

Permanent Magnet Biased Inductors

And Additional investigations on: Biasing topologies for AC applications, Parametric transformers using permanent magnets, and Optimization of conduction losses on planar transformer windings

Revilla Aguilar, Andres

DOI (link to publication from Publisher):
[10.54337/aau550070662](https://doi.org/10.54337/aau550070662)

Publication date:
2023

Document Version
Publisher's PDF, also known as Version of record

[Link to publication from Aalborg University](#)

Citation for published version (APA):
Revilla Aguilar, A. (2023). *Permanent Magnet Biased Inductors: And Additional investigations on: Biasing topologies for AC applications, Parametric transformers using permanent magnets, and Optimization of conduction losses on planar transformer windings*. Aalborg Universitetsforlag.
<https://doi.org/10.54337/aau550070662>

General rights

Copyright and moral rights for the publications made accessible in the public portal are retained by the authors and/or other copyright owners and it is a condition of accessing publications that users recognise and abide by the legal requirements associated with these rights.

- Users may download and print one copy of any publication from the public portal for the purpose of private study or research.
- You may not further distribute the material or use it for any profit-making activity or commercial gain
- You may freely distribute the URL identifying the publication in the public portal -

Take down policy

If you believe that this document breaches copyright please contact us at vbn@aub.aau.dk providing details, and we will remove access to the work immediately and investigate your claim.

PERMANENT MAGNET BIASED INDUCTORS

AND ADDITIONAL INVESTIGATIONS ON: BIASING TOPOLOGIES
FOR AC APPLICATIONS, PARAMETRIC TRANSFORMERS USING
PERMANENT MAGNETS, AND OPTIMIZATION OF CONDUCTION
LOSSES ON PLANAR TRANSFORMER WINDINGS

BY
ANDRÉS REVILLA AGUILAR

DISSERTATION SUBMITTED 2023



AALBORG UNIVERSITY
DENMARK

PERMANENT MAGNET BIASED INDUCTORS

**AND ADDITIONAL INVESTIGATIONS ON:
BIASING TOPOLOGIES FOR AC APPLICATIONS,
PARAMETRIC TRANSFORMERS USING PERMANENT
MAGNETS,
AND
OPTIMIZATION OF CONDUCTION LOSSES ON PLANAR
TRANSFORMER WINDINGS**

by

Andrés Revilla Aguilar



AALBORG UNIVERSITY
DENMARK

PhD Dissertation.

Aalborg 2023

Dissertation submitted: May 2023

PhD supervisor: Professor Stig Munk-Nielsen,
Aalborg University

Assistant PhD supervisors: Associate Prof. Szymon Michal Bęczkowski,
Aalborg University

Post. Doc. Hongbo Zhao,
Aalborg University

PhD committee: Associate Professor Kaiyuan Lu
Aalborg University, Denmark

Professor Teng Long
University of Cambridge, United Kingdom

Professor Emeritus Gerard Hurley
National University of Ireland, Ireland

PhD Series: Faculty of Engineering and Science, Aalborg University

Department: AAU Energy

ISSN (online): 2446-1636

ISBN (online): 978-87-7573-703-1

Published by:
Aalborg University Press
Kroghstræde 3
DK – 9220 Aalborg Ø
Phone: +45 99407140
aauf@forlag.aau.dk
forlag.aau.dk

© Copyright: Andrés Revilla Aguilar

Printed in Denmark by Stibo Complete, 2023

ENGLISH SUMMARY

This thesis presents a compilation of research work, aimed at improving the design trade-offs and performance of magnetic components for power electronics applications. The thesis is divided in two parts.

The first and main part, is focused on the research of *permanent magnet biased inductors*, *PMBIs*, suitable for increasing the energy density of power inductors operating in *DC* applications. A *100%* biased inductor can achieve the same inductance and current requirements with only half of the core's area cross-section, or half of the required number of turns, compared to a standard non-biased inductor. In the main part of the thesis are covered, the basic theory background required for the design of *PMBIs*, the historical evolution of the *PM* and core topologies, and the main achievements and limitations found on the state-of-the-art documented *PMBI* implementations. A new topology of *PMBI* with improved characteristics has been developed and documented in this part of the thesis and in the attached publications *P1*, *P2*, *P3* and *P4*. This new *PMBI* topology employs standard non-gapped *UU* cores and *PMs* and is proven to achieve *100%* linear biasing in both ferrite and silicon-iron laminations cores. It has also been proven the possibility of achieving over-biased states, where the biasing flux has shifted the linear region of the core into high current levels, further increasing the *PMBI*'s energy density. The analysis and calculations required for the design of the *PMBI* topology has been approached using finite element analysis (*FEMM*) and *MEC* simulations. Several prototypes using the new *PMBI* topology has been implemented and empirically tested in common *DC* power inductor applications.

The second part of the thesis presents a summary of other brief investigations, related to magnetics components for power electronics. This second part includes research on: The possibility for a symmetric *PM* biasing topology, suitable for improving energy density of inductors for *AC* applications; A new topology of *parametric transformer*, *PT* with improved characteristics based on *PM* biasing. The new *PM-PT* topology has been physically implemented and documented on a journal publication, *P5*; And a practical investigation presenting a new design technique, suitable for reducing the conduction losses in high frequency planar transformer windings.

PERMANENT MAGNET BIASED INDUCTORS

DANSK RESUMÉ

Denne afhandling præsenterer en samling af forskningsarbejde, rettet mod at forbedre design trade-off og ydeevne af magnetiske komponenter til power-elektronik applikationer. Specialet er opdelt i to dele.

Den første del er hoveddelen fokuseret på forskning i *permanent magnet biased induktorer*, *PMBIs*, som er brugbare til at øge energitætheden af strøminduktorer, i *DC*-applikationer. En *100 %* biased induktor kan opnå de samme induktans- og strømkrav med kun halvdelen af kernens arealtværsnit eller halvdelen af det nødvendige antal drejninger sammenlignet med en standard ikke-biased induktor. I afhandlingens hoveddel er dækket, den grundlæggende teoretiske baggrund, der kræves for design af *PMBIs*, den historiske udvikling af *PM'en* og kernetopologier, og de vigtigste resultater og begrænsninger inden for state-of-the-art dokumenterede *PMBI*-implementeringer. En ny topologi af *PMBI* med forbedrede karakteristika er blevet udviklet og dokumenteret i denne del af afhandlingen og i de vedhæftede publikationer P1, P2, P3 og P4. Denne nye *PMBI*-topologi anvender standard non-gapped *UU*-kerner og *PMs* og har opnået *100 %* lineær bias i både ferrit- og silicium-jern lamineringskerner. Det er også blevet bevist muligheden for at opnå over-biased tilstande, hvor bias flux har rykket det lineære område af kernen til højere strømniveauer, hvilket yderligere øger *PMBI'ens* energitæthed. Analysen og beregningerne, for design af *PMBI*-topologien, er blevet behandlet ved hjælp af finite element-analyse (*FEMM*) og *MEC*-simuleringer. Adskillige prototyper, der bruger den nye *PMBI*-topologi, er blevet implementeret og empirisk testet i almindelige *DC*-effektinduktorapplikationer.

Anden del af afhandlingen præsenterer et resumé af andre kortere undersøgelser, omkring magnetiske komponenter til effektelektronik. Denne anden del omfatter forskning i: Muligheden for en symmetrisk *PM*-biasing topologi, egnet til at forbedre energitætheden af induktorer til *AC*-applikationer; En ny topologi af *parametriske transformere*, *PT* med forbedrede egenskaber baseret på *PM-bias*. Den nye *PM-PT* topologi er blevet fysisk implementeret og dokumenteret på en tidsskriftspublikation, P5; samt en praktisk undersøgelse, der præsenterer en ny designteknik, velegnet til at reducere ledningstabene i højfrekvente plane transformatorviklinger.

PERMANENT MAGNET BIASED INDUCTORS

TABLE OF CONTENTS

1. INTRODUCTION	15
1.1. Initial Problem Definition	15
1.2. Permanent Magnet Biasing	18
1.3. Aim of the Project.....	20
1.4. Outline of the Thesis	20

Part 1. Permanent Magnet Biased Inductors

2. THEORETICAL BACKGROUND	25
2.1. Introduction to Magnetics Theory	25
2.2. Magnetic Quantities and Relations	26
2.3. Inductor Design	36
2.4. Introduction to Permanent Magnets	41
3. STATE OF THE ART	45
3.1. Theoretical benefits of <i>PMBI</i> design strategies.....	45
3.2. Evolution of <i>PMBIs</i> Topologies.....	48
3.2.1. Topologies with PM inside the airgap	50
3.2.2. Topology improvements with PM inside the airgap	51
3.2.3. Topologies with PMs outside the airgap	52
3.3. Physical <i>PMBI</i> Implementations	54
3.3.1. Implementations with PMs inside the airgap	54
3.3.2. Implementations with PMs outside the airgap	57
3.3.3. Implementations from the industry and <i>PMBI</i> market products	60
3.4. Conclusions on the State of the Art	61

4. PRACTICAL INVESTIGATION AND PROTOTYPE IMPLEMENTATIONS .	63
4.1. Practical Investigation	63
4.2. <i>PMBI</i> Prototype Implementations	65
4.2.1. Ferrite flyback transformer	66
4.2.2. Steel laminations DC link choke	68
4.2.3. Ferrite filter inductor pair.....	70
5. DESIGN ANALYSIS AND SIMULATION OF THE SATURATION-GAP TOPOLOGY	73
5.1. Introduction.....	73
5.2. <i>FEA</i> Simulations	73
5.3. Simplified <i>MEC</i> analysis	75
5.4. Design Procedure	79
6. CONCLUSIONS ON PERMANENT MAGNET BIASED INDUCTORS	85

Part 2. Additional investigations on: Biasing topologies for AC applications, Parametric transformers using permanent magnets, and Optimization of conduction losses on planar transformer windings

7. INVESTIGATIONS ON SYMMETRIC BIASING TOPOLOGIES FOR AC APPLICATIONS.....	89
7.1. Introduction to <i>AC-Biasing</i>	89
7.2. Potential <i>AC-biasing</i> Topologies.....	92
7.3. Practical Implementations	93
7.4. <i>FEA</i> Simulations	94
7.5. Conclusions on <i>AC-biasing</i>	95

8. INVESTIGATIONS ON THE USE OF PM-INDUCTORS AS PARAMETRIC TRANSFORMERS.....	97
8.1. Introduction to Parametric Transformers	97
8.2. Non-inductive Coupling on the Saturation-gap Topology.....	99
8.3. New Symmetric <i>Saturation-gap PM-PT</i> Topology.....	100
8.4. Practical Experimentation	101
8.5. Conclusions on the new <i>PM-PT</i> Topology	102
9. INVESTIGATIONS ON COPPER LOSSES ON HIGH FREQUENCY PLANAR WINDINGS.....	103
9.1. Introduction to Planar Magnetics	103
9.2. Eddy Currents in Electric Conductors	104
9.3. AC Losses in Planar Windings	105
9.4. A New Technique for Current Density Equalization.....	107
9.5. Practical Implementation	108
9.6. Conclusions on AC Losses in Planar Windings	109
References	111

APPENDIX. LIST OF PUBLICATIONS

Conference Publications

P1: “Method for Introducing Bias Magnetization in Ungapped Cores: The Saturation-Gap”, Andres Revilla Aguilar, and Stig Munk-Nielsen, Applied Power Electronics Conference and Exposition (APEC) 2014, 29th Annual IEEE, pp 721 - 725. 16-20 March 2014.

P2: “Size Reduction of a DC Link Choke Using Saturation-gap and Biasing with Permanent Magnets”, Andres Revilla Aguilar, Stig Munk-Nielsen, Marco Zuccherato and Hans-Jørgen Thougard, PCIM Europe 2014, pp 1667 – 1674. 20-22 May 2014.

P3: “Design Analysis and Simulation of Magnetic Biased Inductors with Saturation-Gap”, Andres Revilla Aguilar, and Stig Munk-Nielsen, Power Electronics and Applications (EPE'14-ECCE Europe), 2014 16th European Conference on, pp 1 - 11. 2014.

Journal Publications

P4: “Half Size Reduction of DC Output Filter Inductors with the Saturation-gap Magnetic Bias Topology”, Andres Revilla Aguilar, and Stig Munk-Nielsen, Journal of Emerging Selected Topics on Power Electronics JESTPE 2015, Vol. 4, Issue 2, pp 382 – 392. June 2016.

P5: “Parametric Transformer using PM-Inductors with Saturation-gap”, Andres Revilla Aguilar, Bjørn Rannestad and Stig Munk-Nielsen, Journal of The Institution of Engineering and Technology, IET PEL 2020, Vol. 13, Issue 19, 30 December 2020, pp. 4581-4591.

PERMANENT MAGNET BIASED INDUCTORS

1. INTRODUCTION

1.1. INITIAL PROBLEM DEFINITION

The technology of power electronic systems has been in constant development since its early beginnings. In order to assist the constant growth of the electric distribution grid, the automatized production industry and the communication technologies, the demand of power electronic systems is constantly increasing, and requiring higher power density, efficiency, and reliability. Some examples of power electronic systems include: the power supplies in every electronic appliance, *AC to DC*, or *DC to DC* converters, *DC to AC* inverters, motor drive systems, battery chargers, *MPP* trackers for solar *PV* or wind turbines, power factor correction or active filtering and power control systems for the power grids. Power electronic systems are utilised to transform the electrical characteristics of the power available at the energy source, into the required electrical characteristics for the power loads. From a generic perspective, power electronic systems can be described with the block diagram presented in Fig.1.1. The total volume of most common power electronic systems can be characterised by sum of the following components or modules:

- Passive components: Capacitors and Magnetics (Inductors and Transformers).
- Electronic Switch Semiconductors. (Diodes, *IGBTs*, *MOSFETs*...).
- Switching control circuit.
- Dissipation and cooling systems.

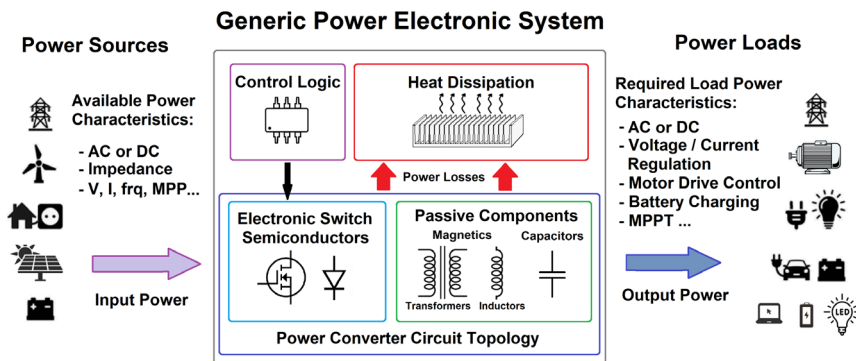


Fig. 1.1. Generic block diagram of power electronic systems and their possible applications.

PERMANENT MAGNET BIASED INDUCTORS

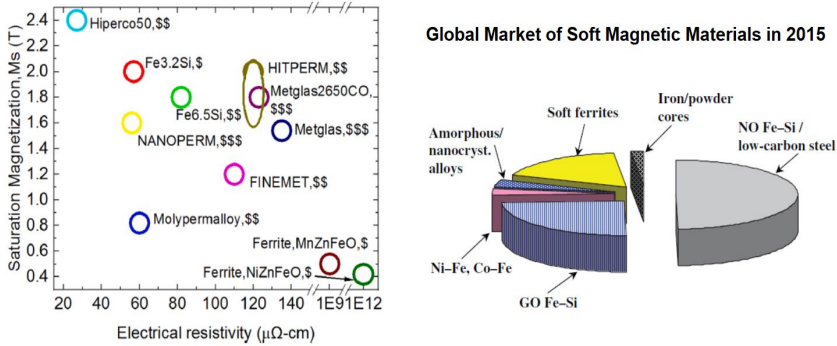


Fig. 1.2. Soft magnetic materials. Left: Saturation flux density or magnetization and electrical resistivity of some common magnetic materials. Right: Global market capital estimation of magnetic materials from 2015. Sources [6][7].

In a simplistic approach, the power density of a power converter can be estimated to be proportional to the individual energy density of the passive components, multiplied by the switching frequency of the control circuit. The developments of the semiconductor industry have been providing a constant increase in the switching frequency capabilities of power semiconductors, approximately doubling its maximum frequency every ten years. Constant developments on power converter topologies and control schemes have provided great improvements on the energy efficiency and reliability of power systems, improving the power density by minimizing switching losses and relieving requirements of the passive components and the cooling systems. On the other hand, the historical evolution of the energy density achievements of passive and specially magnetics components, has been comparatively more limited. Magnetic components, as well as cooling systems and the interconnection between modules has been identify as the main barriers for the constant power density evolution of future power electronic systems. [1]-[5][9].

The common inductor and transformer constructions consist of one, or more, electric conductive wires coiled around a core of a magnetic conductive material. These ferromagnetic materials, used for the cores, are heavy and make magnetic components responsible of a dominant part of the total weight of most electronic appliances. The size of the inductor is proportional to its energy density and can be estimated by its required inductance and current rating. In **Fig.1.2.left** are presented properties of some of the more used materials for magnetic cores. In the vertical axes, it is presented the higher limit on the maximum magnetization or saturation flux density, which is proportional to the achievable energy density with each core material. On the horizontal axes is presented the electric resistivity of the different core materials. Eddy current losses in the magnetic cores are proportional to the frequency squared, and therefore, the electric resistivity can be an indicative factor to determine the maximum

INTRODUCTION

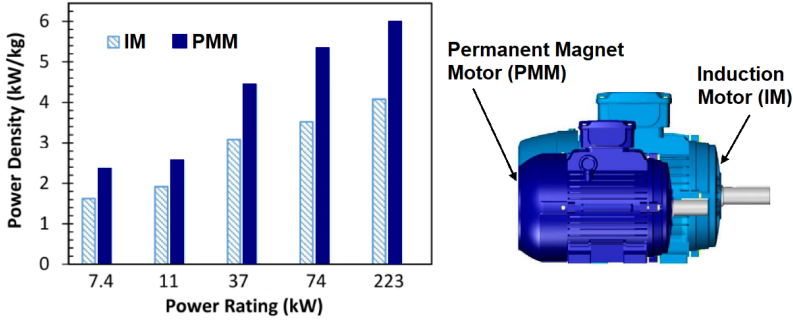


Fig. 1.3. Power density comparison of permanent magnet motor (PMM) vs induction motor (IM), at different power rating [8].

frequency of operation of a core material. In **Fig.1.2.right** it is depicted the approximated global market distribution of magnetic materials, in 2015 [6]. The more commonly used materials are silicon-iron ($SiFe$) and ferrites ($MnZnFeO$ and $NiZnFeO$). The latest developments in material technology have provided: amorphous, nanocrystalline and cobalt-based alloys, with improved energy density compared to ferrites and allowing higher frequency of usability compared to silicon-iron cores. On the other hand, these newer core materials present a higher production cost and big impact on the total price and therefore they only achieved a minimal part of the global market. More than half of the total market is dominated by silicon-iron laminations ($SiFe$), both grain-oriented (GO) and non-grain-oriented (NO), due to the high demand of low frequency applications such as power motors and transformers for the power grid. Despite their relatively high energy density, silicon-iron laminated cores can only be used for low frequency applications (< 500 Hz) due to their low electric resistivity. For high frequency applications, most of the remaining market is dominated by ferrites. Ferrite cores are the preferred choice for higher frequency applications, allowing for higher power density despite having a lower energy density compared with silicon-iron cores. The main trend towards increasing the power density of power converters, has been toward increasing the switching frequency, relieving volume requirements from the magnetic components. One of the latest strategies for high frequency magnetic components is the use of planar magnetics, presenting high resistivity ferrite cores with a reduced profile and allowing for printed *PCB* windings or foil windings. On the other hand, the increase in power density due to an increase in switching frequency, come at expenses of additional power losses due to skin-and-proximity-effects on the windings, associated with high frequency operation. [6]-[10][47]-[51].

In order to assist the constant increase in power density of power electronic systems, it is desired the development of more efficient and compact inductors. One possible

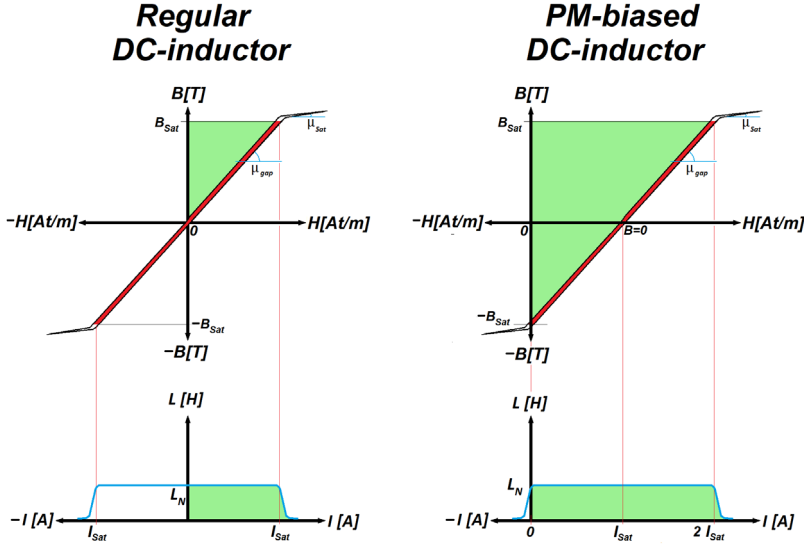


Fig.1.4. *BH*-loops (top) and *Inductance vs current, $LvsI$* profiles (bottom), of a regular (left) and PM-biased DC-inductors, *PMBI* (right). Green areas on the *BH*-loops are representative of stored energy. Red areas represent energy loss per cycle. Green areas on the *LvsI* profiles represent the utilized *LI* product.

technique for enhancing the energy density of power inductors in *DC* applications, is the use of permanent magnet biased inductors, *PMBIs*. [11]-[38].

1.2. PERMANENT MAGNET BIASING

Permanent magnets, *PMs* has been utilised to increase the power density and efficiency of electric motors. A permanent magnet motor, *PMM* presents approximately 40% higher power density compared to an induction motor, *IM*. **Fig.1.3.** shows a comparison of the achieved power density of *PMMs* and *IMs*, at different power ranges. *PMs* provide a free magnetization of the *PMM* rotor, while the *IM* rotor needs to be magnetised from the stator currents. Therefore, the comparatively lower efficiency and power density of *IMs* is especially noticeable at higher power ratings [8].

In a similar manner, *PMs* can also be utilised to increase the energy density of inductors operating in *DC* applications. *PMBIs* present higher energy density compared to standard non-biased inductors. Inductors intended for *DC* applications present a highly asymmetric magnetizing current. Their core's operation region on the *BH* curve is restricted to the first quadrant. *PMBIs* use permanent magnets in order to

INTRODUCTION

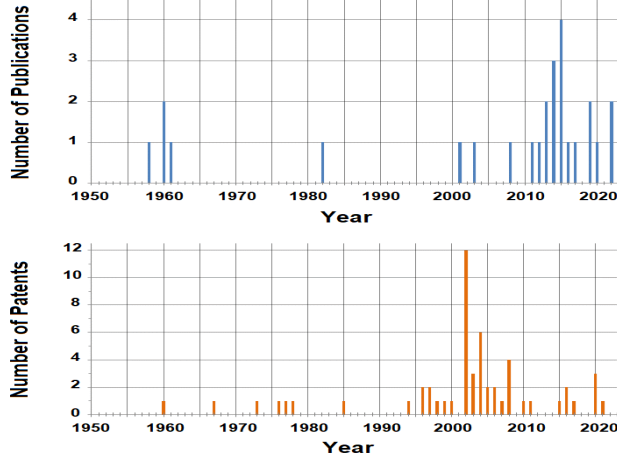


Fig.1.5. Timeline of scientific publications (in blue) and patents (in orange) on *PM-biased* Inductors. Publications are list chronologically on the references section. Patent numbers are list in [17].

introduce an opposing bias magnetic flux in the core material and accordingly extend its maximum *DC* current limit. In **Fig.1.4.** is shown the *BH* loop of a *PMBI* and a non-biased inductor of the same size. In the *BH* loop of a non-biased *DC* inductor (**Fig.1.4.left**) the maximum allowable magnetic field strength, H_{sat} and accordingly the inductor's saturation current, I_{sat} , is defined by the value at which the flux density, B has reached the saturation limit of the core material, B_{sat} . In the *BH* loop of an ideal *PMBI* (**Fig.1.4.right**), there is an opposing bias magnetic flux density, $-B_{bias}$ inside the core, at the initial state of zero current (or zero *H*-field). The maximum allowable bias flux, ϕ_{bias} is limited by the saturation flux density, B_{sat} of the core and its area cross-section, A_c . Full bias is achieved when the initial equilibrium point (at zero current) of the core's *BH* has been shifted to $-B_{sat}$. An ideal *PMBI* (**Fig.1.4.right**), presents a maximum magnetic field strength, H_{sat} and saturation current I_{sat} , two times higher of what is achieved with a non-biased core ($2 I_{sat}$). It can be appreciated that when full biasing is achieved, the energy capacity (green areas in the *BH* loop) increases by 400%. This calculation relies on the assumption of achieving full magnetic biasing within the complete length of the core and is not accounting for possible additional losses introduced by the possible biasing techniques. When facing practical applications, achieving full biasing of the core without introducing detrimental effects on the inductor's efficiency or the *PM*'s lifetime, is a much more challenging situation. **Fig.1.5.** present the timeline of scientific papers and patent documents published during the last decades. The theoretical benefits of *PM-biasing* were recognised more than six decades ago, on the other hand the practical implementation and optimization of physical prototypes has been an open area for research until present days, with a relatively small attention from the scientific

community. The first documented *PMBI* topology, consisted of placing the *PM* inside the inductor's airgap. This is probably the more intuitive strategy to introduce the desired bias magnetic flux into the core. On the other hand, this first topology presented important limitations and expose the *PM* to strong demagnetizing fields, limiting its usability. The more recent topologies, described in the patent documents and proposed by the latest scientific publications, tend to rely on the use of specially design core shapes. The patented topologies rely on no-standardised core shapes, which require a customised production, increasing the cost and limiting the replicability of these *PM* biasing topologies. Since the last two decades, the academic and industry interest in *PMBIs*, appears to be reawaken, with an increasing number of publications and patents. These latest developments on *PMBIs* has been supported in great manner by the developments of the *PM* industry, which has provided stronger and higher performance rare-earth *PMs* materials, like *NdFeB* and *SmCo*, allowing improvement of the design trade-offs and possibilities on *PMBIs*. [11] - [38].

1.3. AIM OF THE PROJECT

The main part of this thesis, focus of the improvement of the practical performance and design achievements of *PMBIs*. This study aims for the development of more compact and better performance power *DC* inductors, and to enrich the currently growing academic interest on *PMBIs*. This thesis evaluates the different topologies found on the scientific literature and their efficiency and limitations.

An investigation oriented to improve the limitations associated with known topologies, achieved the development of a new biasing methodology using cores with no airgaps. The new developed topology is analysed and empirically tested in common power inductor *DC* applications and achieves higher biasing level and improved characteristics compared with state-of-the-art *PMBI* implementations.

The second part of the project focuses on different practical investigations on the field of magnetics in power electronics applications, aiming to identify improvement techniques and promising areas of investigation. This series of investigations include: an analysis of possible *PM-inductor* topologies presenting bidirectional biasing flux, suitable for *AC* applications, a new topology of *parametric transformer* using *PMs* and a practical investigation for the optimization of conduction losses in high frequency planar transformer windings.

1.4. OUTLINE OF THE THESIS

The thesis is separated in two parts. The first and more extensive part, is focus on the analysis and development of *PMBIs*. On the second part of the thesis is presented other additional research on the possibilities of *PMs* and power magnetics components.

INTRODUCTION

Part 1. Permanent Magnet Biased Inductors

Chapter 2 provides a theoretical background and the main terminology required for analysis and design of *PMBI*. The theoretical introduction includes basic magnetic theory, inductor design and introduction to permanent magnets, *PMs*.

The scientific literature review and the state of the art is presented in **Chapter 3**, covering the more common analysis and design approaches and the different employed *PMBI* topologies and their evolution over the years.

Chapter 4 presents a practical investigation towards the development of a new biasing topology with improvements over the state-of-the-art achievements. Three different practical experiments and physical *PMBI* prototypes of the proposed new topology were investigated and empirically tested. The *PMBI* prototypes are compared against standard inductors operating in different *DC* applications, like: *DC-link filters* and *fly-back transformers*.

In **Chapter 5**, the new biasing topology referred as the “*Saturation-gap*”, is analysed, and simulated. The theoretical analysis and the design procedure of *PMBIs* with the “*Saturation-gap*” topology are address using *MEC* and *FEA* simulations.

Chapter 6 presents the conclusions of the present study on *PMBIs* for *DC* applications. The *Saturation-gap* topology is evaluated according to the goals of the study.

Part 2. Additional investigations on: Biasing topologies for AC applications, Parametric transformers using permanent magnets, and Optimization of conduction losses on planar transformer windings

Chapter 7 presents the research towards the possibility of a new symmetric biasing concept, suitable for minimizing the size of *AC* inductors. The proposed symmetric biasing topology is analysed with the use of *FEA* simulations. Physical prototypes were built, and their electrical characteristics were empirically measure. None of the tested prototypes provided significant improvements and the research area is suspended.

Chapter 8 analyses further possibilities of the use of *PMs* on inductors. The *Saturation-gap* topology is being analysed on its potential operation as a controllable variable inductance. A new symmetric *PM-inductor* design, based on the *saturation-gap* topology, has been develop. The new symmetric topology has been simulated and empirically tested, demonstrating its performance as a *Parametric-Transformer*, *PT*. The new *PM-PT* topology has been documented in a journal publication, *P5*, and presents improved characteristics compared with previous *PT* topologies. This chapter

PERMANENT MAGNET BIASED INDUCTORS

also provides a summary of some possibilities of the new *PM-PT* topology for power electronics applications.

Finally, **Chapter 9** present a brief analysis about high frequency planar magnetics. The main challenges and improvement strategies found on the literature, are being summarised. A new technique for optimizing current density distribution and minimize conduction losses, has been develop and presented. A small experimental analysis is performed and provides a successful proof of concept. The proposed technique is identified as a new design improvement and a potential area for future research.

Part 1

Permanent Magnet Biased Inductors

PERMANENT MAGNET BIASED INDUCTORS

2. THEORETICAL BACKGROUND

2.1. INTRODUCTION TO MAGNETICS THEORY

Fig.2.1.a) depicts the electric and magnetic fields, in a cross-section plane of a loop of wire carrying and electric current. Dashed radial lines with blue vectors represent the electric field forces, \vec{E} . Static electric charges are always associated with static electric field vector forces. On the other hand, magnetic field forces are only produced when electric charges are not static but flowing on a conductor, producing an electric current. The loop lines with red vectors represent the magnetic field lines of force, $\vec{\phi}$. The concentration of these *lines of force*, is defined as the *magnetic flux density*, \vec{B} . There are no magnetic monopole charges, and therefore magnetic forces always form closed loops. The *magnetic flux lines*, originates at the surface of the current carrying conductor. As current increases, magnetic lines expand becoming concentrated inside the conductor's loop, and stretching outwards outside the conductor. The electric and magnetic fields are representative of stored of energy. The tendency to maintain a constant voltage by storing energy in the *electric field*, \vec{E} is refer as *capacitance*, C . The tendency to maintain a constant current by storing energy in the *magnetic field*, \vec{B} , is refer as *inductance*, L . Inductors and transformers' geometry and materials are optimised for the storage of energy into magnetic fields. A simplified *EE* core inductor

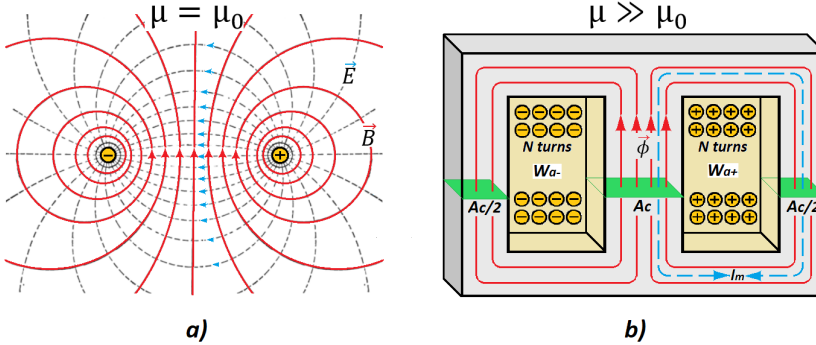


Fig.2.1. a) Electric and magnetic fields, in a cross-section plane, of a single turn of wire carrying a current in free space. *Electric field intensity*, \vec{E} represented in dashed lines with blue vectors. *Magnetic flux density*, \vec{B} in solid lines with red vectors. **b)** Simplified *EE* core inductor. Core's *area cross-section*, A_c in marked in green. The average magnetic length, l_m marked in dashed blue line. Total *Magnetic Flux*, $\vec{\phi}$ through A_c in solid lines with red vectors. W_a (yellow) is the total window area available for windings. Conductors (yellow) with "+" sign indicate current flowing *into the page*, and "-" sign current *out of the page*.

PERMANENT MAGNET BIASED INDUCTORS

is depict in **Fig.2.1.b**). Inductors typically present a big number of turns coiled around a core material with a high *magnetic permeability*, μ . The current generating the magnetic field is therefore multiply by the number of turns, and the medium in between the windings is a better conductor of the magnetic field as compared to **Fig.2.1.a**).

2.2. MAGNETIC QUANTITIES AND RELATIONS

The main magnetic quantities in the S.I. units, are summarised in relation to the basic inductor's (or transformer) core dimensions and magnetic properties [10].

Core Dimensions: The magnetic conduction dimensions are characterised by the core's *magnetic length*, l_m , and the core's *area cross-section*, A_c . The blue dashed line in **Fig.2.1.b**) (and **Fig.2.2.a**)) represent the average magnetic path length of the core, commonly refer as *magnetic length*, l_m . The green area of the *centre-leg* of the *EE* core is the *effective area cross-section*, A_c . Each of the side-legs of the *EE* core, presents half of the total *area cross-section*, $A_c/2$. The total area available for electric conductor's windings is refer as the *window area*, W_a depicted in yellow in **Fig.2.1.b**). The plus sign, “+” indicates current flow *into-the-page*. The minus sign, “-” indicates current flow *out-of-the-page*. The effective *window area*, W_a , is equivalent to the area of only one window of the *EE* core: $W_a = W_{a+} = W_{a-}$, since the same windings are coiled through both windows.

Magnetomotive Force: $F[At]$ has units of *Ampere-turns*. Electric current is considered as the source of magnetic fields. Therefore, is also common to find references to *magnetomotive force* in units of *Amps*, $F[A]$. This quantity is also sometimes using the symbol *mmf*[At]. The total *magnetomotive force* in an inductor, is calculated as the *current*, $I[A]$ multiply by the number of turns, N :

$$F = I N \quad (2.1)$$

Magnetic Field Strength: $H [A/m]$ is express in units of *Amps per meter*. It is sometimes referred as *Magnetic Field Intensity* or *Magnetizing Force*. By taking the line integral of H along the closed loop *magnetic length*, l_m , we can express *Ampere's Law* relating the total magnetic field strength, H to the current and number of turns:

$$I N = F = \oint_{l_m} \vec{H} dl \quad (2.2)$$

Assuming uniform field we can express *magnetic field strength* as:

$$H = \frac{F}{l_m} = \frac{I N}{l_m} \quad (2.3)$$

THEORETICAL BACKGROUND

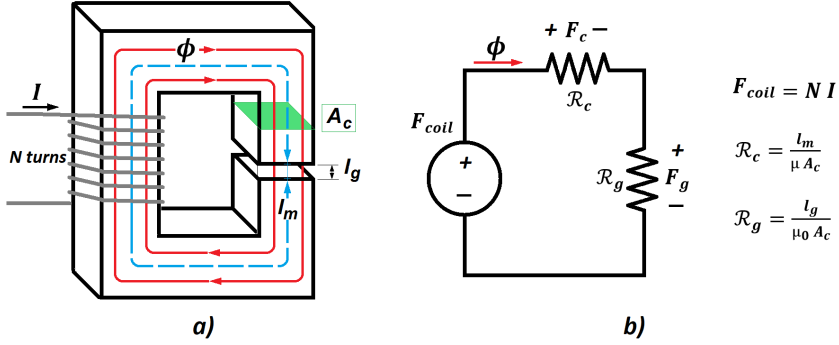


Fig.2.2. Schematic of a Gapped Inductor **a)** Inductor with a ferromagnetic core with an airgap with length, l_g . Core's area cross-section, A_c in marked in green. The average magnetic length, l_m is marked in dashed blue line. **b)** Magnetic equivalent Electric Circuit, MEC of the inductor.

Magnetic Flux: ϕ [Wb]. Represents the total amount of *magnetic lines of force* and is express in units of *Webers*. The *magnetic flux*, ϕ flowing in an inductor's core, can be calculate by the time integral of the voltage on one turn of its windings, using the expression of *Faraday's Law* in its integral form:

$$\phi = \frac{1}{N} \int V(t) dt \quad (2.4)$$

In the case of a constant DC voltage, V_{DC} applied for a time period, T the *magnetic flux* can be calculated as:

$$\phi = \frac{V_{DC} T}{N} \quad (2.5)$$

Magnetic Flux Density: B [T] has units of *Tesla*. It is sometimes referring as magnetic field density, *magnetization*, *magnetic Induction*, or the *B-field*. It represents the density of *magnetic flux lines* per surface area. Therefore, is sometimes express in units of *Webers per square meter*, $[Wb/m^2]$ which is equivalent to *Teslas* [T]. *Magnetic flux density* can be calculated as the derivative of the *magnetic flux* per differential of surface area:

$$B = \frac{d\phi}{dA} \quad (2.6)$$

Assuming homogenous distribution of *magnetic flux* through the core's *area cross-section*, A_c , the *flux density*, B can be calculated by:

PERMANENT MAGNET BIASED INDUCTORS

$$B = \frac{\phi}{A_c} \quad (2.7)$$

Faraday's Law (2.4) can also be express in derivative form, relating the voltage at the inductor's windings with the *flux density*, B in the core area, A_c :

$$V = N \frac{d\phi(t)}{dt} = N A_c \frac{dB(t)}{dt} \quad (2.8)$$

Magnetic Reluctance: \mathcal{R} [At/Wb] is express in units of *Ampere-turns per Weber*, or equivalent units of *per Henry*, \mathcal{R} [H^{-1}]. *Reluctance* can be understood as a magnetic dual equivalent to *electric resistance*, R . Similarly, to *Ohm's Law*, *magnetic reluctance* can be defined as the ratio between the *magneto-motive force*, F to the total *magnetic flux*, ϕ .

$$\mathcal{R} = \frac{F}{\phi} \quad (2.9)$$

The *reluctance* of a magnetic core is proportional to its *magnetic length*, l_m and it is inversely proportional to the core's *area cross-section*, A_c and to the *permeability*, μ of the material. Similar to the expression of electric resistance by the *resistivity* of the conductor material, *reluctance* can be calculated as:

$$\mathcal{R} = \frac{l_m}{\mu A_c} \quad (2.10)$$

It is common to represent *magnetic circuits* by using an *equivalent electric circuit* representation, *MEC*, Where:

- *Magnetomotive forces*, F are represent as electric *voltages*, V .
- *Magnetic flux*, ϕ is represent as electric *currents*, I .
- *Magnetic reluctances*, \mathcal{R} are represent as electric *resistors*, R .

Fig.2.2. shows the magnetic circuit of a generic inductor with an *airgap* and its equivalent *MEC* model.

Magnetic Permeability: μ [H/m] is express in units of *Henry per meter*. Like the *resistivity* of an electric conductor, the *permeability* is independent from the core's dimensions, and it represents the magnetic properties specific to the material used as magnetic conductor. It is defined as the ratio of the *flux density*, B over the *magnetic field strength*, H .

$$\mu = \frac{B}{H} = \mu_0 \mu_r \quad (2.11)$$

The *magnetic permeability of vacuum*, μ_0 is a universal constant with a value of:

THEORETICAL BACKGROUND

$$\mu_0 = 4 \pi 10^{-7} \text{ H/m} \quad (2.12)$$

The *relative permeability*, μ_r of a material is a unit-less factor expressing the magnetic conductor performance of the material as compared to vacuum:

$$\mu_r = \frac{\mu}{\mu_0} \quad (2.13)$$

Every substance can be classified according to its magnetic permeability, by measuring the attained *flux density*, B as response to the presence of a *magnetizing force*, H . There are three types of magnetic responses that a substance can present:

- *Diamagnetic*: Materials with $\mu < \mu_0$
- *Paramagnetic*: Materials with $\mu > \mu_0$
- *Ferromagnetic*: Materials with $\mu \gg \mu_0$

This classification is done according to the *permeability* value of the characterised material as compared to the reference *permeability of vacuum*, μ_0 . Substances presenting a slightly higher *flux density*, B response than vacuum are classify as *paramagnetic*. When the *flux density*, B is even lower than in vacuum, the material classifies as *diamagnetic*. Only the *ferromagnetic* materials respond to magnetic fields in a practically meaningful level. Their higher magnetic permeability makes them suitable for the construction of inductor cores and other magnetic systems. The only elements that classify as *ferromagnetic* materials are *Iron (Fe)*, *Cobalt (Co)* and *Nickel (Ni)*. Every other know element is either *diamagnetic* or *paramagnetic*, and present a much weaker response to a *magnetizing force*, H . Different iron-based compounds are typically employed as inductor core material, presenting a *relative permeability*, μ_r in the range from 500 to 10000. The *relative permeability*, μ_r of *diamagnetic* and *paramagnetic* materials is insignificant compared to *ferromagnetic* materials and is typically approximate to unity; $\mu_r = 1$ for any practical calculations.

The BH-loop: $B(H)$. The *permeability* of ferromagnetic core materials is a non-linear and non-univalent function commonly refer as the *BH-loop*. The *BH-loop* represents the level of *magnetic flux density*, B achieved on a specific material as a function of the applied *magnetic field strength*, H and the slope of the *BH-loop* is representative of the *magnetic permeability*, μ of the material. The common shape of a generic *BH-loop* is represent in **Fig.2.3.(left)** The *BH* curve of a ferromagnetic material present a characteristic *non-linear* function. This effect is known as *magnetic saturation*: Ferromagnetic materials present a high *permeability* when the magnitude of the *flux density*, B is below the *saturation limit* B_{sat} of the material. When the flux density has reach B_{sat} , the material is said to be *saturated*, and further increments in the *magnetizing force*, H does only result in minimal increments in the achieved flux density, B characterise by a drop in *permeability*. The *relative permeability* of ferromagnetic materials operating below their saturation limit is in the range, $\mu_r =$

PERMANENT MAGNET BIASED INDUCTORS

$[10^3 \text{ to } 10^6]$, while in the saturation region the *relative permeability* is slightly above unity $\mu_r \cong 1$.

The BH curve is also, a *non-univalent* function and therefore follows a closed loop, due to the effect known as *hysteresis*. The areas enclosed between the BH curve and the B -axes, coloured in green in **Fig.2.3.**, are representative of energy stored in the magnetic field, operating in AC within the linear region of the core. When energy is introduced into the magnetic field, the inductor operation is rising through the right side of the BH loop. When the stored magnetic energy is release back into electric form, a part of it is dissipate into losses and the operation point falls through the left side of the BH loop. Accordingly, the red area enclosed by the BH loop in **Fig.2.3.**, is representative of the energy loss per cycle. The shape and size of the BH loop described by the operation point of an inductor, is dependent on the rate at which *magnetic flux*, ϕ is being stored and released. The higher the *voltage*, V or the *frequency* of operation, f ; the higher the *magnetic flux rate*, $d\phi/dt$ within the core. If the rate at which *magnetic flux*, ϕ is entering and leaving the core is increase, more energy is being lost into thermal dissipation and the area enclosed by the BH loop becomes wider. The ability of a magnetic material to maintain its energy storage efficiency at higher *magnetic flux rates*, $d\phi/dt$ is in part proportional to its electric resistivity, due to the effect know as *eddy currents*. The operation frequency of the inductor will typically be the determinant factor for deciding the choice of the core material. In order to avoid excessive thermal losses due to *eddy currents*, it is required that the, magnetically conductive, core material presents a relatively high resistance to the flow of electric current. Insulated laminations of iron are commonly use in low frequency applications. The thinner the lamination width, the higher the frequency of usability. The thinnest iron laminations cores operate at frequencies typically below $1kHz$. For operation at higher frequencies, a core material with higher electric resistance is required. Ferrites are non-conductive compounds containing *iron oxides* combined with *zinc* and *nickel* or *manganese*. An important number of ferrite compounds and grades exist presenting a range of electric resistivity and magnetic properties, suitable for the multiple requirements of possible applications. The more common *manganese-zinc*, $MnZn$ ferrite core, power inductors are typically used for operating frequencies up to $500KHz$. The latest achievements in ferrite cores uses *nickel-zinc*, $NiZn$ based compounds extending the frequency of usability into the MHz range.

Airgap Length: $l_g[m]$, is measured in units of *meters*. The high magnetic *permeability* of the core materials makes them suitable for guiding and concentrating the *magnetic flux*, ϕ generated by the coil. On the other hand, the maximum storable energy is very limited. In order to increase the storable energy, the total *reluctance* of the magnetic circuit of the inductor is typically increase by the use of an *airgap*, cut within the magnetic length of the core, l_m , as depicted in **Fig.2.2.a)**. In **Fig.2.3.** it is shown a comparison of the BH -loop of an inductor with and without an *airgap*. It can

THEORETICAL BACKGROUND

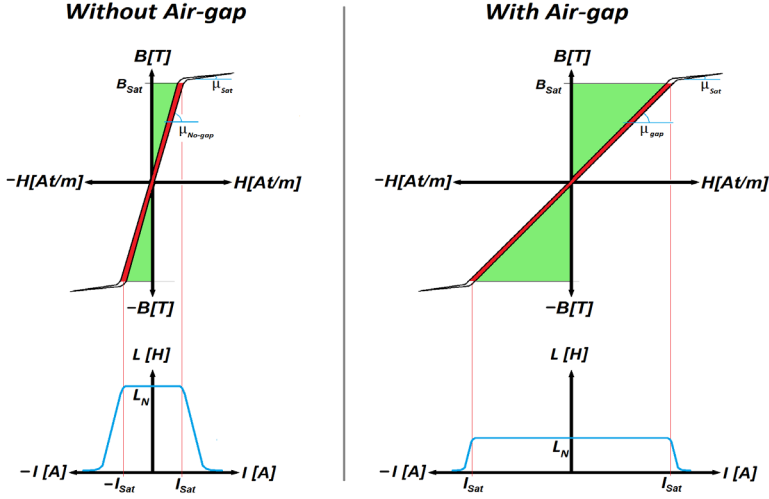


Fig.2.3. Simplified BH loop of a ferromagnetic material (*left*), and simplified BH loop of a gapped inductor (*right*). Green areas are representative of stored energy on AC operation. Red areas are representative of energy loss per cycle.

be appreciated the increase in energy storage (green areas) introduced by using an *airgap*. The magnetic permeability of air is commonly approximated to be equal to the *vacuum permeability*, μ_0 , and the reluctance of the *airgap* can be calculated by:

$$\mathcal{R}_g = \frac{l_g}{\mu_0 A_c} \quad (2.14)$$

In the inductor represented in **Fig.2.2**. The total reluctance of the magnetic circuit is defined along the magnetic length, by the series of the *core reluctance*, \mathcal{R}_c and the *airgap reluctance*, \mathcal{R}_g . Since the *permeability*, μ of the core material is orders of magnitude bigger than the *vacuum permeability*, μ_0 (or the material in the *airgap*), the total *reluctance*, \mathcal{R} is dominated and commonly approximated to the *reluctance* of the *airgap*, \mathcal{R}_g .

Inductance: L [H], is measured in units of *Henry*, and can be understood as the ability of the coil to store energy into the magnetic field by slowing the flow of current. It can be represented as the ratio of the total *magnetic flux*, ϕ to the *current*, I generating the magnetic field, multiply by the number of turns:

$$L = N \frac{\phi}{I} \quad (2.15)$$

PERMANENT MAGNET BIASED INDUCTORS

It can also be represented by the relation between the total *energy*, W in *Joules*, stored in the magnetic field, and the *current*, I generating the field:

$$L = \frac{2W}{I^2} \quad (2.16)$$

Inductance, L is proportional to the square of the number of turns, N and inversely proportional to the reluctance, \mathcal{R} of the core's magnetic circuit. It can be calculated as function of the core parameters by:

$$L = \frac{N^2}{\mathcal{R}} = \frac{N^2 \mu A_C}{l_m} \quad (2.17)$$

Assuming the total reluctance of the inductor's magnetic circuit is dominated by the *airgap*, the *inductance* can be approximated by:

$$L \cong \frac{N^2}{\mathcal{R}_g} = \frac{N^2 \mu_0 A_C}{l_g} \quad (2.18)$$

Using the expression for *Inductance*, L in (2.15) and *Faraday's Law* in (2.8), the electrical terminal characteristics of an inductor can be represented by:

$$V_L = N \frac{d\phi(t)}{dt} = L \frac{dI_L(t)}{dt} \quad (2.19)$$

Fig.2.4. shows the relation between the *BH-loop* and the *inductance* as function of *current*, $L(I)$ or $LvsI$, of an inductor with and without *airgap*. The inductor can provide a nominal inductance value, L_N for currents below the saturation limit of the core. The *saturation current*, I_{sat} is defined as the current limit associated with the *magnetizing force*, H_{sat} required to reach the *saturation flux density* B_{sat} on the *BH-loop* of the inductor. At currents higher than I_{sat} , the value of the *inductance*, $L(I > I_{sat})$ drops to a minimum. The increased *reluctance* of the *airgap* reduces the *nominal inductance*, L_N while extends the saturation current limit, I_{sat} .

Flux Linkage: $\lambda[\text{Wb t}]$, is expressed in units of *Weber-turns*, and is representative of the product of the total *magnetic flux*, ϕ multiplied by the *number of turns*, N linking the *magnetic flux*. Assuming all the *flux*, ϕ is contained in the core and linking every wire turn, the flux linkage, λ can be calculated by:

$$\lambda = \phi N \quad (2.20)$$

Using equation (2.20) with (2.15), it is possible to express *flux linkage*, λ as the product of *current*, I and *inductance*, L :

THEORETICAL BACKGROUND

$$\lambda = I L \quad (2.21)$$

Window Utilization Factor: k_u is a scalar (*unit-less*) factor, sometime refer as, *Fill Factor*. It indicates the proportion of the total window area, W_a to the area used by the N turns of the electric conductor with area cross-section, A_W :

$$k_u = \frac{N A_W}{W_a} \quad (2.22)$$

Current Density: $J [A/m^2]$ is quantify in units of *Amps per square meter*. It is representative of the distribution of the charge flow (current) on the *cross-section area of the wire*, A_W :

$$J = \frac{dI}{dS_{A_W}} \quad (2.23)$$

DC currents through copper wire conductors, present a uniform current density distribution through their area cross-section, A_W , and equation (2.23) can be simplified by:

$$J = \frac{I}{A_W} \quad (2.24)$$

In the case of AC currents, the current density distribution is stronger at the surface, than at the centre of the conductor cross-section, A_W , known as the *skin-effect*. The *skin-depth*, $Sd [mm]$ is commonly express in millimetres and represents the maximum depth of current penetration into the conductor cross-section, A_W . It is inversely proportional to the frequency of the current and can be estimate by:

$$Sd [mm] = \frac{66.2}{\sqrt{f}} \quad (2.25)$$

A deeper analysis of the *skin-effect* and other related issues are summarised in Chapter.9, dedicated to high frequency ($> 100kHz$) planar transformers.

Magnetic vector potential: $A [Tm]$ is sometimes refer as *magnetic potential*, or the *A-field*. It is express in units of *Tesla-meter* or equivalent *Weber-per-meter*. *Magnetic potential* is defined as an analogous magnetic quantity to the *electric potential*, \vec{V} . The *magnetic flux density*, \vec{B} is define as the *curl* of the *magnetic potential*, \vec{A} :

$$\vec{B} = \nabla \times \vec{A} \quad (2.26)$$

PERMANENT MAGNET BIASED INDUCTORS

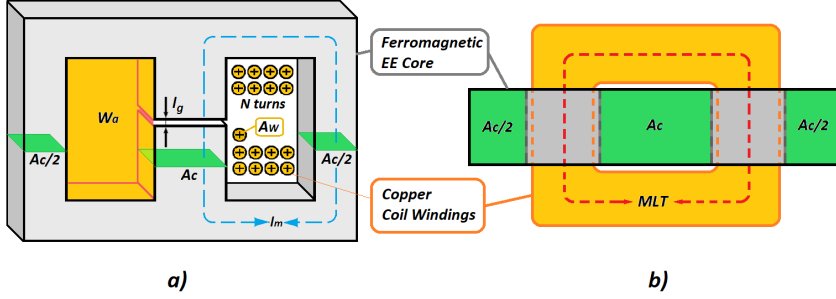


Fig.2.4. Simplified *EE* core inductor. *Airgap* with length, l_g . Core's area cross-section, A_c in marked in green. The average *magnetic length*, l_m is marked in dashed blue line. *Window area*, W_a marked in yellow. *Wire area cross-section*, A_w in dark yellow. *Mean length per turn*, *MLT* marked in dashed red line. **a)** Front view. **b)** Top view.

The *magnetic vector potential*, \vec{A} is not recognised as representative of any physical phenomena, but rather a mathematical construct for commodity of calculations. It is especially useful for calculations in 2D *finite element analysis*, *FEA* simulations.

On a 2D simulation environment, the *magnetic flux*, $\vec{\phi}$ field is defined on the *X-Y* plane, and its associated *magnetic potential*, \vec{A} is in the *Z* axis, through the 2D plane. In a *FEA* simulation of the example inductor depicted in **Fig.2.1.b**), the total *magnetic flux*, $\vec{\phi}$ generated by the current in the *N*-turns windings, can be calculate by integrating the *magnetic potential*, \vec{A} over the surface of each window area [52]:

$$\phi = \left(\frac{1}{W_{a+}} \iint_{W_{a+}} \vec{A} dS \right) - \left(\frac{1}{W_{a-}} \iint_{W_{a-}} \vec{A} dS \right) \quad (2.27)$$

Table 2.1. summarises the common quantities, units, and relationships useful for inductor design [10]. The simplified inductor depicted in **Fig.2.4.** can be used to visualize the different design parameters.

THEORETICAL BACKGROUND

Name	Sym	Units	Formula
Magnetomotive force	F	[At] Ampere-turns	$F = IN = \phi \mathcal{R}$
Magnetic flux	ϕ	[Wb] Weber	$\phi = \frac{1}{N} \int V(t) dt = \frac{F}{\mathcal{R}} = BA_c$
Reluctance	\mathcal{R}	[H ⁻¹] = [At/Wb] Per Henry = Ampere-turns per Weber.	$\mathcal{R} = \frac{F}{\phi} = \frac{N^2}{L} = \frac{l_m}{\mu A_c}$
Magnetic field strength	H	[At/m] Ampere-turns per meter	$H = \frac{F}{l_m} = \frac{B}{\mu}$
Magnetic flux density	B	[T] = [Wb/m ²] Tesla = Weber per square meter	$B = \frac{\phi}{A_c} = \mu H$
Permeability	μ	[H/m] Henry per meter.	$\mu = \mu_r \mu_0 = \frac{B}{H}$
Relative Permeability	μ_r	Scalar	$\mu_r = \mu / \mu_0$
Vacuum Permeability	μ_0	[H/m] Henry per meter.	$\mu_0 = 4\pi 10^{-7} \text{ H/m}$
Inductance	L	[H] = [Wbt/A] Henry = Weber-turns per Ampere.	$L = \frac{\phi N}{I} = \frac{N^2}{\mathcal{R}}$
Flux linkage	λ	[Wbt] Weber-turns	$\lambda = \phi N = IL$
Current	I	[A] Ampere	$I = \frac{F}{N} = \frac{\phi N}{L}$
Current density	J	[A/m ²] Ampere per square meter	$J = \frac{I}{A_w} = \frac{F}{W_a k_u}$
Window area	W_a	[m ²] square meter	$W_a = NA_w / k_u$
Window utilization factor	K_u	Scalar	$k_u = \frac{NA_w}{W_a}$
Wire area cross-section	A_w	[m ²] square meter	$A_w = \frac{I}{J} = \frac{W_a k_u}{N}$
Magnetic vector potential (Magnetic potential) (A-field)	A	[Tm] Tesla-meters or Weber per meter	$B = \nabla \times A$ $\frac{\lambda}{N} = \left(\frac{1}{W_{a+}} \iint_{W_{a+}} \vec{A} dS \right) - \left(\frac{1}{W_{a-}} \iint_{W_{a-}} \vec{A} dS \right)$

Table 2.1. Summary of magnetic parameters, units, and relationships, useful for inductor design.

2.3. INDUCTOR DESIGN

The optimal design parameters of any inductor are dependent on the operation requirements of the inductor's application. The operation frequency, f , the input voltage, V_{in} , the current, I and the required inductance, L are expected to be known before the design procedure. The frequency of operation, f is typically the determinant factor deciding the core material of choice. Iron laminations are commonly used at low frequencies (below $1kHz$). For higher frequencies, *Ferrite* cores are provably the more common choice. Core manufacturers typically provide a number of material grades with different losses and magnetic properties suitable for a range of possible applications. In the following paragraphs are summarised the common steps use for gapped inductor design [10].

Step.1. Calculate the required core's Area product, A_p .

One of the more common methodologies for the selection of the core dimensions is based on the core's area product, A_p . The value of A_p , is the product of the core's area cross-section A_c , and its window area W_a , and it provides an intuitive indication of the total core volume and the energy handling capability of the core.

$$A_p = A_c W_a = \frac{L I^2}{\Delta B J K_u} \quad (2.28)$$

Manufacturers typically provide the A_p value of the different standard core shapes and dimensions. The minimally required A_p , of an inductor, is dependent on its inductance and current requirements, as well as the maximum allowed losses. The stored energy on an inductor can be calculated as:

$$W = \frac{L I^2}{2} = \frac{A_p \Delta B J K_u}{2} \quad (2.29)$$

Where W , is the energy in *Watt Seconds* or *Joules*, L is the inductance and I is the current. In this side of the equation, the $L I^2$ product is representative of the energy, in terms of the design requirements of inductance and current. In the other side of the equation, the energy storage capability is defined by the inductor's design parameters. Were J is the current density in the conductor coil and ΔB is the *peak-to-peak* flux density during operation. The maximum achievable ΔB is equivalent to the saturation flux density of the core material, B_{sat} for *DC* operation. For *AC* inductors the maximum achievable ΔB is double of the saturation limit, $2B_{sat}$. On the following design steps has been assumed *DC* operation. The window utilization factor, K_u is representative of the percentage of copper within the total window area. A common inductor typically presents *40 to 80%* of window filled by the windings. The additional space is used by the bobbin and inter-winding spacing.

THEORETICAL BACKGROUND

Step.2. Calculate the minimum required wire's area cross-section, A_w

Higher current density, J will lead to higher thermal losses. The required conductor area cross-section, A_w is dependent on the allowed thermal losses, determined by the operating current and the heat dissipation profile of the design. A current density between 2 to 4 A/mm² is commonly used in multiple layer coils, of solid copper wire, operating below 50KHz with no cooling. Using larger cores (with larger A_p) reduces the required number of turns and provide a larger window area, A_w suitable for thicker coil wires, minimizing heat and resistive losses, at expenses of a higher cost, volume and weight. There is a typical trade-off between compactness and efficiency. Wire's area cross-section, A_w can be calculated using the rms current, I_{rms} and the allowed current density, J using:

$$A_w = \frac{I_{rms}}{J} \quad (2.30)$$

Step.3. Calculate the maximum magnetic flux, ϕ possible in the core.

The maximum allowable flux, ϕ_p (*peak value*) is limit by the core's area cross-section, A_c and the saturation flux density, B_{sat} of the chosen core material:

$$\phi_p = B_{sat} A_c \quad (2.31)$$

The magnetic flux, ϕ can be calculated using Faraday's Law in expression (2.4). Assuming sinusoidal input voltage, equation (2.4) can be rearranged as:

$$\phi_p = \frac{V_p}{N 2 \pi f} = \frac{V_{rms}}{N f K_f} \quad (2.32)$$

Where V_p is sinusoidal input voltage peak value, ϕ_p is the flux peak value, also sinusoidal with a $-\pi/2$ phase shift. K_f is the *waveform factor* and can be calculated, for sinusoidal input voltage, as:

$$K_f = \frac{2 \pi}{\sqrt{2}} \cong 4.44 \quad (2.33)$$

In the case of input voltage, $V_{in}(t)$ being a square waveform, the magnetic flux $\phi(t)$ presents a triangular waveform, with a peak value calculated as:

$$\phi_p = \frac{V_{DC}}{N f K_f} \quad (2.34)$$

Where the waveform factor for square waveform is $K_f = 4$.

PERMANENT MAGNET BIASED INDUCTORS

Step.4. Calculate the minimum required number of turns, N_{min} .

In order to avoid saturation of the core, the minimum required number of turns, N_{min} can be calculate as:

$$N_{min} = \frac{V_{rms}}{\phi_p f K_f} \quad (2.35)$$

Step.5. Calculate the total winding resistance, R_{DC} .

If the wire area, A_W and the number of turns, N are known, the total wire DC-resistance can be calculated as:

$$R_{DC} = \frac{MLT N \rho_{Cu}}{A_W} \quad (2.36)$$

Where ρ_{Cu} is the resistivity of copper with a value of $\rho_{Cu} = 10^{-8} [\Omega m]$ at room temperature ($20^\circ C$). The wire DC-resistance achievable in a core with a fix window area, W_a can be calculate as function of the choosen number of turns, N . Assuming the wire area cross-section, A_W is adjusted in orde to keep constant the window utilization factor, K_u , the DC-resistance can be calculate as:

$$R_{DC}(N) = N^2 \frac{MLT \rho_{Cu}}{W_a K_u} \quad (2.37)$$

Step.6. Calculate the copper losses, P_{Cu} .

The power *copper losses*, P_{Cu} associated with the DC-resistance, R_{DC} of the windings can be calculate as:

$$P_{Cu} = I_{rms}^2 R_{DC} \quad (2.38)$$

Step.7. Calculate the regulation, α .

The regulation is defined as the percentage of the copper losses, P_{Cu} to the total output power, P_o :

$$\alpha = \frac{P_{Cu}}{P_o} (100) [\%] \quad (2.39)$$

THEORETICAL BACKGROUND

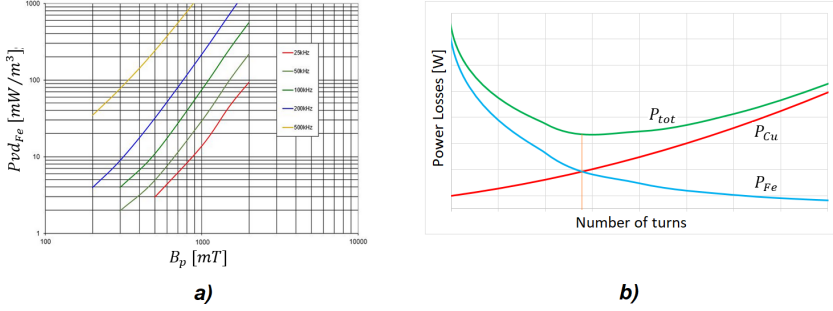


Fig.2.5. Power losses on an inductor. **a)** Volumetric power loss density, Pvd_{Fe} of Ferrite (material grade 78) at $100^{\circ}C$. **b)** Total losses, P_{tot} , iron losses, P_{Fe} and copper losses, P_{Cu} , as function of number of turns. Optimal number of turns with the minimal total losses, P_{tot} marked by orange line.

Step.8. Calculate the iron losses, P_{Fe} .

The *iron losses*, P_{Fe} represent the total power losses dissipated in the ferromagnetic core material. Manufacturers typically provide the *volumetric power density loss*, Pvd_{Fe} of the material, as depicted on the graph in **Fig.2.5.a)**. Volumetric power density losses are quantified in units of $[mW/cm^3]$ or equivalently $[kW/m^3]$. The graph presents the power density losses as function of the *AC magnetic flux density*, B_{AC} , for several operation frequencies. Iron power density losses are also dependent on the operation temperature of the core material. Manufacturers commonly provide several characterisation graphs at different operation temperatures, typically at $20^{\circ}C$. and $100^{\circ}C$. The iron power losses, P_{Fe} of an inductor core operating at a fix frequency, can be calculated using:

$$P_{Fe} = K_{Fe} \Delta B^{\beta} A_C l_m \quad (2.40)$$

Where the coefficients K_{Fe} and β are calculated empirically from the Pvd_{Fe} graph on the material. The product of $A_C l_m$ is representative of the total core volume. Iron losses are dependent on the allowed *peak-to-peak flux density*, ΔB , which can be calculate as a function of the number of turns, N using expression:

$$\Delta B(N) = \frac{V_{rms}}{A_C N f k_f} \quad (2.41)$$

PERMANENT MAGNET BIASED INDUCTORS

Step.9. Calculate the minimal total losses, P_{tot} and associated number of turns, N .

The total power losses can be estimate by the addition of copper and iron losses, as:

$$P_{tot} = P_{Cu} + P_{Fe} \quad (2.42)$$

Fig.2.5.b) shows the total losses, P_{tot} and the independent contribution of iron and copper losses, P_{Cu} and P_{Fe} as function of the number of turns, N . The calculation uses equations (2.37),(2.38),(2.40) and (2.41) and assumes the same core area product, A_p and inductance, L value are fixed. Increasing the number of turns, N leads to lower flux density, ΔB and lower iron losses, P_{Fe} , at expenses of higher DC resistance and copper losses, P_{Cu} . Reducing the number of turns, N leads to lower copper losses, P_{Cu} at expenses of higher flux density, ΔB and iron losses, P_{Fe} . The minimum total losses, P_{tot} are achieved when the copper and iron losses are equilibrated: $P_{Cu} = P_{Fe}$.

Step.10. Calculate the required *flux linkage*, λ .

The *flux linkage*, λ is equivalent to the LI product. The product of the required maximum peak current, I_p and the nominal inductance, L_N must satisfy:

$$L_N I_p \leq LI = N \phi_{max} = N B_{Sat} A_C \quad (2.43)$$

Where, B_{Sat} is the core's saturation flux density, A_C is the core's area cross-section and N is the number of turns of the coil. The LI product is a constant which defines the maximum achievable area for the $LvsI$ profile of a given inductor design. A normalized LI product is depicted by the blue lines in **Fig.2.6**. The product of the number of turns, N the saturation flux density of the material, B_{Sat} and the area cross-section, A_C of the core, needs to be equal or bigger than the required LI product.

Step.11. Calculate the *airgap length*, l_g .

Assuming the total reluctance of the magnetic path is dominated by the airgap, the nominal inductance, L_N can be calculated by:

$$L_N = \frac{N^2}{\mathcal{R}_g} \quad (2.44)$$

Where the reluctance of the airgap, \mathcal{R}_g can be calculate by:

$$\mathcal{R}_g = \frac{l_g}{\mu_0 A_g} \quad (2.45)$$

THEORETICAL BACKGROUND

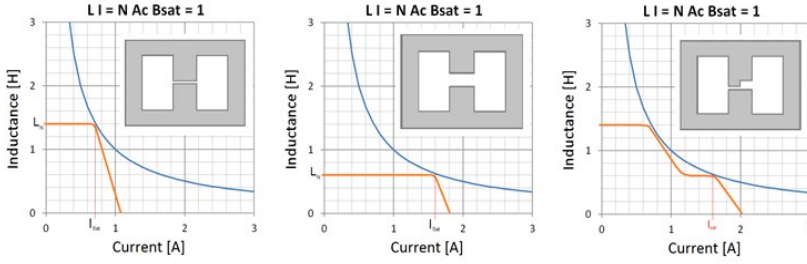


Fig.2.6. Inductance as function of current, $LvsI$ of an inductor for three different airgap lengths. Blue curve defines a normalized LI product region. Orange line represents the $LvsI$ for each airgap length. *Left: short airgap; Center: long airgap; Right: airgap with non-constant length. Figure from [26]*

Where l_g is the length of the airgap along the flux axis, μ_0 is the permeability of vacuum and A_g is the airgap's area cross-section. In order to account for the effect of fringing flux near the airgap, a rectangular airgap with dimensions: $[l_x, l_y, l_g]$, can be approximated as:

$$A_g = (l_x + 2l_g)(l_y + 2l_g) \quad (2.46)$$

In **Fig.2.6.** It is shown approximate $LvsI$ curves of three hypothetical airgap's lengths. The longer the airgap, the bigger the reluctance and lower the linear inductance, L_N value. The saturation current starts the value at which the nominal inductance, L_N crosses with the LI product limit (blue line). *Saturable airgaps*, presenting non-constant area along its length, produces non-linear $LvsI$ profiles. Inductors with higher inductance, L_N at low currents levels, have been used to provide a better output voltage ripple in converters operating at lower power loads [15].

2.4. INTRODUCTION TO PERMANENT MAGNETS

Every magnetic field is generated by an associated electric current. The magnetic field of a permanent magnet is also produced by moving electric charges, generated by the organised electron spin and orbit within the permanent magnet material. Permanent magnets, *PMs* are used as the source of the required bias *magnetic flux*, ϕ_{bias} in *PMBIs*. The selection of the *PM's* material and its dimensions are the additional design parameters of *PMBIs*. The demagnetization curves of a *PMs*, as depicted in **Fig.2.7.left**, provide the main parameters required for the characterization of the *PM's* material. The *magnetic polarization*, J achieved in the *PM* material as function of the *magnetic field strength*, H , is referred as the intrinsic curve, JH . The characterization of the the intrinsic curve, JH is tested on the material sample under a condition of

Demagnetization Curves and Energy Storage of a Lineal Permanent Magnet

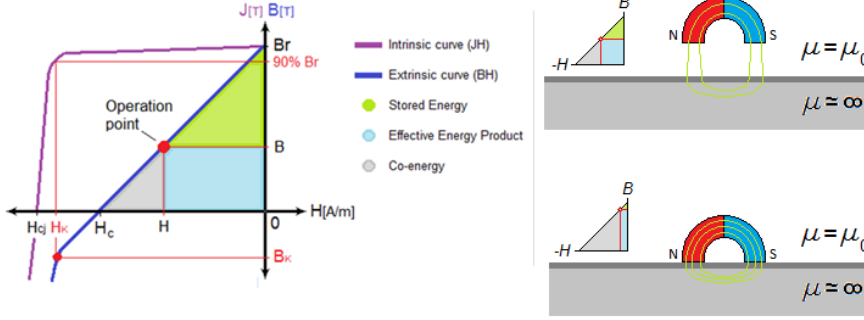


Fig.2.7. Demagnetization curves of a lineal PM (left), and example of energy stored on a PM (right).

magnetic short circuit. After being magnetized, the operation point and the flux density, B of the PM 's material is defined by the extrinsic curve. The total PM 's flux, ϕ_{PM} can be calculated as a function of the PM material characteristics, its area-cross section, and the applied field strength, H , by:

$$\phi_{PM} = A_{PM} B = A_{PM} (B_r + \mu_{PM} H) \quad (2.47)$$

Where ϕ_{PM} is the PM 's magnetic flux, A_{PM} is the area cross-section, B is the magnetic flux density, B_r and μ_{PM} are the remanent flux density and the permeability of the PM 's material. When the PM is not in a short-circuit condition and no magnetic field strength, H is applied against the PM , the operation point is dependent on the reluctance of the medium containing the flux of the PM , and can be calculated using:

$$\phi_{PM} = \frac{H_c l_{PM}}{\mathcal{R}_{PM} + \mathcal{R}_l} \quad (2.48)$$

Where, H_c represents the PM 's coercive force, and l_{PM} is the length of the PM along the magnetization axes. \mathcal{R}_{PM} is the magnetic reluctance of the PM and \mathcal{R}_l is the load reluctance between the PM 's poles. The effective magnetic energy product of the PM , is dependent on its operation point, as depicted by the blue area in **Fig.2.7**. By increasing the load reluctance, \mathcal{R}_l , the PM 's operation point decreases, and energy is stored in the PM , as represented by the green area in **Fig.2.7**. The grey area is representative of the magnetic co-energy, which can be define as a dual mathematical

THEORETICAL BACKGROUND

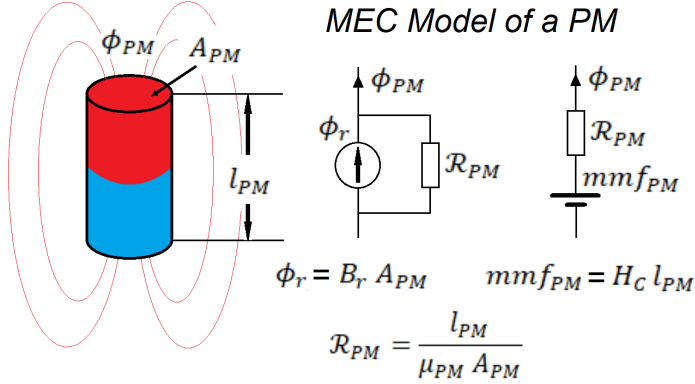


Fig.2.8. MEC models of a PM. Current source or voltage source and related formulas.

formulation to define the storage of energy. Co-energy is often used to compute forces and torque on *PM electric motors*. An intuitive understanding of the energy sourcing and the storage capability of *PMs*, can be envision with the example presented in **Fig.2.7.right**. In the situation depicted in the bottom, a U shape *PM* rest with its poles in direct contact with an ideal magnetic conductor with extremely high *permeability* and no saturation flux density limit. The *load reluctance*, \mathcal{R}_l is minimal or hypothetically zero, and the magnetic *flux density*, B sourced by the *PM* is maximal or equal to B_r . In this situation, the *PM* can be understood as being in a *short-circuited* condition. Even if the sourced *magnetic flux*, ϕ_{PM} is maximal, the *magneto-motive force*, F at the *load reluctance*, \mathcal{R}_l is minimal or zero. Accordingly, the sourced magnetic energy at the *load reluctance*, \mathcal{R}_l (blue area), and the energy stored in the *PM* (green area) are zero. In the situation depicted at the top of **Fig.2.7.right** a force is being apply in order to lift the *PM* from its resting position, and hold it at certain distance away from the ideal perfect magnetic conductor. The space between the *PM* and the ideal magnetic conductor increases the *load reluctance*, \mathcal{R}_l and the operation point of the *PM* is lowered. The *PM* can now source a certain *magneto-motive force*, F and magnetic energy into the non-zero *load reluctance*, \mathcal{R}_l . It can be graphically appreciated that there is an optimal *PM's* operation point, which yield the maximum sourced *BH* energy product. Similar to the common calculation for the *maximum power transfer* of electric sources, the maximum magnetic energy product is achieved when the *load reluctance*, \mathcal{R}_l is equal to the *PM's reluctance*, \mathcal{R}_{PM} . The energy required to lift the *PM* out of its equilibrium point at magnetic short-circuit, has been stored in the *PM* as represented by the green area. If releasing the force which hold the *PM* above the ideal magnetic conductor, the stored energy would be released as the *PM* reaches its original resting point in a *short-circuit* condition in contact with the ideal conductor. Two possible MEC models of a bar *PM* is depicted in **Fig.2.8**.

PERMANENT MAGNET BIASED INDUCTORS

PMs can be simulated as a current source of value equal to the *remanent magnetic flux*, ϕ_r in parallel with the *PM's reluctance*, \mathcal{R}_{PM} , or a voltage source equal to mmf_{PM} in series with the *PM's reluctance*, \mathcal{R}_{PM} . These models are typically sufficient to characterize a *PMs* presenting a linear extrinsic curve. Most of the grades of rare-earth *PM* materials (*NdFeB* or *SmCo*) can be characterized with a linear extrinsic curve, as depicted in **Fig.2.7.a**). If the operation point of the *PM* is maintained within the linear region, the *PM* will not present demagnetization damages. The threshold for demagnetization damage of the *PM* is delimited by the knee-point at the extrinsic curve. Common *PM* materials present different demagnetization curves as different temperatures. The threshold for demagnetization damage is lower at higher temperatures. The maximum demagnetization field strength, H at the expected *PM* temperature at maximum power must be below the demagnetization damage threshold, H_k [39][40].

3. STATE OF THE ART

This chapter starts with a summary of the theoretical benefits of *PM* biasing and the possible *PMBI* design strategies, followed by the historical evolution on the different *PMBI* topologies. Finally, the practical performance of the different physical implementations documented in the literature are summarise and evaluated.

3.1. THEORETICAL BENEFITS OF *PMBI* DESIGN STRATEGIES

As depicted in **Fig.1.4**, the biasing magnetic flux introduced by the permanent magnet, can shift the centre of the operation point (at OA) of the *BH* loop of the ferromagnetic core. Therefore, *PMBIs* can provide a higher maximum flux density increment, $\Delta B_{PMBI} = B_{bias} + B_{sat}$ compared to standard, (*STD*) non-biased inductors with equivalent dimensions, $\Delta B_{STD} = 0 + B_{sat} = B_{sat}$. The current, inductance and design limits associated for a maximum ΔB , were defined in equation (2.43) and can be expressed as:

$$\Delta B_{STD} = 0 + B_{sat} = \frac{L I_{sat}}{A_c N} \quad (3.1)$$

Comparatively can be defined the *biasing improvement factor*, *BIF* of the *PMBI* design as function of the achieve bias:

$$BIF = \frac{\Delta B_{PMBI}}{\Delta B_{STD}} = \frac{B_{bias} + B_{sat}}{B_{sat}} \quad (3.2)$$

And the design limits of the associated *PMBI*'s flux density increment, ΔB_{PMBI} can be expressed as:

$$\Delta B_{PMBI} = BFI \Delta B_{STD} = \frac{B_{bias} + B_{sat}}{B_{sat}} \frac{L I_{sat}}{A_c N} \quad (3.3)$$

Where L , I_{sat} , A_c , and N are the design parameters of the standard non-biased reference design. Full linear bias, or *100%* bias, can be defined when all the linear region of the core's *BH* loop has been shifted to the first quadrant, and therefore bias flux is equal to saturation flux density of the core, $B_{bias} = B_{sat}$. A *100%* biased core presents a *biasing improvement factor*, $BFI = 2x$, on the product of the design parameters: L , I , $1/N$, or $1/A_c$, as indicated in (3.3).

PMBI design strategies

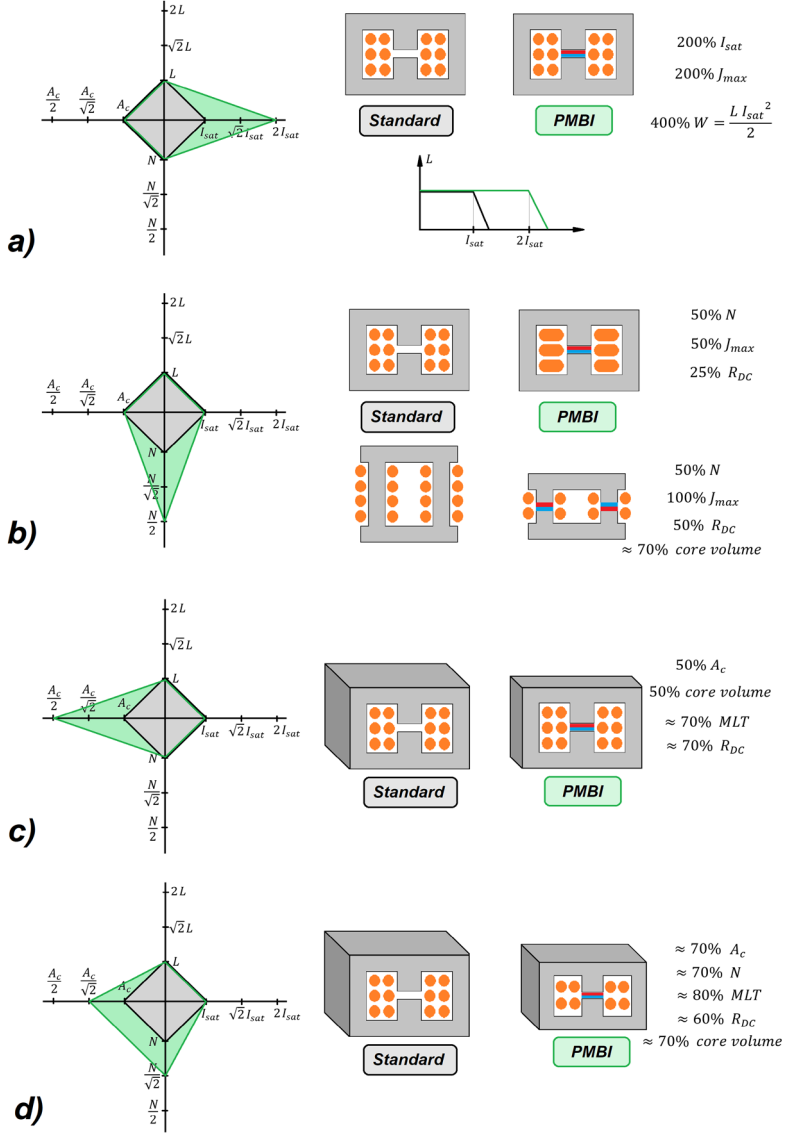


Fig.3.1. Examples of possible PMBI design strategies and associated improvements. 100% biasing ($BFI = 2$) is assumed. Design strategies' Improvement factor BFI : **a)** 2x saturation current, I_{sat} ; **b)** x0.5 number of turns, N ; **c)** x0.5 core's area cross-section, A_c . **d)** x0.707 area cross-section, A_c and x0.707 number of turns, N .

STATE OF THE ART

A smaller percentage of bias magnetization, B_{bias} will allow for a proportional factor of design improvements. The total *improvement factor*, BFI achieved can be utilised by different design strategies and distributed among different design parameters. **Fig.3.1** presents some of the possible and more common choices for assignment of BFI in *PMBI* designs. These examples and the associated design improvements are calculated assuming 100% biasing, achieved by a theoretical *PMBI* ideal topology.

The optimal choice for the distribution of the improvement factor, BFI among the design parameters: L , I , $1/N$, or $1/A_c$, is dependent on the specific core geometry and the priorities associated with the specific inductor applications. One of the common possibilities consist of utilizing the BFI for increasing the saturation current, I_{sat} , while maintaining the same core size and number of turns, as represented in **Fig.3.1.a**). This design strategy increased the energy density to 400% the value of a standard non-biased inductor, while increasing to 200% the maximum current density, J_{sat} , and its associated conduction losses.

The optimal design strategy is dependent on the requirements associated with the operation conditions. Applications operating at high *DC* current levels and with small *AC* current ripple or low ripple frequency, are typically limited by *DC* losses, and will benefit from a reduced *DC* resistance, R_{DC} . **Fig.3.1.b**) presents a design strategy with 50% number of turns, N . Two main possibilities are associated with this strategy:

- The wire's area cross-section, A_w can be doubled with the same fill factor in the original window area, W_a . This strategy results in 25% of the R_{DC} value compared to a non-biased reference design, while presenting the same total inductor volume.
- Keeping the same wire's area cross-section, A_w with half the turns results in 50% the reference *DC* resistance R_{DC} . This strategy requires only half of the original window area, W_a , and a core with the same area cross-section A_c , and reduced magnetic length, l_m can be utilized, resulting in approximately 70% of the reference core volume.

Fig.3.1.c) presents a design strategy based on 50% reduction of the core's area cross-section, A_c . This strategy is preferred in applications where achieving minimal weight and compactness are the highest priority. It achieves 50% core weight and volume and a reduced *mean length per turn*, MLT of approximately 70% its original reference value, resulting in 70% the reference *DC* resistance R_{DC} .

The total improvement factor, $BFI = \mathbf{x2}$ (100% bias) could also be distributed among several of the design parameters. **Fig.3.1.d**) present a design strategy example where the improvement factor is distributed between $1/N$ and $1/A_c$, allowing for a factor of $\mathbf{x0.707}$ the required number of turns, N and an additional factor of $\mathbf{x0.707}$ the required core's area cross-section, A_c . This strategy can achieve approximately 70% of the reference core volume and 60% the reference *DC* resistance R_{DC} .

PERMANENT MAGNET BIASED INDUCTORS

These theoretical improvements are calculated assuming 100% bias achieved with an ideal *PMBI* topology with identical core size with *PM* inside the airgap. In practicality, achieving 100% biasing without any detrimental effects on the *PM*'s lifetime or the inductor's performance is not easily achievable, and newer *PMBI* topologies are in constant improvement and evolution.

3.2. EVOLUTION OF *PMBIS* TOPOLOGIES

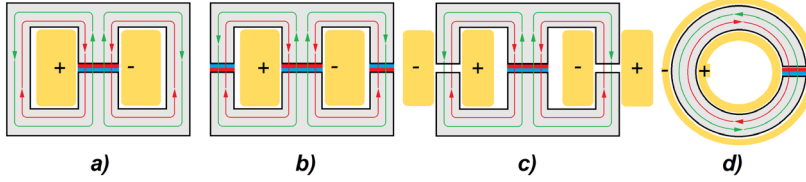
Fig.1.5. present the timeline of scientific publications about permanent magnet biased inductors, *PMBIs*. The development and possibilities of *PMBIs* has been closely dependent on the historical evolution of *PM* materials. The first *PMBIs* date back to the late 1950's, when the first ferrite magnets were developed. The higher electric resistivity and magnetic coercivity, H_c of barium ferrite magnets, compared to the preceding *AlNiCo* magnets, became a key technological development that allowed for the *PM* biasing technique. Approximately twenty years later, in the 1980's, the advancements in material technology provided the next generation of *rare-earth PMs*. These new *PM* material compounds, like *Neodymium Iron Boron*, *NdFeB* and *Samarium Cobalt*, *SmCo*, can achieve higher levels of remanent flux density, B_r and magnetic coercivity, H_c enhancing the possibilities in the development of *PMBIs*. The proceeding continuous development of stronger grades of *rare-earth PMs* in the 90's and the development of *polymer bonded rare-earth PMs*, has greatly enhance the practical possibilities of inductor biasing, and the scientific interest on the subject seems to be reawakened, as seen in **Fig.1.5**. These newer *rare-earth* magnetic compounds can provide higher levels of magnetic flux and better resistant against demagnetizing fields. The electric resistivity of the *PM* material is also a critical factor with a dominant impact on the highest frequency of usability of the *PMBI*. High

PM Material	Br [T]		Hc [kA/m]		Hcj [kA/m]		μ_r	Resistivity ρ
	min	max	min	max	min	max		
Sintered Neodymium. NdFeB	1	1.2	780	915	955	2388	1 - 1.1	$\approx 150 \mu\Omega\text{-cm}$
Sintered Samarium Cobalt. SmCo	0.9	1.1	600	800	1200	1440	1 - 1.2	$\approx 100 \mu\Omega\text{-cm}$
Bonded Neodymium. NdFeB	0.3	0.76	160	517	398	875	1.2 - 1.5	$> 10 \text{ k}\Omega\text{-cm}$
Barium Ferrite.	0.2	0.4	125	288	210	280	1.1 - 1.3	$> 1 \text{ M}\Omega\text{-cm}$

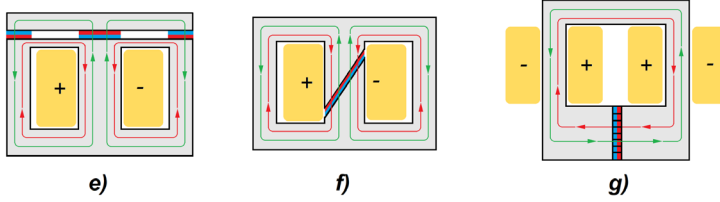
Table 3.1. Magnetic characteristics of available grades of common Permanent Magnet materials.

Permanent Magnet Biased Inductor's Topologies

Permanent Magnet inside the air-gap



Improvements over Permanent Magnets inside the air-gap



Permanent Magnets outside the air-gaps

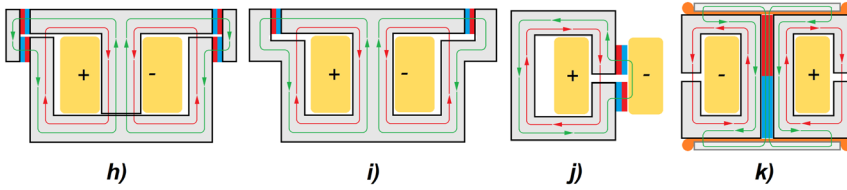


Fig.3.2. Permanent Magnet Biased Inductor Topologies. Red vectors represent magnetic flux induced by the coils. Green vectors represent magnetic flux induced by the permanent magnets. Yellow areas represent windings. Current direction: + is into the page; - is out of the page.

electric resistivity is required at higher frequencies, due to the losses associated with the effect of eddy currents. The latest developments of rare earth bonded compounds can provide relatively strong *PMs*, while greatly enhancing the electric resistivity of the *PM* material and extending the *PMs* usability at higher frequencies. Since 2002 until the present days, the number of scientific publications in the field of *PMBIs* has been increasing with time. **Table 3.1.** presents a summary of the magnetic characteristics achieved by the range of *PM's* grades available within each magnetic material. Different core materials presenting a specific saturation flux density, B_{sat}

PERMANENT MAGNET BIASED INDUCTORS

require an equivalent amount of magnetic biasing flux density, B_{bias} supplied by the *PM*. The more commonly used core materials are:

- Silicon iron, *SiFe* laminations: Used in lower frequency applications ($<1\text{kHz}$). Saturation flux density, B_{sat} in the range from 1 T to 1.6 T .
- Ferrites, *MnZn-FeO* and *NiZn-FeO*: For higher frequency applications, up to 200 kHz and up to 1 MHz respectively. Saturation flux density, B_{sat} in the range from 0.3 T to 0.5 T .

Ferrite and *SiFe* lamination cores present different requirements on the bias flux density, B_{sat} and electric resistivity of the *PM* material. Sintered *NdFeB* or *SmCo* presenting the highest remanent flux density, B_r , and the lowest resistivity, can be employed in *PMBIs* using *SiFe* laminations in low frequency applications. Ferrite cores, requiring a lower B_{bias} and operating in high frequency applications, can be biased with the use of *polymer bonded NdFeB* magnets, presenting a much higher electric resistivity compared to sintered *PMs*.

The specific topologies employed to introduce the *PM*'s biasing flux into the magnetic core, have also been evolving over the years. **Fig.3.2.** presents the schematic flux diagrams of the different core and *PM* topologies used by different authors in the development of *PMBIs* [11]-[23]. The green vectors are representative of the magnetic flux introduced by the *PMs*. The red vectors represent the magnetic flux induced by the current on the windings. Magnetic biasing is achieved in the sections of the core presenting these two vectors in opposite directions.

3.2.1. Topologies with PM inside the airgap

The first scientific publications on the subject [11]-[14], date back to the late 50's and present a theoretical analysis and an optimization procedure for the first *PMBIs* topology. This first *PMBI* topology consist of standard gapped cores with a *PM inside the airgap* as depicted in **Fig.3.2.a),b),c), and d)**. This biasing technique can be implemented in any standard gapped core shapes, *EE*, *UU*, gapped toroid. This pioneering idea appeared as the more intuitive approach to introduce the desired opposing bias flux, B_{bias} into the inductor's core. This topology can introduce a certain level of bias flux and achieve a proportional improvement factor, *BFI* on the design. On the other hand, this first topology having the *PM* inside the airgap, exposes the *PM* to strong demagnetizing forces at saturation current, I_{sat} . A common technique employed to reduce the demagnetization field and maintain the operation point of the *PM* above its permanent demagnetization threshold, H_K , is to introduce airgaps in between the *PM*'s and the core's surfaces, as depicted in **Fig.3.3**. As can be understood by the *MEC* representation, the airgaps reluctances, $\mathcal{R}_{air-gap}$ absorb part of the demagnetizing *mmf* introduced by the coil's current on the *PM*. On the other hand, the airgaps reluctances, $\mathcal{R}_{air-gap}$ increases the total load reluctance, \mathcal{R}_l seen by

STATE OF THE ART

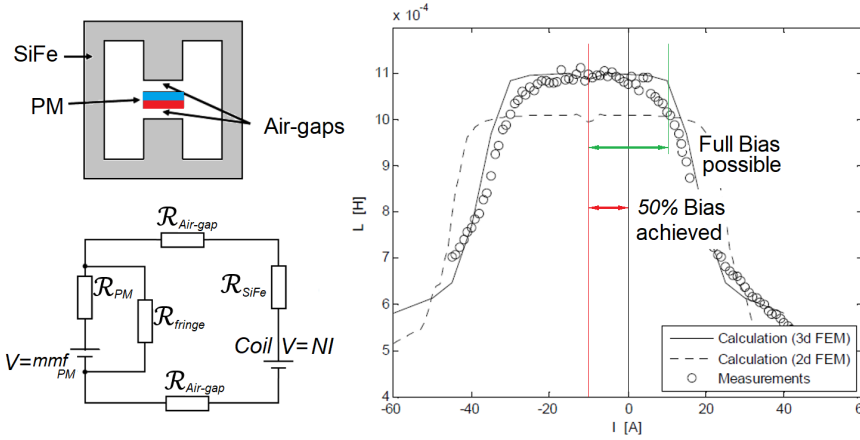


Fig.3.3. PMBI topology with PM inside the airgap. Left: Basic PMBI topology and MEC representation. Right: **LvsI** profile of a PMBI, empirical measurements and predictions with 2D and 3D FEA [19].

the PM, lowering its operation point (2.48) and the achievable bias flux, B_{bias} . Nevertheless, the basic topology with PMs inside the airgap has been documented to achieve design improvements in both ferrite and SiFe laminations inductors operating in different DC applications [18][19][31][32][34].

3.2.2. Topology improvements with PM inside the airgap

In order to minimize the limitations of the basic topology, reducing the demagnetizing mmf on the PMs and increasing the available PM's area cross-section, several possible design improvements over the basic topology with "PMs inside the airgap" has been documented [11]-[15][33]. The authors of the earliest publications presented a creative solution, using special design cores with *angled airgaps* [11]-[14]. **Fig.3.2.f)** shows a schematic of this proposed non-standard core topology. The angular orientation of the gap increases the available surface, allowing for higher PM's area and higher levels of bias magnetic flux. Additionally, the demagnetizing field induced against the PM, is reduced using angular airgaps. These theoretical improvements are achieved at expenses of requiring non-standard cores with angled airgaps. Unfortunately, no physical PMBI implementations using *angled airgaps* have been found as products on the market or documented in the scientific literature.

The topology depicted in **Fig.3.2.e)** was utilized by the first PMBI commercial product, developed by TDK in the early 80's and termed the PCH coil. This topology uses a non-standard core shape with a saturable section besides the PM-airgap. This

saturable portion of the core greatly reduces the demagnetizing field on the *PM*, while increasing the inductance at low current levels. This non-linear inductance profile is beneficial in converter applications, adding extra inductance and stability at low *DC* load current operation. At the time of this development, barium ferrite *PMs* was the highest performance *PMs* available. Nevertheless, the *PCH coil* achieves 30% biasing allowing for 30% higher I_{sat} compared to a non-biased inductor with the same dimensions [15].

The topology depicted in **Fig.3.2.g)** present a *UU* core biased by a *PM* inside the airgap, located on a section of the core with a larger area cross-section [33]. This strategy increases the available *PM*'s area and therefore the achievable bias flux. This *PMBI* implementation using *SiFe* core and sintered *NdFeB* *PMs* is documented to achieve 75% biasing flux and 35% reduction in number of turns, N [33].

3.2.3. Topologies with *PMs* outside the airgap

In order to overcome the limitations associated with the *PM* inside the airgap, a common trend has been in the direction of developing topologies using non-standard core shapes and placing the *PMs* near the airgaps. Four different topologies have been documented, employing *PMs outside the airgap* in [17][20]-[22][28][35]-[37]. The schematic diagram of the specific core and *PM* topologies used on these publications can be seen on **Fig.3.2.h),i),j),** and **k)**. These newer topologies provide a secondary magnetic circuit, for guiding the *PM*'s flux inside the core. By placing the *PMs* outside of the airgap, the opposing demagnetizing field induced at the *PMs* poles is significantly reduced, optimizing the lifetime and the operation point of the *PMs*. These topologies require non-standard core shapes and/or additional material segments used to guide the *PM*'s flux, which also contribute to the total volume of the core. Placing the *PMs* outside the coil's flux path also present some challenges for introducing biasing flux in the totality of the core, resulting in non-biased core segments near the airgap, and presenting partial saturation and a small reduction of the inductance value at high currents [35].

The first scientific publication documenting a *PMBI* with non-standard core shape and *PMs near the airgap*, appeared in 2001 [17]. The authors employed the topology presented in **Fig.3.2.h)** and *MEC* analysis was used for this *PMBI* design. To make final adjustments in inductance and saturation current of the *PMBI*, the thickness of the core segments linking the *PMs* was used as an adjustment parameter.

A very similar *PMBI* topology (**Fig.3.2.i)**) has been documented in [20][21][22], employing ferrite core and sintered *NdFeB* *PMs*. A comparison of the design achievements of: non-biased *EI* core inductors, *PMBIs* using the basic topology with *PM inside the airgap* (**Fig.3.2.a)**) and *PMBIs* with *PMs* outside the airgaps using the topology in **Fig.3.2.i)**, has been analysed with the use of software simulations, and the comparison results are presented in **Fig.3.4**. Authors in [20] presents a comparison of the simulated optimal fronts of *mass vs losses*, of standard *EI* core inductors and

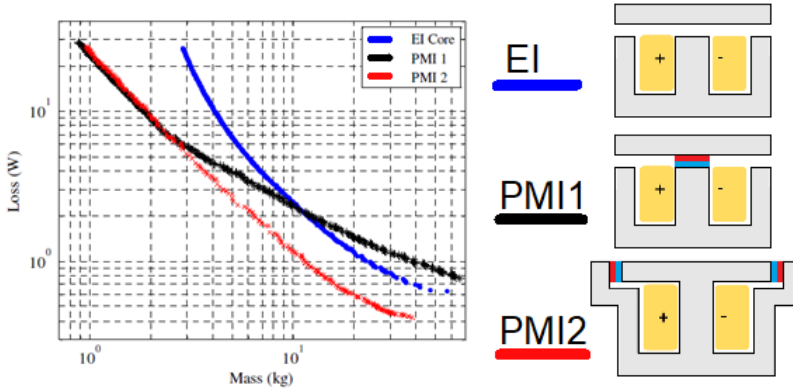


Fig.3.4. Pareto-optimal fronts of losses vs mass of different inductor designs. Calculated with MEC analysis coupled to population base algorithms. The blue curve represents standard non-biased EI designs. The black curve represents designs with the topology in **Fig.3.1.a)**. The red curve represents designs with the topology in **Fig.3.1.e)**. *Source of the figure: [21].*

PMBIs with the topology shown in **Fig.3.2.i)**. A high frequency ferrite, grade 3C90, has been used as core material in the simulations. The length and thickness of the different core segments and airgaps, the number of turns and the winding area are submitted as optimization variables for a *PBA*. This algorithm finds the optimal value for the submitted variables, within a specified range, in order to achieve the minimum volume-losses product. The inductor's rated inductance and current are set as target requirements. Constraint limits for the maximum flux density in the core material, the maximum demagnetizing field induced in the *PM* and the maximum current density in the windings, were introduced in the algorithm. The calculations required for the population algorithm were provided by a *MEC* analysis. The losses calculation only considers the copper losses. The same procedure is done for the design calculations of non-biased standard *EI* cores. The pareto-optimal front of *mass vs losses* with the two different topologies is calculated and compared. The calculation is targeting an inductance on 2.6 mH at a rated current of 20 A. The presented results, shows that the proposed *PMBI* topology can achieve the same inductance, operating current, and losses requirements with 40% less mass. In [21] the same analysis is calculated on the basic *PMBI* topology, using standard *EI* cores with a *PM* inside the airgap, as depicted in **Fig.3.2.a)**. The calculated pareto-optimal fronts of *mass vs losses* of the standard *EI* and the two different *PMBI* topologies are presented in **Fig.3.4**. It can be noticed that the topology presented in **Fig.3.2.i)** possess the best compromises. The required mass for this topology is approximately 40% lower compared to the non-biased *EI* inductor. The basic topology depicted in **Fig.3.2.a)** is slightly less massive for designs allowing high losses. On the other hand, for designs requiring lower losses, the basic

topology quickly becomes the more massive. These results provide an intuitive indication of the size reduction benefits of using these different *PMBI* topologies.

The topology depicted in **Fig.3.2.j**), present the *PMs* in the side of the core near the airgap [37]. It uses a standard *UU* core shape, and the biasing flux presents a portion of its magnetic circuit outside the *UU* core, without using any ferromagnetic material segments for containing and guiding the *PMs* flux. The demagnetization field on the *PMs* outside the airgap is greatly minimized. By placing the *PMs* on the sides of the core, the maximum allowable *PM's* area cross-section A_{PM} is enhanced compared with the basic topology. On the other hand, having a portion of the biasing flux on the air (without a ferromagnetic conductor) greatly increases the *PM's* load reluctance, reducing the *PM's* operation point and the achievable bias flux, B_{bias} . Nevertheless, this topology has been documented using nanocrystalline *UU* core, with saturation flux density, $B_{sat} = 1.2\text{ T}$, and achieving up to 30% bias flux. This topology employed special *laminated-sintered NdFeB PMs*, allowing for a great increase in the total *PMs* resistivity and resulting in 90% lower eddy current losses compared to standard sintered *NdFeB PMs*.

The latest topology documented with *PMs* outside the airgap, employs a new technique utilizing a standard ferrite pot core, as depicted in **Fig.3.2.k**) [36]. A sintered *NdFeB PM* is inserted in the hollow central axis of the ferrite pot core, and additional ferromagnetic plates are used to guide the *PM's* flux into the outer sides of the pot core. These guiding plates are made of *Hiperco-50*, providing very high permeability and saturation flux density, which allows for the use of relatively thin plates. In order to reduce the expected eddy current losses in the *PM* and *Hiperco-50* plates, this topology includes a copper shield in between the ferrite and the *Hiperco-50* plates. The documented prototype achieves 45% bias flux, and successfully reduces the required number of turns, achieving a 50% reduction in *DC* resistance, R_{DC} .

3.3. PHYSICAL *PMBI* IMPLEMENTATIONS

3.3.1. Implementations with *PMs* inside the airgap

Six different publications have been found documenting empirical measurements on physical *PMBI* implementations using topologies with *PMs* inside the airgaps [18][19][31]-[34]. **Table.3.2.** presents a summary of the *PMBI* characteristics, the chosen design strategies, the biasing flux achieved, the operating conditions and their performance achievements and limitations.

Reference [18] presents the first documented physical implementation of the basic topology, with *PM inside the airgap*, **Fig.3.2.a**). This *PMBI* prototype is employ for miniaturization of a *fly-back converter* for a computer power supply. The used core material is high frequency ferrite. The converter nominal current is 6A and it operates at a frequency in the range of 100kHz. At this relatively high frequency, the eddy

STATE OF THE ART

Ref. Nr.	Publication Title PMBI Topology / Implementation	Year	Core material	PM material	Electrical Specifications	Bias % $BIF = \frac{B_{bias} + B_{sat}}{B_{sat}}$	Design Strategy Achievements
[18]	"A new downsized large current choke coil with magnet bias method"	2003	MnZn Ferrite FEY28	Bonded NdFeB	Frq 100 kHz L 0.7 uH I _{dc} 23 A I _{pp} Not specified	60% $BIF = 1.6$	Compared with equivalent inductance and saturation current. 32% less core volume Equivalent DC resistance.
[19]	"Design of a high-temperature pre-biased line choke for power electronics applications"	2008	SiFe Laminations	Sintered SmCo	Frq 10 kHz L 1 mH I _{dc} 32 A I _{pp} 3.2 A	50% $BIF = 1.5$	Compared with equivalent inductance and saturation current. 30% less core volume. 10% less total volume. Equivalent DC resistance.
[31]	"Evaluation of High-Current Toroid Power Inductor With NdFeB Magnet for DC-DC Power Converters"	2015	Ferrite 3C20	Sintered NdFeB N35EH	Frq 300 kHz L 7 uH I _{dc} 14 A I _{pp} 0.6 A	100% $BIF = 2$	Compared with equivalent inductance and saturation current. 40% less core volume. Equivalent DC resistance.
[32]	"Permanent-Magnet Coupled Power Inductor for Multiphase DC-DC Power Converters"	2017	Ferrite N87	Sintered NdFeB N35EH	Frq 150 kHz L 4 uH I _{dc} 22 A I _{pp} 0.5 A	92% $BIF = 1.92$	Compared with the same inductor without PMs. 92% higher saturation current. 48% core volume reduction compared to standard non-biased coupled inductors.
[33]	"Premagnetization of High-Power Low-Frequency DC-Inductors in Power Electronic Applications"	2019	SiFe Laminations	Sintered NdFeB	Frq Not specified L 1.3 mH I _{dc} 60 A I _{pp} Not specified	75% $BIF = 1.75$	Compared with equivalent inductance and saturation current. 35% less number of turns. 35% lower DC resistance. Approx. 10% smaller core volume.
[34]	"Premagnetized Inductors in Single Phase dc-ac and ac-dc Converters"	2019	Ferrite (grade not specified)	Bonded NdFeB	Frq 400 kHz L 240 uH I _{dc} 5 A I _{dc} 2 A I _{pp} 28 A	100% $BIF = 2$	Compared with the same inductor without PMs. 100% higher saturation current. Equivalent DC resistance.

Table 3.2. Summary of *PMBI* implementations using topologies with *PMs* inside the airgaps.

currents on the surface of the magnet will become a critical limiting factor. Measurements of the inductor's *quality factor*, Q with two different *PM* materials are presented. The tested *PMs* materials are *sintered* and *bonded NdFeB*. Sintered magnets offer the highest flux density at expenses of a quite low electric resistivity. Bonded magnets are a compromise solution having lower flux density while having a

high resistivity value. The *PMBI* using the sintered magnet achieves higher biasing levels. On the other hand, the eddy currents on the *PM* introduce new losses and lower the Q value of the inductor, limiting its usability. Despite their lower flux density, bonded magnets are the preferred choice due to their lower eddy current losses. The achieved bias flux is 40% of the maximum allowable flux. Nevertheless, the presented design achieves 30% of volume reduction compared to a standard non-biased design while presenting the same inductance and quality factor Q .

Two different physical implementations are documented achieving 100% biasing of ferrite cores using the topologies with sintered *NdFeB* *PMs* inside the airgap, depicted in **Fig.3.2.c)** and **d)** [31][32]. These *PMBIs* are documented to achieve up to 48% core volume reduction. Using this combination of core and *PM* material 100% biasing is easily achieved. 3D FEA simulations were used to verify that the demagnetization force mmf on the *PMs*, at maximum current, I_{sat} is successfully kept below the demagnetization threshold, H_k of the chosen sintered *PM*'s material grade. On the other hand, the low resistivity of the *PM* material will introduce significant *AC* losses on the *PMs*. Unfortunately, no empirical measurements are provided of the achieved quality factor, Q or *AC equivalent series resistance*, ESR of these *PMBI* prototypes. Nevertheless, these topologies are suitable and oriented for applications presenting a relatively high *DC* current, I_{DC} and a relatively smaller *AC* current ripple, I_{pp} .

The topology depicted in **Fig.3.2.b)** has been employed with ferrite cores and polymer bonded *PMs* [34]. The use of bonded *NdFeB* material, greatly increases the *PMs* resistivity and minimizes the *AC* eddy current losses. This implementation successfully achieves 100% bias flux and increases the saturation flux density, I_{sat} to double its non-biased value, from $I_{sat} = 14\text{ A}$ to $I_{sat} = 28\text{ A}$. Since the prototype does not include additional airgaps in between the *PMs* and the core, it could be expectable to reach the demagnetization threshold at maximum current. Unfortunately, the magnetic field strength, H_k of the demagnetization limit of the *PM*, or the present demagnetizing force, mmf produced against the *PMs* surface at maximum current, I_{sat} has not been specified. The prototype is operating on a unipolar *DC-AC* converter, with a low frequency *AC* of $I_{AC} = 5\text{ Arms}$ and a high frequency current ripple of approximately $I_{pp} = 2\text{ A}$. The current range of the tested application, is relatively low, compared with its available saturation current limit, $I_{sat} = 28\text{ A}$.

The first *PMBI* using *SiFe* laminations and the topology with *PM inside the airgap* (**Fig.3.2.a)**) has been documented in [19]. The inductor is required to provide an inductance of 1 mH , operating at a *DC* current of 32 A . The frequency of the current ripple is 10 kHz and the *peak-to-peak* current is only 3.2 A . Since the ripple's amplitude and frequency are relatively low and the operation *DC* current is relatively high, the design restrictions on *DC* losses due to thermal heating of the wire are more severe than limitations in core and *PM* due to eddy currents losses. Despite the lower resistivity in comparison to ferrite, the chosen core material is silicon steel, *SiFe* laminations, due to its higher saturation flux density. The use of sintered samarium

cobalt *SmCo* magnet is preferred from other materials with higher flux or higher resistivity due to its higher operating temperature. The length of the *PM* is smaller than the length of the core's airgap. The spaces in between the *PM* and the core, reduces the demagnetizing field in the *PM*. The measured and simulated *LvsI* profiles of this *PMBI* prototype are presented in **Fig.3.3**. Two different simulations are compared with the empirically measured values. It is noticeable the superior accuracy of the *3D FEA* simulation predictions compared with the predictions using *2D FEA*. This implementation design achieved a 50% of the total possible biasing flux of the *SiFe* laminations core and resulted in 30% less core volume.

By using the topology depicted in Fig.3.2.g), the allowable *PM* area is enhanced and the achievable bias in *SiFe* laminations cores is been improved to 75% of the total possible bias, B_{sat} [33]. In this *PMBI* implementation, the total *PM*'s area is composed of a matrix of smaller *PMs*, introducing electrical isolation between the *PM* sections, and reducing the eddy currents on the *PM*. The prototype uses a *UU* core shape, with single layer windings on both core legs. The chosen design strategy utilizes the bias improvement factor, *BIF*, to reduce a 35% the required number of turns, *N* and the required window area, W_a .

3.3.2. Implementations with PMs outside the airgap

Five different publications have been found documenting empirical measurements on physical *PMBI* implementations, using topologies with *PMs* outside the airgaps [17][22][28][36][37]. **Table.3.3**. presents a summary of the *PMBI* characteristics, the chosen design strategies, the biasing flux achieved, the operating conditions and their performance achievements and limitations.

The first publication presenting a practical implementation of a non-standard *PMBI* topology appeared in 2001 [17]. The used topology is depicted in **Fig.3.2.h)**. The implemented inductor operates at a DC current of 18A with an inductance of 10mH. The core material is *SiFe* laminations, and the *PM* is sintered *NdFeB*. The frequency and amplitude of the current ripple are not specified. A *MEC* model is use for the analysis and design of the *PMBI* topology. The iron segments connecting the back of the *PMs* are used to control the amount of biasing flux introduced in the core. There actual biasing level achieved with this topology has not been specified. The empirical measurements on the *PMBI* prototype show a maximum increase of 30% more inductance at the saturation current, while presenting almost the same inductance at lower current level, as compared to a non-biased core. According to the increase in the measured inductance the achieved bias flux in this specific prototype is below 30% of the total allowable bias flux.

In [22] a physical implementation of the topology presented in **Fig.3.2.i)** is empirically evaluated. This *PMBI* topology utilizes a ferrite core with non-standard shape, presenting a secondary magnetic path for the *PMs* biasing flux. The design procedure uses a very sophisticated computer analysis, based on *PBA* coupled with *FEM*,

PERMANENT MAGNET BIASED INDUCTORS

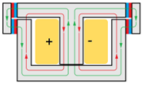
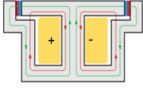
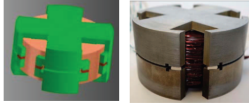
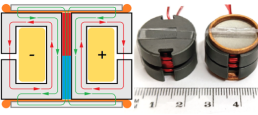
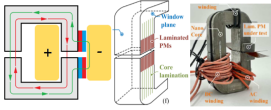
Ref. Nr.	Publication Title PMBI Topology / Implementation	Year	Core material	PM material	Electrical Specifications	Bias % $BIF = \frac{B_{bias} + B_{sat}}{B_{sat}}$	Design Strategy Achievements
[17]	"The principle and design of the permanent magnet bias DC reactor" 	2001	SiFe Laminations	Sintered NdFeB	Frq Not Specified L 10 mH I _{DC} 18 A I _{pp} Not specified	Not Specified $\approx 20\%$ $BIF \approx 1.2$	Compared with the same inductor without PMs. 30% higher inductance at saturation current.
[22]	"Design Paradigm for permanent-magnet-inductor-based power converters" 	2013	Ferrite 3F3	Sintered NdFeB N38SH	Frq 17 kHz L 3 mH I _{DC} 20 A I _{pp} 3 A	Not Specified $\approx 100\%$ $BIF \approx 2$	Compared with equivalent inductance and saturation current. 40% total mass reduction.
[28]	"Magnetically biased inductor for an aerospace switched reluctance drive" 	2015	Somaloy (Hoganas AS)	Sintered NdFeB	Frq 100Hz-1kHz L 20 mH I _{DC} 3.7 A I _{pp} 2.3 A	Not Specified $\approx 10\%$ $BIF \approx 1.1$	Compared with the same inductor without PMs. 10% higher inductance.
[36]	"Permanent Magnet Hybrid Core Inductors for High Saturation Capability" 	2022	Ferrite 3F46	Sintered NdFeB N40SH	Frq 1 MHz L 35 μH I _{DC} 10 A I _{pp} Not specified	45% $BIF = 1.45$	Compared with the same core volume, inductance and saturation current. 27% less number of turns. 50% lower DC resistance.
[37]	"Laminated Permanent Magnets Enable Compact Magnetic Components in Current-Source" 	2022	Finemet F3CC0125	Laminated NdFeB N42	Frq 18 kHz L Not specified I _{DC} Not specified I _{pp} Not specified B _{DC} 0.6 T B _{pp} 0.4 T B _{PM} 0.5 T	30% $BIF = 1.3$	Comparison between relative positions of PMs and laminations. Laminated PMs achieve 90% reduction in eddy current losses compared to standard sintered PMs.

Table 3.3. Summary of *PMBI* implementations using topologies with *PMs* outside the airgaps.

thermal-MEC and electric circuit simulations. Unfortunately, a standard non-biased design is not being provide for performance comparison. The electrical characteristics of the implemented *PMBI* prototype are evaluated as single inductor and operating in a buck converter. The used core material is high frequency ferrite 3F3. The *PM* material is sintered *NdFeB* grade *N38SH*. The complete converter is tested at a switching frequency of 17kHz. The inductor test was done at a frequency of 100Hz. The inductor performance presented higher losses compared to the simulated values and especially higher temperature at the *PMs*. The rise in temperature is probably due

STATE OF THE ART

to the effect of eddy currents, since the electrical resistivity of sintered *NdFeB* is much higher as compared to ferrite *3F3* core material. Nevertheless, this combination of *PMs* and core materials can be employed in applications dominated by a high *DC* current, I_{DC} level and a small *AC* current ripple, I_{pp} . The achieved biasing level of the implemented design is also not indicated. Since the used *PM* material is sintered *NdFeB*, the achieved bias of the ferrite core is expected to be full bias or 100%. The simulation analysis predicted a 40% volume reduction compared to standard non-biased design.

A similar topology presenting the *PMs* near the airgaps on a pot core has been presented in [28]. The core uses a distributed airgap material (*Somaloy*), characterised by a very high saturation flux density, B_{sat} and a relatively low permeability. These magnetic characteristics of *Somaloy* cores, become a challenging target for *PM* biasing techniques. Due to its highest saturation flux density, the required bias flux is also larger compared to other core materials. And due to the low permeability of the material, a substantial percentage of the available *PM's* flux is creating a smaller loop through the airgap, and not reaching the centre pole of the core, required to achieve the desired bias. Nevertheless, the implemented prototype achieves 10% bias and improved with 10% higher inductance, compared with the same core and windings without the *PMs*.

A high frequency ferrite *PMBI* employing the topology depicted in **Fig.3.2.k** is documented in [36]. This topology uses a sintered *NdFeB* *PM* inserted in the centre hole of the ferrite pot core. The *PM's* flux is guided to the edges of the pot core using a top and bottom *Hiperco-50* plates. The prototype is tested with and without the *PM* and achieves a 45% bias flux and 45% increased saturation current. In order to reduce the eddy current losses on the *Hiperco* plates, this prototype employs a copper foil and ring shield, in between the plates and the ferrite core. Unfortunately, the measured quality factor, Q or the *AC equivalent series resistance*, *ESR* of the prototype (with or without the copper shield) are not indicated. This topology is suitable and oriented to applications dominated by *DC* copper losses, with $I_{pp} \ll I_{DC}$. The *PMBI* presents an inductance of 35 μH at a frequency of 1 MHz, with a saturation current of $I_{sat} = 10$ A. The *PMBI* prototype is also compared to a non-biased pot core of the same size and inductance. The *PMBI* employs 27% less number of turns, using thicker wire and achieving 50% smaller *DC* resistance.

The topology depicted in **Fig.3.2.j** is been implemented using nanocrystalline *Finemet UU* cores [37]. The study is focus on the analysis of the improvements achieved by the use of laminated-sintered *NdFeB* *PMs*, as compared to standard sintered *NdFeB* *PMs*. The implemented *PMBI* prototypes achieve 30% bias flux. The use of laminated *PMs* greatly increases the *PM's* resistivity, achieving 90% lower eddy current losses compared with the *PMBI* with conventional sintered *NdFeB* *PMs*.

PERMANENT MAGNET BIASED INDUCTORS

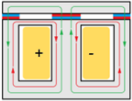
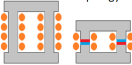
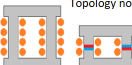
Ref. Nr.	Publication Title PMBI Topology / Implementation	Year	Core material	PM material	Electrical Specifications	Bias % $BIF = \frac{B_{bias} + B_{sat}}{B_{sat}}$	Design Strategy Achievements
[15]	TDK PCH Core "A new reverse-biased choke coil" 	1982	Ferrite TDK H7C1	Barium Ferrite TDK FB3B	Different models Frq max 200 kHz L max 1.5 mH I _{dc} max 36 A I _{pp} max 36 A	30% $BIF = 1.3$	Compared with equivalent core size. 30% higher saturation current. 70% higher Energy Density. 30% more inductance below 10% load current.
[16]	STS "MaxFlux-Magnetically Biased Inductor" 	2014	Ferrite STS proprietary	Not disclosed STS proprietary	Frq 16 kHz L 75 uH I _{dc} 300 A I _{pp} 120 A	100% $BIF = 2$	Compared with equivalent inductance and saturation current. 50% less number of turns. 50% lower DC resistance. 41% less total mass.
[29]	SUMIDA "Magnetically Biased High Power Coil Module" 	2015	MnZn Ferrite F399	Sintered NdFeB N38SH	Frq 72 kHz L 5 uH I _{dc} 55 A I _{pp} Not specified	75% $BIF = 1.75$	Compared with equivalent inductance and saturation current. 42% less number of turns. 42% lower DC resistance. 28% less core volume.

Table 3.4. Summary of *PMBI* commercial products and industry implementations.

3.3.3. Implementations from the industry and PMBI market products

Only three different publications have been found documenting commercially available *PMBI* implementations [15][16][29]. **Table.3.4.** presents a summary of the *PMBI*'s characteristics and design strategies provided by the manufacturers.

In the early 80's, appeared the first *PMBI* commercial product. An engineering analysis of this new *PMBI* topology (**Fig.3.2.e**), develop by *TDK-Electronics*, has also been publish in the scientific literature [15]. This *PMBI* configuration presents no-linear *inductance vs current*, *LvsI* profile, which is desire in some *DC* inductor applications. Due to its saturable magnetic path, the *PCH coil* presents higher inductance for current values smaller than nominal. At low current operation, the *PCH coil* behaves as an un-gapped inductor, presenting its higher inductance. As current increases, the thinnest section of the core becomes saturated and the permanent magnet behaves effectively as an airgap, maintaining its lower nominal inductance value until the current limit at which the biggest sections of the core become saturated. Since the flux path of the coil is directly linking the *PM*, a high resistivity magnet material like barium ferrite has been used, allowing for operation at frequencies up to 200 kHz. The *PCH coil* consist of a series of premagnetized cores available in a range of sizes, allowing for inductances up to 1.5 mH and saturation current up to 36 A. Barium ferrite *PMs* was the best option available at the time of this product

STATE OF THE ART

development. Nevertheless, this *PMBI* product achieved 30% biasing level and 30% increase in the saturation current, compared with non-biased cores of the same size [15].

In 2014, the company *STS*, brought to the market the second *PMBI* commercial product, presenting reduced size as compared to a standard inductor with the same power rating [16]. This product is marketed as *MaxFlux-InDur*. This *PMBI* design combines the benefits of an optimised thermal dissipation (*InDur*) and *PM* biasing (*MaxFlux*). It is implemented using a topology having *UU* cores with single layer coils. The core segments containing the coils present a circular area cross-section, to minimize the coil's perimeter per unit area. These *PMBIs* are potted and encapsulate in aluminium, in order to maximize thermal dissipation. The *PM* biased *InDur* design achieves approximately 30% smaller size and equivalent losses, compared with the non-biased *InDur* design. The chosen design strategy consisted on reducing the number of turns and utilizing a smaller core with the same area cross-section and reduced magnetic length, as represented in **Fig.3.1.b**). On the other hand, the specific biasing arrangement of the cores and *PMs* in this topology has not been disclosed by the authors of the publication.

The latest *PMBI* commercial implementation has been documented by *SUMIDA Electronics* [29]. This *PMBI* is also implemented on *UU* cores with single layer coils, and with the same design strategy (**Fig.3.1.b**). The core uses a newly developed ferrite material with optimized grain characteristics improving thermal stability and high saturation flux density at high temperature operation. The specific *PM* position within the core is not specified by the authors. The cores are probably biased by several *PMs* inside several gaps along the core's length. Other possibility could be the use of hard magnetic material, bonding the distributed micro-airgaps between grains of soft magnetic ferrite material. This *PMBI* implementation achieves 75% biasing, resulting in 42% less copper weight, and 28% less core volume.

3.4. CONCLUSIONS ON THE STATE OF THE ART

After the analysis of the state of the art, the following conclusions can be acknowledged:

- *PMBIs* present desirable improvements in the design achievements compared to non-biased inductors. 100% bias flux allows for an improvement factor, $BFI = \times 2$ on the product of the design parameters: $L * I_{sat} * 1/N * 1/A_c$.
- *PMBI* topologies using ferrite cores and bonded *NdFeB* *PMs* has been documented to achieved up to 60% biasing flux, without introducing additional *AC* losses and or excessive demagnetizing *mmf* fields at the *PMs* surface [18].

PERMANENT MAGNET BIASED INDUCTORS

- Ferrite cores biased with sintered *NdFeB* *PMs* can easily achieve 100% linear bias flux, while maintaining the *mmf* fields at the *PMs*, below its demagnetization threshold, H_k . Sintered *NdFeB* presents a relatively low resistivity compared with the ferrite core material. *PMBIs* with this combination of core and *PM* materials are limited by *AC* losses due to eddy currents on the *PMs*. Nevertheless, applications requiring a high *DC* current, I_{DC} and a relatively small *AC* ripple, $I_{pp} \ll I_{DC}$, are dominated by *DC* losses, and can benefit using sintered *NdFeB* *PMs* [22][31][32][36].
- *SiFe* lamination cores have a higher saturation flux density, B_{sat} and therefore present a higher challenge for the biasing technique. The highest bias flux achieved in *SiFe* laminations is 75%, using sintered *NdFeB* *PMs* and the topology depicted in **Fig.3.2.g**) [33].
- Topologies using *PMs* outside the airgaps, greatly reduced the demagnetization fields on the *PMs*.
- The maximum achievable bias flux is proportional to the *PM's* area. Topologies allowing for the highest *PM's* area are desired.
- Topologies employing standard core shapes are desired, due to simple replicability and minimal production cost.

It is desired to investigate the development of possible new *PMBI* topologies and improvements which can guarantee achievement of 100% bias flux, on both standard ferrite and *SiFe* lamination cores, without introducing excessive losses or impacting the lifetime of the *PM*.

4. PRACTICAL INVESTIGATION AND PROTOTYPE IMPLEMENTATIONS

In order to find solutions and improvements for the previously mentioned challenges and goals of state-of-the-art *PMBIs* topologies, a practical analysis of the possible interactions of *PMs* and standard non-gapped cores was initiated. A series of practical experiments resulted in the identification and development of a new *PMBI* topology with improved characteristics.

4.1. PRACTICAL INVESTIGATION

The first experiment consisted of placing a sintered *NdFeB PM*, besides a non-gapped ferrite toroid inductor. This approach produced an interesting behaviour on the magnetic flux within the toroid. **Fig.4.1.a)** shows magnetic flux vector diagram of the toroid core and the *PM* in this experiment. The magnetic flux induced by the coil's *DC* current is represented by the red vectors. The magnetic flux induced by the *PM* is represented by the green vectors. In a shorter section of the toroid core, the magnetic flux induced by the *PM* is presenting the same direction as the magnetic flux induced by the *DC* current in the coil. This segment of the core has been saturated at some extent, presenting an effective permeability within the expectable range of a distributed airgap material. In the following, this section of the core is being refer as the “*saturation-gap segment*” or *SG-segment*. In the longer portion of the core, the *PM* is introducing the desired bias flux, in opposite direction to the flux induced by the coil's current, successfully extending the saturation current of the inductor. In the following, this longer section of the core is being refer as the “*biased segment*”. This first experiment successfully achieved 100% biasing of a standard non-gapped toroid

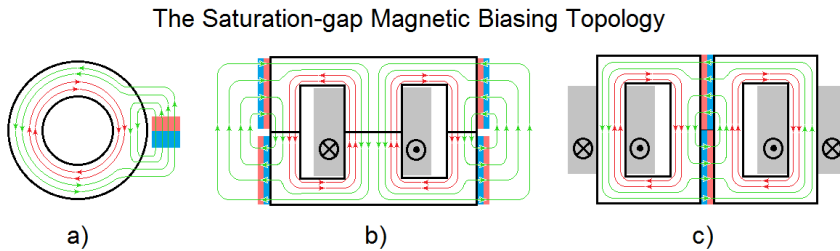


Fig.4.1. Evolution of the development of the *Saturation-gap* magnetic biasing topology. Red vectors represent magnetic flux induced by the *DC* current in the coils. Green vectors represent magnetic flux induced by the *PMs*. *a)* Toroid core. *b)* *EE* core. *c)* *2xUU* cores.

core, while simultaneously producing the equivalent effect of a typical airgap. On the other hand, the *PM* connection to the core was not optimal and a better design needed to be developed. The *saturation-gap reluctance* in the toroid, presented a value in the range expected from a typical airgap. Using longer or stronger *PMs* or adjusting the distance between the *PM* to the core, resulted in the modification of the reluctance of the saturation-gap, allowing for the adjustment of bias flux and inductance value. On the other hand, the specific procedure for the calculation of the equivalent airgap reluctance of the saturation-gap and the desired bias flux were still unknown.

A similar experiment was performed using an *EE* ferrite core, as depicted in **Fig.4.1.b**). Using this *EE* core, the reluctance of the saturation-gap was easily compared to an equivalent airgap. Several *PMs* were stacked in series and/or in parallel, increasing their total effective *PM's* length and area respectively. The *inductance vs current, LvsI* profiles of the *EE* inductor with different *PM's* lengths and areas were empirically measured. The experiment showed that the reluctance of the *saturation-gap* is adjustable and proportional to the reluctance of the *PM*, and therefore proportional to the *PM's* length. This technique can be used for the adjustment of the *saturation-gap* reluctance and define the required inductance with this *PMBI* topology. On the other hand, this topology presented important limitations. Similar to the topology depicted in **Fig.3.2.j**), a portion of the magnetic circuit of the biasing flux is flowing in the air between the two *PMs*. This increases the load reluctance, \mathcal{R}_l at the *PMs* and therefore reduces their operation point and the achievable bias flux, as shown in (2.48). In order to avoid the external magnetic flux, and optimise the achievable *PM's* flux, by raising its operation point, the configuration presented in **Fig.4.1.c**) was developed. This configuration consists of two non-gapped *UI* (or *UU*) cores, simultaneously biased by the same pair of *PMs*. The two biased inductors present no magnetic flux linkage between them. The optimization of the *PM's* operation point allows for the use of *PM* materials with lower remanence, which typically offers higher electric resistivity and therefore lower losses. The two inductor coils can be connected in series or parallel, to behave as a single inductor with increased inductance or saturation current respectively.

The further investigation and understanding of the saturation-gap biasing topology and the techniques required for design, has been evolving during the implementation and empirical testing of several physical *PMBI* prototypes. The analysis, simulation, and design procedure for this new *PMBI* topology are summarized on **Chapter 5**. The different practical implementations and empirical test measurements are presented in the following.

PRACTICAL INVESTIGATION AND PROTOTYPE IMPLEMENTATIONS

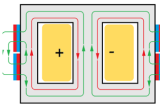
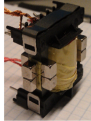
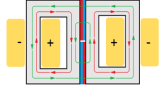

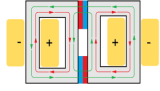

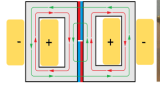

Ref. Nr.	Publication Title PMBI Topology / Implementation	Year	Core material	PM material	Electrical Specifications	Bias % $BIF = \frac{B_{bias} + B_{sat}}{B_{sat}}$	Design Strategy Achievements
[24] [P1]	"Method for introducing bias magnetization in ungapped cores, The Saturation-gap"	2014	MnZn Ferrite N87	Sintered NdFeB N42	Frq 8 kHz L 340 μ H I _{dc} max 5 A I _{pp} max 10 A	Prototype PM1. Two pairs PMs per leg	
						100%	100% higher saturation current. Identical DC resistance.
						$BIF = 2$	
			B _{sat} 0.49 T ρ > 1 k Ω -cm μ r 2200	Br 1.2 T ρ 150 μ Ω -cm μ r 1.1		Prototype PM12. Three pairs PMs per leg	
						>100%	Over linear bias. 200% higher saturation current.
						$BIF = 3$	Identical DC resistance.
[25] [P2]	"Size Reduction of a DC link Choke Using Saturation-gap and Biasing with Permanent Magnets"	2014	SiFe Laminations	Sintered NdFeB N42	Frq 300 Hz L 1 mH I _{dc} 20 A I _{pp} 15 A	100%	Two UI PMBIs in series compared to one standard EE with equivalent inductance and saturation current.
			B _{sat} 1.5 T ρ < 5 m Ω -cm μ r 4000	Br 1.2 T ρ 150 μ Ω -cm μ r 1.1		$BIF = 2$	50% smaller core volume. 30% higher DC resistance. 37% total volume reduction.
[27] [P4]	"Half Size Reduction of DC Output Filter Inductors with the Saturation-gap Magnetic Bias Topology"	2016	MnZn Ferrite MF198A	Bonded NdFeB	Frq 30 kHz L 5 mH I _{dc} 9 A I _{pp} 2 A	100%	Compared with equivalent inductance and saturation current.
			B _{sat} 0.47 T ρ > 500 Ω -cm μ r 5500	Br 0.8 T ρ > 10 k Ω -cm μ r 1.5		$BIF = 2$	50% smaller core area cross-section. 50% less core volume. 16% lower DC resistance
[27] [P4]	"Half Size Reduction of DC Output Filter Inductors with the Saturation-gap Magnetic Bias Topology"	2016	MnZn Ferrite F1399	Bonded NdFeB	Frq 30 kHz L 5 mH I _{dc} 9 A I _{pp} 2 A	>100%	Compared with equivalent inductance and saturation current. Over linear bias.
			B _{sat} 0.47 T ρ > 500 Ω -cm μ r 5500	Br 0.8 T ρ > 10 k Ω -cm μ r 1.5		$BIF = 3$	35% less number of turns. 50% lower DC resistance. 50% smaller core area cross-section. 50% less core volume. 50% total volume.

Table 4.1. Summary of PMBI implementations using the Saturation-gap topology.

4.2. PMBI PROTOTYPE IMPLEMENTATIONS

This sub-chapter summarizes the different practical *PMBI* implementations developed during the present study. Their characteristics and electric properties are empirically tested and compared to standard non-biased prototypes. These implementations have also been documented in one journal and three conference publications attached on the appendixes (P1, P2, P3 and P4). **Table. 4.1.** presents the summary of the achievements and design strategies of *PMBI* implementations using the Saturation-gap topology.

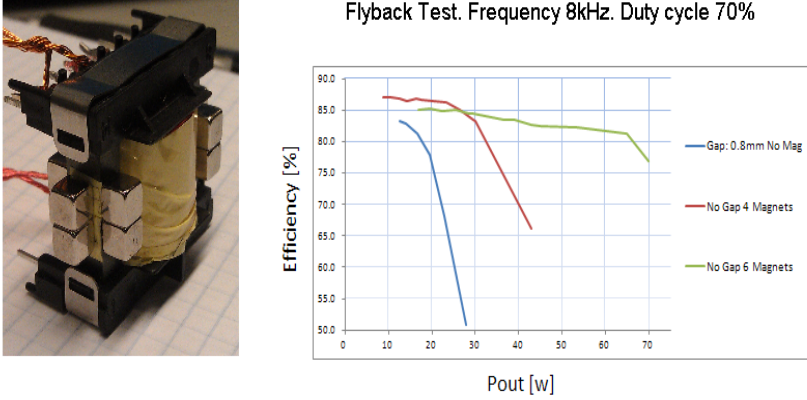


Fig.4.2. Flyback transformer test. *Left:* Ferrite *EE30* transformer, biased with 3 pair of *PMs* in each leg. *Right:* Converter efficiency as function of power output. Blue curve is non-biased *EE30* core with *0.8mm* total airgap length. Red curve is biased with 2 pair of *PMs* in each leg, achieving full linear biasing. Green curve is biased with 3 pair of *PMs* in each leg, achieving an over-saturated biasing state. *Figure and data from [24].*

4.2.1. Ferrite flyback transformer

The first *PMBI* prototypes utilizing the *Saturation-gap* biasing technique, were implemented on an *EE30* ferrite core transformer, using the biasing topology depicted in **Fig.4.1.b**). Two different *PMBIs* were tested and compared with a standard non-biased prototype. The different implementations operating as a *flyback transformer* has been documented in conference publication P1. This topology in **Fig.4.1.b**) and **Fig.4.2.left**, was far from optimal and presented some drawbacks; on the other hand, it provided a good proof of concept of the biasing technique with saturation-gap and understanding of the *over-saturated* biasing possibilities. More than $>100\%$ bias (*over-saturated bias*) is achieved when the totality of the linear region of the *BH-loop* and an additional portion of the saturated region of the core is being shifted to the initial operation point at zero current. *Over-saturated* bias level can achieve a biasing improvement factor higher than two, ***BIF*** $>x2$.

One standard gapped *EE30* core transformer and two *PMBIs* prototypes were implemented and tested. The *PMBI* designs used the same *EE30* core and windings. The side legs of the *EE* cores present a square cross-section, having 3 of the surfaces suitable for placing the *PMs*. The two biased prototypes used 2 and 3 pairs of *PMs* in each leg. These *PMBI* prototypes achieved *full linear biasing* (100% bias flux) and *over-saturated biasing* states (more than 100% bias flux), respectively. The physically

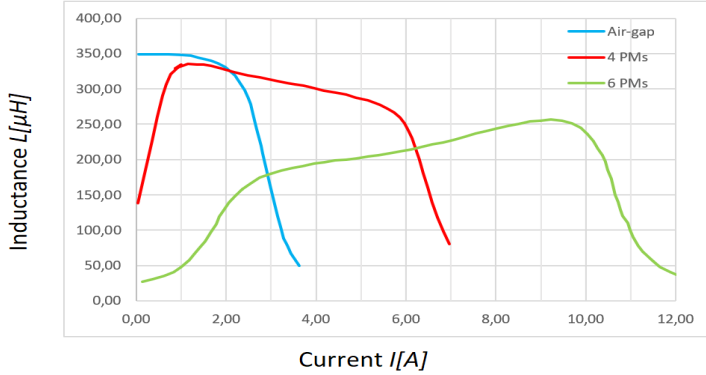


Fig.4.3. Inductance as function of Current, $LvsI$ measured on three prototypes: Standard non-biased ferrite *EE30* core with 0.4 mm airgap in each leg (blue curve). Saturation-gap *PMBI* with the same *EE30* core and windings and 2 pairs of *PMs* in each leg (red curve). Saturation-gap *PMBI* with the same *EE30* core and 3 pairs of *PMs* in each leg. Measured at 10 kHz frequency at the primary windings, using Wayne Kerr 3260B Magnetic Analyzer. Data from [24].

build prototype, with 3 pairs of *PMs* on each leg, is presented in Fig.4.2.(left). Fig.4.3. shows the measured $LvsI$ profiles of the three prototypes. It can be noticed that the saturation current has been increased by a factor of $\times 2$ (100% bias) and $\times 3$ (>100%), respectively. It is also noticed that the biasing introduced by the *PMs* is also presenting a reduced inductance value. The prototypes used ferrite core material and sintered *NdFeB* *PMs*. The higher flux density of the *PMs* compared with the saturation flux density of ferrite, produces a partial saturation of the core resulting in a higher reluctance value, like the effects reported with topologies with *PMs* near the airgaps [35]. The relatively low resistivity of sintered *NdFeB*, compared to the ferrite core, presented additional losses due to eddy currents proportional to the frequency of operation. The three transformers were tested on a flyback converter. The converter was operated at critical conduction mode ($I_{pp} = 2 I_{DC}$) at 8 kHz switching frequency. Operation of the converter at higher frequencies and at critical conduction mode ($I_{pp} = 2 I_{DC}$), resulted in excessive eddy current losses due to the low resistivity *PMs*. On the other hand, sintered *PMs* can safely be used in applications characterised by relatively high DC current and small AC ripple, $I_{pp} \ll I_{DC}$ [22][31][32][36]. The input voltage was initially set at 13V and was increase in steps until saturation was reach. The output load was adjusted in order to get an output voltage equal to four times the input value. The input and output power, at the different input voltage levels, was empirically measured. Fig.4.2.(right) shows the three converter efficiencies as a function of the output power. It can be appreciated, that the output power has been

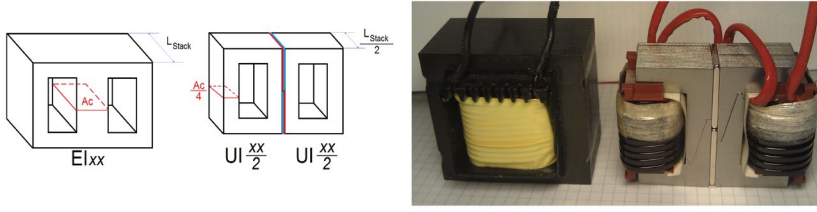


Fig.4.4. *Left: Core representation of the half-size core reduction strategy with Saturation-gap biasing topology. Right: Physical prototypes. Figure from [25].*

increase more than three times, while maintaining the efficiency, when using the PMBI with *over-saturated* prototype.

4.2.2. Steel laminations DC link choke

The second implementation used the optimised *Saturation-gap* topology using two *UI* cores biased by a pair of PMs, depicted in **Fig.4.1.c)**. The goal of the experiment was to validate the possibility of achieving *full-linear biasing* on *SiFe* laminations core material with the proposed topology. The target of the PMBI design was reducing the size of the *DC* link choke for an electric motor drive application. The two *UI* biased inductors connected in series were used to achieve the same inductance and current rating of the non-biased reference design, using standard gapped *EI* *SiFe* laminations. The inductor was required to provide $1mH$ at a rated current of $20A$ with a current ripple frequency of $300Hz$. *Full linear biasing* was achieved using sintered *NdFeB N42* magnets. *Full linear (100%) biasing* allows for a 50% reduction in the required *LI* product, allowing 50% smaller core area cross-section, A_c or number of turns, N . Since the design target was focus on achieving minimal size and weight, 50% reduction of the area cross-section, A_c was implemented following the strategy depicted in **Fig.4.4.(left)**. Since the PMBI is comprised of two *UI* inductors connected in series, each *UI* inductor is required to provide half of the rated inductance, and each area cross-section can be reduced by a factor of 4. By using the equivalent size of *UI* to *EI*, and reducing the stack height by half, a 50% core reduction has been achieved while maintaining the same window area for the same number of turns in each *UI*. The sum of the perimeters of the two *UI* cores area cross-section is equal to the perimeter of the reference *EI* cross-section. On the other hand, the multiple layers windings present a higher mean length per turn, *MLT* and the biased design with the two coils in series presented 30% higher copper *DC* resistance. Nevertheless, the design target was focus on achieving maximal core size reduction, and the implemented PMBI prototype presented 50% smaller core volume. The PMBI and the reference non-biased *EI* inductor are presented in **Fig.4.4.(right)**. The

PRACTICAL INVESTIGATION AND PROTOTYPE IMPLEMENTATIONS

	Total Power Losses [W]	Copper Losses [W]	Core Losses [W]	Operating Conditions
Standard	17.2	13.8	3.4	$I = 20 \text{ A (DC)} + 7.5 \text{ A}_p \text{ (AC)}$ $Frq = 300 \text{ Hz}$
PMBI	22	18.5	3.5	

Table 4.2. Power Losses of the Standard and the PMBI prototypes operating at nominal power. Operating conditions: 20 A DC current with a 7.5 A (peak) AC ripple at 300 Hz , using a *Spitzenberger Grid Simulator EMV D 45000/PAS*. Data from [25].

characteristics of both inductors were empirically measured using a *Magnetic Analyser WK3260B*. **Fig.4.5.** present the inductance, L and AC Equivalent Series Resistance, ESR as a function of DC current measured on the reference and the biased inductors. It can be appreciated, that the *Saturation-gap PMBI* prototype can closely match the $LvsI$ profile of the reference standard design, while presenting 50% core size reduction. The ESR value is representative of the addition of copper losses and iron core losses. The contribution of the iron losses and the winding's DC resistance, to the ESR , is expected to be constant over the current range. On the other hand, the ESR of the PMBI in **Fig.4.5.(right)**, is higher at low current levels and gradually decreases very close to the value of the standard prototype. This characteristic is due to the contribution of the losses in the PMs to the total ESR . The eddy current induced in the PMs, are proportional to the magnetic flux variations ($d\phi/dt$) through the PMs. The prototypes were also test at nominal power, operating at a 20A DC bias current with a 7.5A (peak) sinusoidal current ripple, using a *Spitzenberger Grid Simulator EMVD 45000/PAS*. **Table 4.2.** Presents the measured total losses and the contribution of copper losses and core losses of both prototypes, operating at nominal power. The PMBI presents 28% higher losses, mostly dominated by the copper losses. This

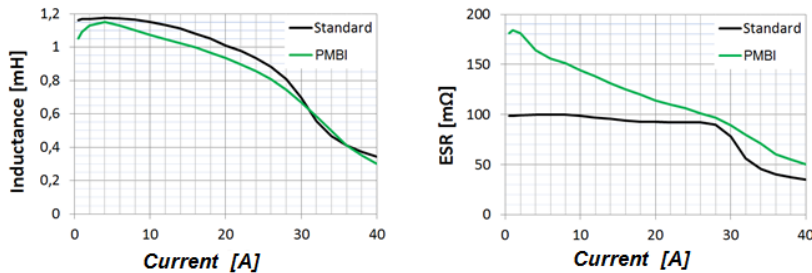


Fig.4.5. Inductance versus current, $LvsI$ (left) and Equivalent Series Resistance, ESR versus DC bias current (right). Measured with *WK3260B* magnetic analyzer. Stimulus: $300\text{mV rms AC } 300\text{Hz}$. Figure from [25].

PERMANENT MAGNET BIASED INDUCTORS

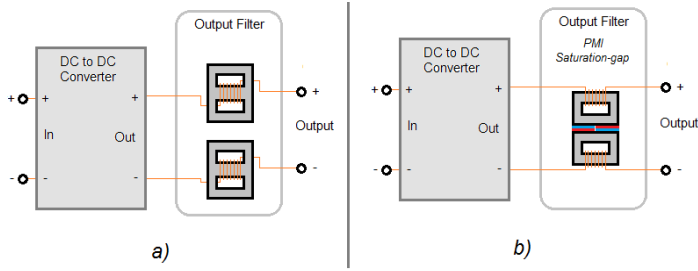


Fig.4.6. Block Diagram of symmetric output filter inductors. **a)** Standard non-biased filter inductor pair. **b)** Symmetric output filter with the *Saturation-gap* topology, using two non-coupled *UU* inductors simultaneously biased by a pair of permanent magnets (*PMs*). *Figure from [27].*

situation is a direct consequence of the design target, focused on reducing the total core volume by 50%. A compromise between possible the core's area reduction and the number of turns reduction, could yield more optimal results, if achieving minimal core size is not the priority. The *PMBI* consist of two biased inductors connected in series, thus increasing noticeably the total wire resistance, R_{DC} . Applications where two standard inductors are connected in series, would present a better condition for minimizing the total wire resistance of *PMBIs*, with the *Saturation-gap* topology.

4.2.3. Ferrite filter inductor pair

The last *PMBI* implementation consisted of a symmetric filter inductor pair, for a buck converter. The complete filter, including two symmetric inductors effectively connected in series, is required to provide an inductance of $5mH$ in the current range from $8A$ to $10A$. The converter operates at a frequency of $30kHz$. The reference design

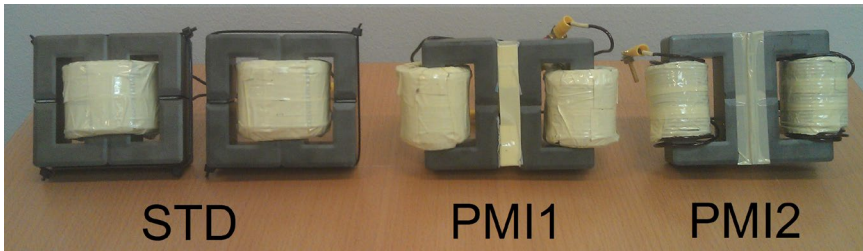


Fig.4.7. Physically implemented filters. From left to right: Standard inductor pair (STD), Linear biased inductor pair (PMI1), Over-Saturated inductor pair (PMI2). *Figure from [27]*

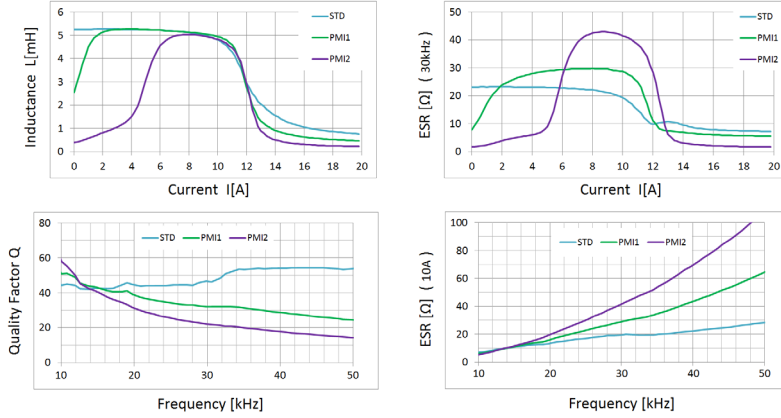


Fig.4.8. Measurement results of the standard (STD) and biased inductor prototypes (PMI1 and PMI2). *Top:* Inductance and equivalent series resistance, ESR as function of current. Stimuli: 500mV AC 300 kHz. *Bottom:* Quality Factor (Q) and ESR as function of frequency; Stimuli: 500mV AC 10A DC. Figure from [27].

uses two standard gapped EE ferrite inductors as depicted in **Fig.4.6.a**). This two inductors filter, has also been implement using the *Saturation-gap* topology, as depicted in **Fig.4.6.b**). The two UI ferrite cores were simultaneously biased, by one pair of *bonded-NdFeB* PMs. The higher electrical resistivity of *bonded-NdFeB* compared to the more common *sintered-NdFeB* allows for lower eddy current losses on the PMs, and higher frequency of operation. The use of two separated inductors, inherent to the *Saturation-gap* topology optimizes the biasing benefits for applications requiring a symmetric pair of inductors. The two PMBI prototypes PMI1 and PMI2 were design in order to achieve *full linear biasing* and *over-saturated biasing*, respectively. **Fig.4.7.** presents the standard filter (STD) and the two different *Saturation-gap* filters (PMI1 and PMI2).

- The biased filter pair operating in *full linear biasing*, (100% bias flux) PMI1 achieved 50% core volume, 25% lower copper volume and 13% lower DC resistance, R_{DC} as compared to the STD filter pair.
- The biased filter pair operating in *over-saturated biasing*, (more than 100% bias flux) PMI2 achieves 50% core volume and a reduction of 35% less number of turns, resulting in 50% copper volume, 50% DC resistance, R_{DC} and a total 50% volume reduction.

The inductance, L and ESR values of three the filters, as function of DC current and stimuli frequency was measured empirically. **Fig.4.8.** presents the measurement

PERMANENT MAGNET BIASED INDUCTORS

results of the three filters. It can be notice that the biased designs, clearly achieve the required inductance within the required current range while having a reduced core and copper volume. At the operation frequency of $30kHz$, the filter in *full linear biasing*, *PMI1* presents a *ESR* value 50% higher than the non-biased filter, *STD*. The *ESR* value of *PMI2* is double of the non-biased filter, *STD*. The filters were also tested on a buck converter operating at $30kHz$ switching frequency. The three filters presented equivalent voltage and current waveforms, efficiency, and operating temperatures. The simulation, analysis, and design procedure of this *PMBI* topology, referred as the *Saturation-gap* topology, is presented in the following chapter.

5. DESIGN ANALYSIS AND SIMULATION OF THE SATURATION- GAP TOPOLOGY

5.1. INTRODUCTION

The *Saturation-gap* topology presented in **Fig.4.1.c)**, has been analysed by *MEC* modelling and *2D magneto-static FEA* simulations. The *FEA* simulations provided a relatively good approximation of the inductors *LvsI* profiles and provide a good tool for the understanding of the flux behaviour in a *Saturation-gap* topology. On the other hand, a higher accuracy could be achieved using *3D FEA* simulations and is proposed as subject for future work. A simple design procedure based on a simplified *MEC* analysis has also been presented.

5.2. FEA SIMULATIONS

In order to further understand the behavior of the magnetic flux in the *PMBI* topology proposed in **Fig.4.1.c)**, a simulation using *2D* finite element analysis, *FEA* with

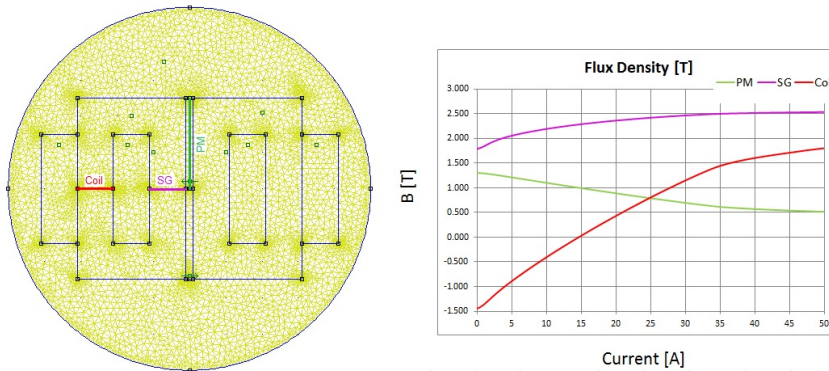


Fig.5.1. Flux density distribution in a *Saturation-gap* topology. *Left: FEMM* model; Core: UI30; PM's length= 3mm NdFeB N42. *Right: Flux density* measured at the colored lines on the *FEA* model: Coil (red), SG (purple) and PM (green), as function of current in the coils. *Figure from [26][P3].*

PERMANENT MAGNET BIASED INDUCTORS

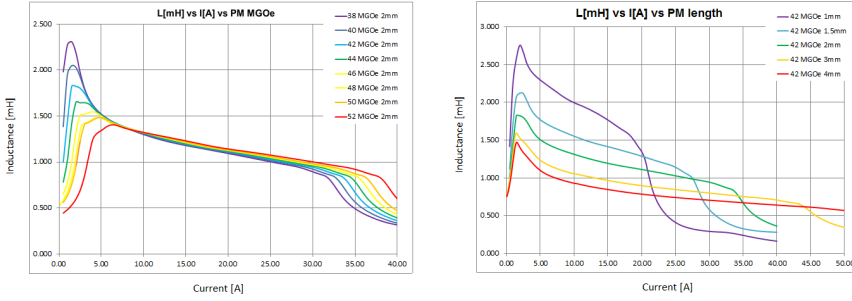


Fig.5.2. Simulated $LvsI$ profiles, for different PM lengths (*right*); and different PM's grades of maximum energy product (*left*). Simulated with 2D FEA. Figure from [26][P3].

software *FEMM* has been performed. The core material used for the *FEA* model is laminated steel, with a saturation flux density, B_{Sat} of $1.5T$. The magnetic core consists of EI30 *SiFe* laminations, with a stack height of 20 mm . Each bobbin contains 36 turns of 2.2 mm copper wire. Different grades and sizes of sintered *NdFeB* PMs have been simulated. The analysis is repeated for current range between $0A$ and $50A$ in steps of $0.5A$. **Fig.5.1.** shows the *FEMM* model and the magnetic flux density as function of current provided by the simulation. The flux density is measured at three different points in the magnetic circuit. At the biased segment inside the coil (red line), the initial flux density, with no current, is equal to $-1.5T$, which is equivalent to 100% of the linear region been biased. In the current range from 0 to $35A$, the flux density value goes from $-1.5T$ to $1.5T$. This range of $3T$ comprises the total linear region of the core, from the negative saturation limit ($-1.5T$) at the 3rd quadrant, to the positive saturation limit ($1.5T$) at the 1st quadrant. In the saturation-gap segment of the core (purple line), the flux density is above the linear range of the core. It is noticeable that while in the same current range, the increment of flux in this segment is only $0.5T$. This equilibrium of the flux present in the *saturation-gap* segment, *SG-segment* is maintained by the action of the PMs. Increments of magnetic flux induced by current in the coil, are compensated by decrements in the flux sourced by the PM, lowering its operation point, and maintaining an almost constant flux density at the *SG-segment*. By lowering the PM's operation point, energy has been stored in the PM, as represented in **Fig.2.8**. The flux density at the *SG-segment* increases to what can be refer as the *Quasi-Saturated Equilibrium*, *QSE*, where the reluctance of the *SG-segment* is equivalent to the PM's reluctance, achieving a condition for presenting maximum energy product of the PMs. In the present example, the *QSE* value is $2.5T$. This provides an almost constant reluctance at the *SG-segment*, presenting a constant nominal inductance value while the longer segment of the core is operating within its linear range. The *QSE* value is dependent on the PM reluctance, and therefore its geometry. **Fig.5.2.** shows the $LvsI$ profiles, calculated from the simulation results

with different *PM* lengths and grades. It is noticeable that the nominal inductance, and therefore the *QSE* value and the reluctance of the *SG-segment*, are dependent on the *PM* length. On the other hand, the nominal inductance is independent of the *PM*'s maximum energy product. The magnet grade is responsible of the total biasing flux introduced in the core. The *PMs* with higher energy products introduce higher flux levels and displace the linear region of the *LvsI* profile to higher current ranges. The *PMs* with lower energy products present a non-linear *LvsI* profile having higher inductance values at very low currents, similar to the profile of *non-constant-length airgaps* or the *PMBI* depicted in **Fig.2.6.(right)**. This *LvsI* profile is desired in some converter applications [15]. The *2D FEA* simulations provided a good tool for the understanding of magnetic flux behaviour in the proposed topology. On the other hand, the simulated *LvsI* profiles present significant differences compared to the empirical measured profiles. The simulation analysis is based on a *magneto-static* problem solver and the effect of eddy currents is not considered. Since the modelling of the inductor is restricted to a *2D* plane (*x* and *y-axis*) the presence of leakage flux in the *z-axis* is not considered and therefore, these simulations do not provide sufficient accuracy to be used as a precise design tool. Small adjustments on the final design are commonly required. The use of more sophisticated *FEA* software, including *3D* modelling and simulation of eddy current effects could increase the simulations accuracy to a level suitable for design purposes. In order to calculate the different design parameters, like the required *PM*'s grade and length, without requiring complex computer simulations, a simple approximation suitable for design calculations has been presented in the following subchapter.

5.3. SIMPLIFIED MEC ANALYSIS

The *magnetic equivalent circuit*, *MEC* presented in **Fig.5.3**. provides a simplified model of the saturation-gap topology. The biased portions on each magnetic core, are represented by the *bias reluctance*, \mathcal{R}_{bias} and the *saturation-gap* section of each core is represented by the *saturation-gap reluctance*, \mathcal{R}_{sg} . The *magnetic permeability*, μ_r of the core material is dependent on its operation point on the *BH-loop*, therefore the core reluctances are depicted as non-linear resistors. The *QSE* is the flux density, $B_{\mathcal{R}_{PM}}$ required for the core to present the same reluctance as the *PM*, \mathcal{R}_{PM} . The *PMs* are simulated by a current source model as depicted in **Fig.2.8**. The *PMs* reluctance, \mathcal{R}_{PM} can be calculated as:

$$\mathcal{R}_{PM} = \frac{l_{PM}}{\mu_0 \mu_r A_{PM}} \quad (5.1)$$

The approximation taken in (2.52) can also be employed to accommodate for fringing flux at the edges of the *PM*. The *short-circuit*, or *remanent flux*, ϕ_r of the *PM* can be calculated by:

PERMANENT MAGNET BIASED INDUCTORS

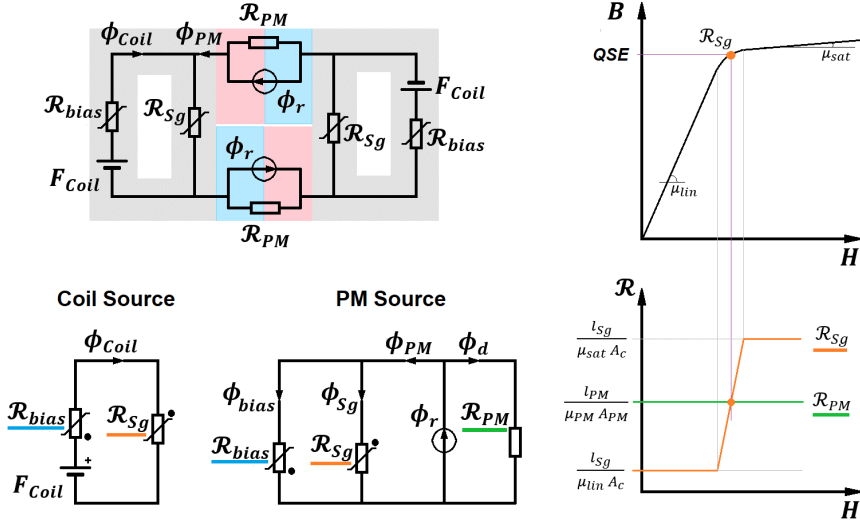


Fig.5.3. MEC model of the Saturation-gap topology (top-left) and Simplified MEC models of the Coil-source circuit and PM-source circuit (bottom-left). $B(H)$ and $R(H)$ profiles of the segment (right).

$$\phi_r = A_{PM} B_r \quad (5.2)$$

The total PM's flux, ϕ_{PM} , through the core's reluctances (\mathcal{R}_{bias} and \mathcal{R}_{Sg}) can be calculated by:

$$\phi_{PM} = A_c (B_{bias} + B_{Sg}) = \phi_r - \phi_d \quad (5.3)$$

The self-demagnetization flux, ϕ_d represents flux not available at the load, flowing through the PM's reluctance \mathcal{R}_{PM} . The total flux, ϕ_{PM} provided by the PM can be calculated using:

$$\mathcal{R}_l = \frac{\mathcal{R}_{bias} \mathcal{R}_{Sg}}{\mathcal{R}_{bias} + \mathcal{R}_{Sg}} \quad (5.4)$$

From the PM's current source model as reference, the reluctances \mathcal{R}_{bias} and \mathcal{R}_{Sg} are in parallel configuration. From the voltage source model of the coil as reference, the core reluctances \mathcal{R}_{bias} and \mathcal{R}_{Sg} present themselves in series configuration. While the value of \mathcal{R}_{bias} is within the linear region, the total reluctance is mostly dominated

Levels of Magnetic Biasing with the Saturation-gap Topology

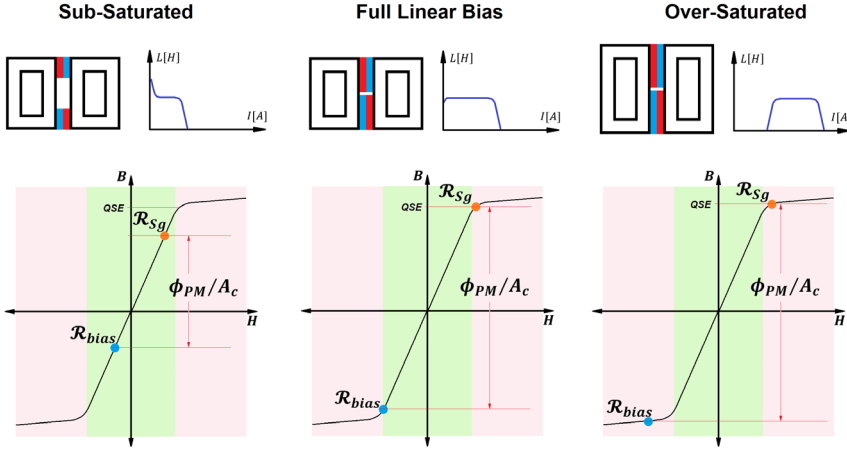


Fig.5.4. Biasing Levels as function of PMs flux over core area cross-section (ϕ_{PM}/A_c). Three operation modes and associated $LvsI$ profiles. Green areas delimit the linear region of the BH curves of the core material; Red areas delimit the non-linear region. Orange and blue markers represent the initial ($I = 0A$) operation point of \mathcal{R}_{Sg} and \mathcal{R}_{bias} respectively. *QSE* is the *Quasi Saturated Equilibrium* flux density.

by \mathcal{R}_{Sg} . Therefore, the operation point of the PM is mostly dependent on the *saturation-gap reluctance*, \mathcal{R}_{Sg} , which is a non-linear function of the instantaneous flux density, B_{Sg} flowing through the *saturation-gap* segment, $\mathcal{R}_{Sg} = \mathcal{R}_{Sg}(B_{Sg})$. As current increases, the total magnetic flux introduced by the coil, ϕ_{coil} increases and the operation point of the PMs and the associated $PM's$ flux ϕ_{PM} is lowered. This linear source behavior of the PMs , results in an almost constant flux density, B_{Sg} at the *saturation-gap* segment resulting in almost constant reluctance, \mathcal{R}_{Sg} , presenting a linear inductance profile like a gapped core. In the *MEC* model presented in **Fig.5.3.**, the current source ϕ_r is in parallel with both: \mathcal{R}_{Sg} and \mathcal{R}_{PM} . The $PM's$ reluctance, \mathcal{R}_{PM} defines the limit of the maximum achievable $PM's$ flux, ϕ_{PM} and the associated maximum reluctance of the *saturation-gap* segment, $\mathcal{R}_{Sg}(B_{Sg})$. The *quasi-saturated equilibrium*, *QSE* has been defined as the flux density level at which the reluctance of the core, \mathcal{R}_{Sg} is equivalent to the reluctance of the PM , $\mathcal{R}_{Sg}(B_{Sg} = QSE) = \mathcal{R}_{PM}$. Therefore, the linear nominal inductance of can be approximated by:

$$L_N = \frac{N^2}{\mathcal{R}_{Sg}} \cong \frac{N^2}{\mathcal{R}_{PM}} \quad (5.5)$$

PERMANENT MAGNET BIASED INDUCTORS

As seen in **Fig.5.4**, different $LvsI$ profiles can be achieved by introducing different biasing flux density levels. The initial flux density at zero current, $B_{sg}(I = 0)$ and $B_{bias}(I = 0)$ determines the operation mode of the *PMBI* design. The total flux introduced by the *PMs* can be calculated by:

$$B_{sg} + B_{bias} = \frac{\phi_{PM}}{A_c} \quad (5.6)$$

The inductance as function of current, $LvsI$ characteristic of each operation mode are represented in **Fig.5.4.(right)**. The blue and orange markers are indicative of the operation point of the core's reluctances, \mathcal{R}_{bias} and \mathcal{R}_{sg} , at initial flux conditions, $B_{sg}(I = 0)$ and $B_{bias}(I = 0)$. There are three possible operation modes depending on the initial conditions:

Sub-Saturated or Under-biased

- Flux density at \mathcal{R}_{sg} is below the *QSE* value. $B_{sg}(I = 0) < QSE$.
- Flux density at \mathcal{R}_{bias} is in the linear region of the 3rd quadrant. $B_{sg}(I = 0) > -B_{sat}$

The inductance as function of current, $LvsI$ characteristic of the *under-biased* operation mode, presents a higher value of inductance for lower currents, similar to the $LvsI$ profile of a *non-constant length airgap*, as depicted in **Fig.2.6**. When current increases, the flux density and the reluctance of the *saturation-gap* segment increases, reducing the effective inductance. When the flux density level is reaching the *QSE*, the *saturation-gap* segment presents almost constant reluctance, defining the value of linear inductance (5.5). Further increments of the current after the *QSE* is reached, is equivalent to the next operation mode, referred as *full linear bias*.

Full Linear Bias or 100% Bias

- Flux density at \mathcal{R}_{sg} has reached the *QSE*. $B_{sg}(I = 0) = QSE$.
- Flux density at \mathcal{R}_{bias} is at the limit of the linear region ($-B_{sat}$) of the 3rd quadrant. $B_{bias}(I = 0) = -B_{sat}$.

When current increases, the operation point of \mathcal{R}_{bias} moves from the linear region of the 3rd and 1st quadrants, towards the *QSE* near the saturation flux density, B_{sat} at the 1st quadrant of the *BH*-loop. In the current range at which \mathcal{R}_{bias} is within the linear region of the 1st and 3rd quadrants, the value, of the nominal inductance, L_N remains constant (5.5). The saturation current, I_{sat} of the *PMBI*, is determined when operation point of \mathcal{R}_{bias} has reached the saturation flux density at the 1st quadrant.

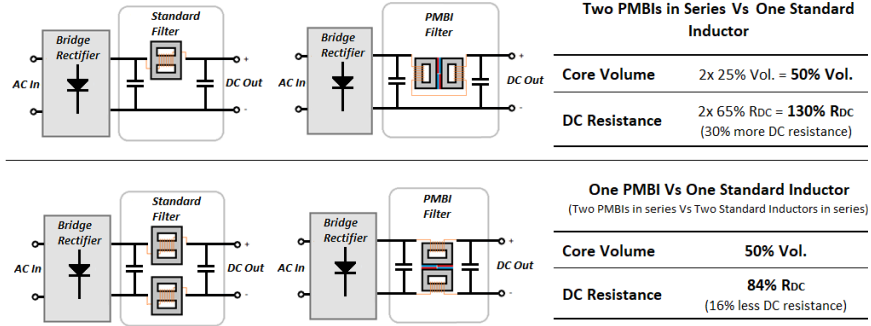


Fig.5.5. Comparison between one or two standard *DC* inductors in series implemented by one pair of *UU* inductors biased with the *Saturation-gap* topology. Volume and *DC* resistance comparison data, from physical prototypes documented in appendix P2 [25] and P4 [27].

Pre-Saturated or Over-Linear-Bias

- Flux density at \mathcal{R}_{Sg} has reached the QSE . $B_{Sg}(I = 0) = QSE$.
- Flux density at \mathcal{R}_{bias} has reached the non-linear region at the 3rd quadrant. $B_{bias}(I = 0) < -B_{Sat}$.

At initial conditions, ($I = 0$) the operation point of the reluctances \mathcal{R}_{bias} and \mathcal{R}_{Sg} are outside the linear region of the BH -loop, presenting relatively high reluctance and initially low inductance. As current increases, the operation point of \mathcal{R}_{bias} approaches the linear region at the 3rd quadrant and the inductance approaches its nominal value (5.5). In the current range in which the operation point of \mathcal{R}_{bias} , is within the linear regions of the 3rd and 1st quadrants, the *PMBI* presents linear inductor behavior. Within the linear current range, the *PMBI*'s behavior is equivalent to the operation mode, *full linear bias*.

5.4. DESIGN PROCEDURE

The *Saturation-gap* topology as depicted in **Fig.4.1.c)** is not a single biased inductor, but rather two *UU* inductors biased by the same pair of *PMs*. Circuit designs requiring two separated *DC* inductors can be substituted by one pair of *PMBIs* using the *saturation-gap* topology as depicted in **Fig.5.5.bottom)**. If the circuit design requires

PERMANENT MAGNET BIASED INDUCTORS

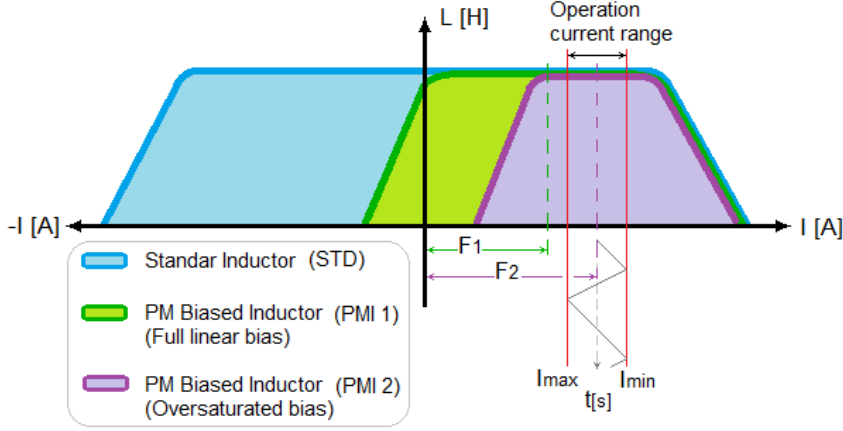


Fig.5.6. Generic *LvsI* profiles of a non-biased inductor and two *PM* biased inductors, *PMBIs*. Standard inductor (blue), Full linear bias *PMI1* (green), Oversaturated bias *PMI2* (purple). The operation current ripple is delimited within the red lines. *F1* and *F2*, indicate the magnetizing force introduced by the *PMs* in *PMI1* and *PMI2*. Figure from [27].

only one *DC* inductor, the *Saturation-gap* topology can be used by connecting the two *UU PMBIs* in series or parallel, as depicted in **Fig.5.5.top**). Circuit designs using two separate inductors present higher benefits when using the *Saturation-gap* topology, since the substitution of one *DC* inductor by two *PMBIs* with half the inductance in series presents an increment on the total *DC* winding's resistance. The following design procedure is representative of only one of the two *UU* biased inductors of the *Saturation-gap* topology. It is therefore necessary to determine the required inductance and saturation current for each of the two *UU* biased inductors accordingly.

The required inductor's *area product*, A_p it is representative of its energy storage capability and can be express by their $L I^2$ product, as shown in (2.34):

$$A_p = A_c W_a = \frac{L I^2}{\Delta B J K_u} \quad (5.7)$$

A *PMBI* achieving *full linear biasing* presents a maximum *flux density increment*, ΔB equal to double of its original limit, $2B_{sat}$. This allows for a reduction of half the required area product, A_p for the same energy storage capability as a non-biased *DC* inductor. The design requirements of an inductor can be represented on an *LvsI* graph. Depending on the specific application, the inductor is required to provide a certain level of inductance, L within an *operation current range* $[I_{min} \leftrightarrow I_{max}]$. **Fig.5.6.**

DESIGN ANALYSIS AND SIMULATION OF THE SATURATION-GAP TOPOLOGY

shows the $LvsI$ profile of a non-biased inductor and two $PMBIs$. The red vertical lines delimit the *operation current range* $[I_{min} \leftrightarrow I_{max}]$ and inductance requirement, typical of a *buck converter*, operating in continuous conduction mode. These requirements are being fulfill by all three filters, independently of their different $L I^2$, area product, A_p and size requirements due to the effect of biasing magnetizing forces F_1 and F_2 . The area enclosed in the $LvsI$ profiles, can provide an intuitive indication of the relative volumes of the three inductors. The required $LvsI$ area of a $PMBI$, achieving *full linear biasing*, is reduce by half as compared to a non-biased inductor design. The possibility of *oversaturated biasing* states allows for the further reduction of the required $LvsI$ area, by concentrating its linear area to the operation current limits.

A good characterization of the BH -loop of the core material and 2D FEA simulations are required to predict accurately the biasing current and the equivalent reluctance of designs using the *Saturations-gap PMBI* topology. Higher accuracy can be achieved by 3D FEA simulations. Nevertheless, a good estimation of the design parameters can be achieved, based on the simplify MEC model calculations, proposed in the previous sub-chapter. The simplified design calculation is summarized with the following procedure:

1st. Defining the PMBI core's dimensions

In order to achieve the inductance and current required by the inductor design, the associated inductor parameters must satisfy the condition defined in (2.49):

$$LI = N \phi_{max} = N B_{Sat} A_c \quad (5.8)$$

The limit of the LI area, as depicted by the blue curve in **Fig.2.6**. is asymptotic with both axes ($I = 0A$ and $L = 0H$). In the case of non-biased inductors, the axes $I = 0A$ is equivalent to the zero flux axes ($B = 0T$). In the case of $PMBIs$ the $B = 0T$ axes is equivalent to the $I = NF_{bias} = I_{bias}$ axes. Where F_b is the biasing magnetization force, as depicted in **Fig.5.6**. as F_1 or F_2 . Accordingly, the required LI product of a $PMBI$ can be define as:

$$LI = L_N (I_{max} - I_{bias}) = N B_{Sat} A_c \quad (5.9)$$

The I_{bias} is equal to the current at which $B = 0T$. For designs in *Full Linear Bias* operating mode:

$$I_{bias} = \frac{I_{max}}{2} = \frac{N \phi_{sat}}{L_N} \quad (5.10)$$

For designs in *Over-Saturated* operating mode:

PERMANENT MAGNET BIASED INDUCTORS

$$I_{bias} = \frac{I_{max} - I_{min}}{2} \approx \frac{N \phi_{sat}}{L_N} + \frac{2 * N (\phi_{bias} - \phi_{sat})}{L_N} \quad (5.11)$$

After determining the inductance and current product, LI required by the application, the common procedure for inductor design as detailed in **Chapter 2.3**. can be used.

2nd. Defining the required PM's area

Initially, a *PM* material must be chosen. Ferrite cores, present a high electric resistivity and relatively low saturation limit, and must be biased using *PM* materials with a similarly high electric resistivity like *bonded NdFeB* or hard ferrites. Laminated steel cores present a higher saturation flux limit. They are typical employed for low frequency applications, and can be biased using sintered *NdFeB* magnets, which presenting lower electrical resistivity, but can provide a higher *remanence flux density*, B_r . The total *PM's* flux, ϕ_{PM} on the core's reluctances at zero current condition, determines the possible operation mode of the inductor as indicated in **Fig.5.3.**, and can be calculated as:

$$\phi_{PM} = A_{PM} B_r = A_c (B_{bias} + B_{Sg}) \quad (5.12)$$

For the case of operation mode of *Full Linear Bias*, the flux density of the saturation-gap segment, B_{Sg} is equal to QSE and the flux density at the biased core segment, B_{bias} is equal to B_{sat} . In case of *Over-Linear-Bias* mode of operation, B_{Sg} is equal to QSE and B_{bias} is equal to the desired displacement of the zero flux axes. The exact flux density value of the QSE can only be measured empirically or calculated using *3D FEA* simulations. The QSE is expected to be slightly higher than the saturation, B_{sat} . For design simplicity, a QSE value equal to $1.25 B_{sat}$ can provide a good estimation. The remanent flux density B_r of the *PM* material and the desired ϕ_{PM} , defines the required *PMs* area A_{PM} .

$$A_{PM} = \frac{\phi_{PM}}{B_r} \quad (5.13)$$

The eddy current losses in the *PMs* are proportional to their electric resistivity. The electrical resistivity of any *PM* material can be increased by “insulated *PM* laminations” or by increasing the binding insulator percentage of bonded *PM* compounds. These techniques can increase the *PM* resistivity at expenses of requiring a larger *PM* area, A_{PM} . The available space for the required *PMs* area A_{PM} , is only limited by the length of the *UU* core legs. If having the freedom of choosing the length of the *UU* cores, any biasing level and eddy current losses can potentially be achieved.

3rd. Defining the required PM's length

The last step is to use the nominal inductance, L_N according to (5.5), to determine the required PM reluctance, \mathcal{R}_{PM} . Since the PM 's area A_{PM} is already fixed by the previous step, the PM reluctance, \mathcal{R}_{PM} must be adjusted by defining the PM 's length, l_{PM} .

$$l_{PM} = \frac{\mu_{PM} A_{PM} N^2}{L_N} \quad (5.14)$$

If the calculated PM 's length, l_{PM} is too short for practical purposes, a smaller number of turns, N needs to be chosen in (5.9). Increasing the PM 's length, l_{PM} results in higher reluctance, $\mathcal{R}_{PM} \approx \mathcal{R}_{Sg}$ and longer equivalent airgap. Final corrections of the required inductance, $LvsI$ profile can be achieved by adjustments of the PM 's length and the distances between the PM s and between the PM s and the UU cores [27].

PERMANENT MAGNET BIASED INDUCTORS

6. CONCLUSIONS ON PERMANENT MAGNET BIASED INDUCTORS

The present thesis analyses the theory and implementation of *permanent magnet biased inductors*, *PMBIs* for *DC* applications. A brief introduction on the research motivations and history of *PMBIs* has been presented in Chapter 1. The theoretical background related to analysis and design of *PMBIs* have been introduced in Chapter 2. A review of the state of the art, and the different topologies and design strategies found in the scientific literature has been presented in Chapter 3. The main advantages and limitations of the different topologies and design approaches are analyzed. None of the topologies found in the literature are documented to achieve *100%* biasing in both ferrite and *SiFe* lamination cores. A practical investigation towards a new topology with improved characteristics has been presented in Chapter 4.

The new biasing topology, referred as *Saturation-gap*, has been introduced and analyzed in Chapter 5. A practical design procedure and empirical measurements on physical prototypes are also presented. *Full linear biasing (100%)* has been practically achieved, in both ferrite and *SiFe* laminated cores. Higher biasing levels (*over-saturated biasing*) have also been empirically achieved with ferrite, providing the possibility of biasing improvement factor higher than two times, $BIF > x2$.

Several prototypes were physically implemented, using both ferrite and laminated steel cores for different *DC* inductor applications. The implemented designs achieve the target *inductance vs current*, *LvsI* profiles while presenting a reduction of size, up to a *50%* of the total inductor volume. The main characteristic of the presented *Saturation-gap* topology and the achievements of the physical implementations are summarized in the following bullet points:

- ✓ The *Saturation-gap* can be implemented using standardized *UI* or *UU* core shapes.
- ✓ The *PMs*, in the *Saturation-gap* topology, present two distinctive functions: to partially saturate a short section of the core achieving the equivalent reluctance of a typical *airgap*, and to provide the desired biasing flux in the rest of the core.
- ✓ Empirically achieved *100%* biasing flux in, both ferrite and laminated *SiFe* core materials.
- ✓ *Over-saturated* bias flux levels ($>100\%$) have been achieved empirically in ferrite cores. Any biasing level could be achievable in any core material by adjusting the ratio between the core and the *PM's* cross-sections: A_{PM}/A_c .

PERMANENT MAGNET BIASED INDUCTORS

- ✓ *PMs* are placed outside the magnetic circuit of the coil's flux, avoiding strong opposing demagnetizing fields and minimizing losses due to eddy currents in the *PMs*. The maximum *PM's area*, A_{PM} is not limited by the core's *area cross-section*, A_c . Any A_{PM}/A_c ratio can be achievable by increasing the length of the *UU* cores.
- ✓ A calculation procedure has been developed using a simplified *MEC* analysis, allowing for design of the linear inductance range of the *PMBIs*, despite the complexity associated with the use of the *non-linear saturation* region of the ferromagnetic cores.

The development of the Saturation-gap topology has been documented in three conference papers and one journal publication, presented in the attached publications: P1, P2, P3 and P4. During the development and investigation of the *Saturation-gap* biasing topology, a number of ideas relating to similar topologies and special inductor applications were identified. The following chapters briefly summarize the further possibilities of *PM-inductors* and possible lines for future research.

Part 2

Additional investigations on:

Biasing topologies for AC
applications

Parametric transformers using
permanent magnets

and

Optimization of conduction
losses on planar transformer
windings

PERMANENT MAGNET BIASED INDUCTORS

7. INVESTIGATIONS ON SYMMETRIC BIASING TOPOLOGIES FOR AC APPLICATIONS

This chapter briefly summarises additional experimentation performed in order to identify further possibilities and fields for future research, for the *Saturation-gap* topology oriented to *AC* applications. The experiments focus on the potential of similar *PM-inductor* topologies for providing a symmetric biasing, suitable for size reduction of inductors operating in *AC* applications. Several *Symmetric-Saturation-gap* topologies are being presented in this chapter. *FEA* simulations and experiments on physical prototypes were performed. In spite of the positive results achieved on the *FEA* simulations, only a relatively small improvement has been achieved on a prototype using ferrite core, and no significant improvement was achieved using steel laminations cores.

7.1. INTRODUCTION TO AC-BIASING

The benefits of magnetic biasing of inductors operating in *DC* applications are widely known. Biased *DC* inductors present higher energy density compared to non-biased ones. On the other hand, the possibility of magnetic biasing of inductors intended for *AC* operation is generally not identified. Not a single scientific publication has been found on the subject of *AC* biasing. The generic techniques used in *DC* biasing topologies are incompatible with the idea of *AC* biasing. These classic *DC* topologies, as well as common non-biased inductors, utilize one or more airgaps within the magnetic length of the core in order to provide an energy storage medium. The core presents an initial magnetic flux in opposite direction to the flux induced by the *DC* current in the windings. This biasing flux is only required inside the core material and is not necessary to be present at the airgaps. *PMs* are typically placed inside the airgap, or near the airgap, in order to introduce a predefined magnetic flux inside the core. The *PM's* flux is generally designed to extend the core's saturation limit for one current direction, at the expense of reducing the saturation limit for the opposite current direction. The flux distribution is fixed by the polarity of the *PMs* and their relative position to the airgap. In order to enhance the energy density of inductors operating with *AC* currents, a different biasing strategy needs to be used.

The saturation-gap *DC* biasing topology uses the *PMs* as energy storage medium and does not require physical airgaps. This particular property, of the saturation-gap

Symmetric Biasing for AC Inductors

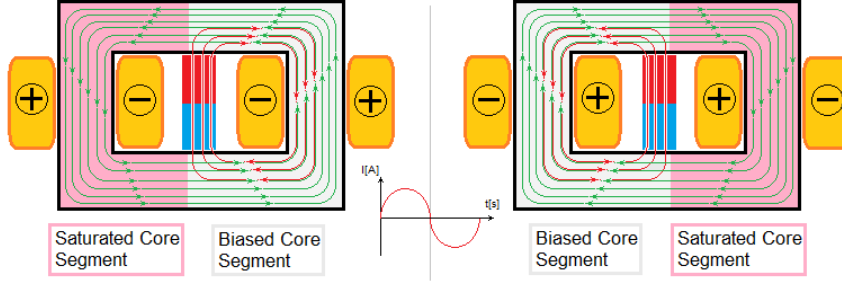


Fig.7.1. Magnetic Flux Distribution in an *AC-Biased* Inductor. *Left:* Positive current; *Right:* Negative current. The positive “+” polarity in the coils (in orange) correspond to current into the page, the negative “-” polarity current out of the page. Green vectors represent magnetic flux induced by the coils current. Red vectors represent magnetic flux produced by the permanent magnet (in red and blue). Pink colored areas represent core saturation and provide the increased reluctance of the typical airgap.

concept, can be exploited for the development of the *AC* biasing concept. **Fig.7.1.** presents a first approach of an *AC-biasing* topology, using a magnetic core with no airgaps and one *PM* in its axis of symmetry. This topology is similar to the basic *DC-bias saturation-gap* topology. As current increases, one segment of the core is biased, while the other segment becomes saturated. In the case of the *AC-biasing* topology, the saturated core segment and the biased core segment are both the same length. The direction of the current will determine which segment of the core becomes saturated or biased. During the positive semi-cycle of an *AC* current, one of the core segments is fully biased, presenting extended saturation flux density limit, while the other core segment is partially saturated, providing a higher reluctance, similar as a *distributed airgap*. The reluctance of the saturated segment is approximately equal to the *PM* reluctance. During the negative current semi-cycle, the behavior of the core segments swaps, the biased segment of the core becomes partially saturated and vice versa. Since the length of the two segments is identical, the inductor will present the same inductance for both current directions. The permeability of the core in the biased segment is very high and the total reluctance of the non-gapped core is practically dominated by the saturated segment. Therefore, the *inductance*, L can be defined by the magnetic reluctance of the saturated segment, \mathcal{R}_{Sg} as:

$$L = \frac{N^2}{\mathcal{R}_{Sg}} \quad (7.1)$$

INVESTIGATIONS ON SYMMETRIC BIASING TOPOLOGIES FOR AC APPLICATIONS

AC-Biasing Topologies with Saturation-gap

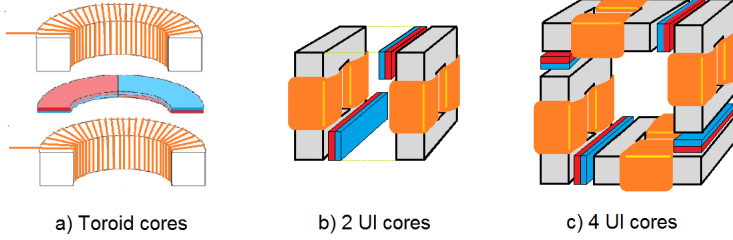


Fig.7.2. *AC-Biasing Topologies with Saturation-gap.* Permanent magnets, PM s in red and blue; Windings in orange. One pair of inductors, or four inductors in case c), are symmetrically biased by PM s. The separated inductors can operate connected in series or parallel.

Where N , is the number of turns, and the reluctance of the biased segment is considered depreciable in comparison to \mathcal{R}_{Sg} . As shown in (5.1) and (5.5), the reluctance of the saturated segment is defined by the reluctance of the PM and can be approximate as:

$$\mathcal{R}_{Sg} \cong \mathcal{R}_{PM} = \frac{l_{PM}}{\mu_{PM} A_{PM}} \quad (7.2)$$

Where l_{PM} is the length of the PM through its axis of magnetization, and A_{PM} its area cross-section. The PM 's permeability, μ_{PM} is typically slightly above the vacuum permeability, μ_0 . In principle, when full lineal biasing is achieved, the saturation current, I_{sat} is increased to double its original value, while maintaining the nominal inductance, L_n . Unfortunately, the windings operating on the saturated segment are subject of lower magnetic induction, $d\phi/dt$ due to the equilibrated variation of the PM s operation point. The level of eddy currents on the PM s, allowed in the design, the ratio of wound core length to the total core length and the profile of the core's saturation knee, will influence the percentage of the total flux variation, $d\Phi/dt$ present in the saturating segment. It is theoretically expected that the higher the eddy current losses allowed at the PM s, the greater the induction in the windings and the bigger the achievable $L_n I_{sat}$ product.

The topology depicted in **Fig.7.1.** can be useful to provide an intuitive understanding of the *AC-biasing* possibility. On the other hand, the relative dimensions of the core and PM presents serious limitations for the practical implementation of this topology. The depicted PM presents an elongated geometry ($l_{PM} \gg A_{PM}$) resulting in a relatively big magnetic reluctance, \mathcal{R}_{PM} and consequently big equivalent gap

reluctance, \mathcal{R}_{Sg} . This implies a direct design limitation for the minimum achievable value for \mathcal{R}_{Sg} , similar to a shortest possible equivalent airgap. In order to reduce the minimum achievable equivalent airgap, the *PM* geometry needs to be closer to a plate ($A_{PM} \gg l_{PM}$), reducing its magnetic reluctance, \mathcal{R}_{PM} .

7.2. POTENTIAL AC-BIASING TOPOLOGIES

In order to provide a symmetric flux distribution, similar to **Fig.7.1.**, while using *PMs* with lower reluctance ($A_{PM} \gg l_{PM}$), the topologies depicted in **Fig.7.2.** has been proposed. The topology in **Fig.7.2.a)** presents a symmetric *AC-biasing* magnetization on a pair of toroid cores, using half-ring *PMs*. The two inductors can be connected in series or parallel in order to increase the inductance or current rating respectively. In this topology, the *PMs* are separate from the cores by the copper windings. This greatly lowers the operation point of the *PMs*, requiring a bigger magnet area, A_{PM} in order to achieve the desired level of biasing flux. On the other hand, this topology presents all its magnetic length available for *PM* surface and *full lineal biasing* and *over-saturated biasing* states are practically achievable. The *PM's* length, l_{PM} is not limit by any core or windings design restrictions and subsequently there is no limit for the minimal achievable equivalent airgap.

Fig.7.2.b) presents a symmetric *AC-biasing* magnetization on a pair of UI (or UU) cores, using plate *PMs*. In this topology, only a portion of the magnetic length is available for *PM* surface. On the other hand, the *PMs* are in direct contact with the magnetic cores, rising their operation point and the induced biasing flux, reducing the minimum required *PM* surface. *Full lineal biasing* and *over-saturated biasing* states are also easily achievable with this topology. The minimum *PM* length, l_{PM} and equivalent airgap are limited by the thickness of the windings. The thicker the winding bundle is, the longer the required *PM* and the longer the minimum achievable equivalent airgap. This topology is practical in high frequency applications where single layer windings are commonly used.

Medium and low frequency inductors, presenting multiple layer windings, will benefit from the topology depicted in **Fig.7.2.c)**. Very similar to the previous topology, while using four UI cores with square area cross-section, A_C . This configuration allows the use of *PMs* shorter than the thickness of the windings, presenting no limitations for the minimum achievable equivalent airgap. The square cross-section of the core ($l_x = l_y$) is required for matching the *PM* surface between adjacent UI cores. A square cross-section optimizes the required winding length for any given rectangular area, A_C , reducing the total winding resistance. On the other hand, this topology requires four separate cores, which can be connect in series or parallel depending on the desired current and inductance.

INVESTIGATIONS ON SYMMETRIC BIASING TOPOLOGIES FOR AC APPLICATIONS

7.3. PRACTICAL IMPLEMENTATIONS

The topologies presented in **Fig.7.2.b)** and *c)* have been physically implement and empirically tested using inductor characterization measurements. A high frequency ferrite and a low frequency laminated steel core materials has been use for the implementation of the two topologies, respectively. The *AC-PMBI* inductors were compared to equivalent non-biased designs using regular airgaps.

- **Implementation 1: High frequency ferrite inductor.**

Table 7.1. presents the design parameters of the standard and biased inductors following the topology depicted in **Fig.7.2.b)**. The two UU inductors are connected in series. The *PM* length it is adjusted in order to achieve the same nominal inductance as the non-biased design using a standard airgap. Both inductors use the same cores and windings. **Fig.7.3.right.** presents the measured inductance vs current profile, *LvsI* of the *PMBI* and the standard, *STD* inductors.

- **Implementation 2: Low frequency laminated steel inductor.**

Table 7.1. presents the design parameters of the standard and biased inductors following the topology depicted in **Fig.7.2.c)**. This topology uses 4 UI inductors. Two inductor pairs connected in series, are connected in parallel with other two series inductors. The *PM* length it is adjust in order to achieve the same nominal inductance as the non-biased design using a standard airgap. Both inductors use the same cores and windings. **Fig.7.4.** presents the measured *LvsI* and *ESRvsI* of the *PMBI* and the standard, *STD* inductors.

	Implementation 1 Ferrite Core		Implementation 2 Steel Lamimnations Core	
	Biased AC Inductor Topology: Fig.7.2.b)	Standard AC Inductor	Biased AC Inductor Topology: Fig.7.2.c)	Standard AC Inductor
Nominal Inductance, L_n [mH]:	0.13	0.13	1.5	1.5
Saturation Current, I_{sat} [A]:	45	35	15	15
Core Material:	Ferrite N87	Ferrite N87	Silicone Steel	Silicone Steel
Core Type:	(2x) UU 60/35/15	(2x) UU 60/35/15	(4x) UI30	(4x) UI30
Saturation Flux Density, B_{sat} [mT]:	450	450	1.2	1.2
Magnetic Length, l_m [mm]:	202	202	60	60
Area cross-section, A_c [mm ²]:	225	225	100	100
Air-gap length, l_g [mm] (total):	0	4	0	1.2
Number of turns (on each core):	32	32	64	64
Wire diameter, W_d [mm]:	3	3	1.6	1.6
Permanent Magnet, PM's Material:	Bonded-NdFeB BN-7	None	Sintered-NdFeB N42	None
Remanent Flux Density, B_r [mT]:	800	-	1.2	-
PM's Area cross-section, A_{PM} [mm ²]:	360	-	300	-
PM's Length, l_{PM} [mm]:	10	-	2	-

Table 7.1. Design parameters of the two *AC*-bias prototype implementations.

PERMANENT MAGNET BIASED INDUCTORS

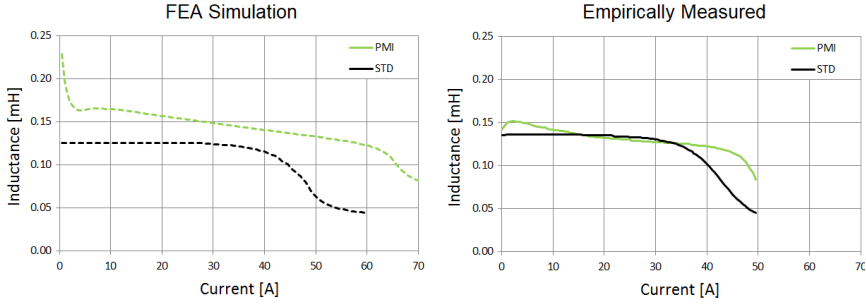


Fig.7.3. Inductance vs Current, ***LvsI*** profiles of the standard non-biased (***STD***, in black) and ***AC-biased*** (***PMI***, in green) inductors. Core material: *Ferrite N87 (Implementation-1)*. *Left*: Calculated using *2D FEA* simulations with *FEMM*. *Right*: Empirically measured on physical inductors with *WK3260B* magnetic analyzer. Stimulus *1V AC 30 kHz*, *DC* current from *0A* to *50A*.

7.4. FEA SIMULATIONS

The accurate simulation of the particular geometry of the *AC-biasing* topologies, depicted in **Fig.7.2.**, would require a *3D* model based simulation. In order to provide an intuitive understanding of the main behavior of the topology presented in **Fig.7.2.b)** (implementation 1), a *2D FEA* simulation has been use. In order to represent the proposed topology with a *2D* model, several approximations needed to be taken. The models have been implemented with software *FEMM*, using a “symmetric boundary”. The total magnetic length of each *UU* core is represent as straight segments. These boundaries are defined as “symmetric”, meaning the simulation software consider them directly connected to each other. These models can represent the overall idea of

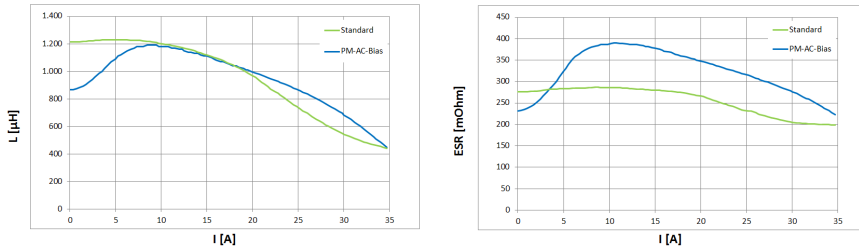


Fig.7.4. Measured ***LvsI*** and ***ESRvsI*** of the ***AC-PMBI*** and standard non-biased reference inductor. Core material: Steel laminations *EI30 (implementation-2)*. Measured on the physical inductors with *WK3260B* magnetic analyzer. Stimulus *1V AC 300 Hz*, *DC* current from *0A* to *35A*.

INVESTIGATIONS ON SYMMETRIC BIASING TOPOLOGIES FOR AC APPLICATIONS

the proposed topology. On the other hand, the rectangular shape of the magnetic length, and the relative length of the independent segments of each UU core is not representable, and important deviations from experimental results are expected. The simulation has been run for a range of current values in steps of $0.5A$, and the incremental inductance, L as function of DC current is calculated. The simulated $LvsI$ profiles, of the $PMBI$ and the STD inductors, are present in **Fig.7.3.left**.

7.5. CONCLUSIONS ON AC-BIASING

The concept of magnetic biasing suitable for AC inductors have been investigate. Two different experimental AC -biased prototypes have been implemented. The first implementation consisted of a high frequency ferrite inductor with the topology depicted in **Fig.7.2.b**). The second implementation consisted of a low frequency laminated steel inductor using the topology depicted in **Fig.7.2.c**). The first implementation achieved 20% increase of the $LvsI$ product as compared to the reference gapped ferrite inductor. This improvement of the energy density, of an AC inductor, can be consider a proof of concept of the symmetric biasing idea. In spite of the $2D$ simulation predicts approximately 40% increase of the $LvsI$ profile; the improvements measured on the physical prototypes were minimal. These big deviations between simulated and measured results are expect due to the intrinsic limitations of the $2D$ representation of this topology. The second implementation using the laminated steel inductors did not achieve any significant improvement on the $LvsI$ profile of the biased inductor, as compared to the non-biased reference. The causes for this lower performance, of the symmetric biasing concept, with the laminated steel inductor may be due to a number of different factors, such: the total flux variation at the saturated segment, level of *eddy currents* in the PMs , the shape of the saturation knee of the core material and the overall geometry of the used cores.

Despite the promising results predicted by the FEA simulation, the experimental analysis on the physical prototypes did not provide significant results. No further research has been performed towards finding possible symmetric topologies suitable for size reduction, of power inductors operating in AC applications.

PERMANENT MAGNET BIASED INDUCTORS

8. INVESTIGATIONS ON THE USE OF PM-INDUCTORS AS PARAMETRIC TRANSFORMERS

This chapter briefly introduce the concept and properties of *Parametric Transformers*, *PTs*. It also analyses the characteristic *non-inductive coupling* between the two coils on the *Saturation-gap* topology and shows its potential as a controllable variable inductance suitable to produce *parametric oscillations*. A new symmetric *Saturation-gap* topology has been developed and a prototype was physically implemented. Its performance operating as a *PT*, is analysed and compare with other documented *PT* topologies. The new, *Saturation-gap* based, *PM-PT* topology presents increased power density and efficiency compared with previous *PT* topologies. The history and principles of *parametric oscillations* and the analysis and calculations of the new *PM-PT* topology are being documented in more detail on an article published on the *IET Journal of Power Electronics*, listed as **P5** in the publication's appendix.

8.1. INTRODUCTION TO PARAMETRIC TRANSFORMERS

Similar in appearance to conventional electric transformers, *Parametric Transformers*, *PTs* are magnetic devices with a ferromagnetic core and two (or more) coils. Despite their similarity, the electric properties of *PTs* are very different and characterized by:

- There are two distinct magnetic flux circuits in the ferromagnetic core.
- Each magnetic flux circuit links only one of the two coils.
- Zero (or negligible) *Magnetic Flux Linkage*, λ_{12} between the primary and secondary coils. $\lambda_{12} = 0$
- The two flux circuits are sharing a common reluctance element.
- Mutually dependent primary and secondary Inductances: $L_1(I_1, I_2) = \frac{N_1^2}{\mathcal{R}_1(H_1, H_2)}$

The operation of *PTs* is based on the principle of *parametric oscillations*. The secondary winding of *PTs* is always connected to a capacitor, forming a resonant *LC-tank* typically in parallel with the load. An *alternating current*, *AC* in the primary windings produces a synchronous variation of the secondary inductance. Only when

PERMANENT MAGNET BIASED INDUCTORS

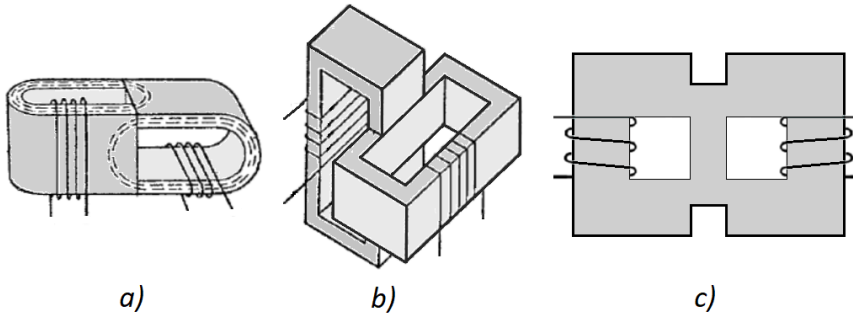


Fig.8.1. Parametric Transformer, *PT* topologies. *a)* Parallel-flux topology (1974) [41]. *b)* Orthogonal-flux topology (1974) [41]. *c)* Parallel-flux planar topology (2010) [42].

the primary *AC* frequency matches the resonant frequency of the secondary *LC-tank*, oscillations are being excited, and energy is transferred to the load. Due to their operation principle, *PTs* present some interesting advantages and desirable properties:

- Bidirectional Filtering. Energy is only transfer at a desired resonant frequency, eliminating EMI noise and propagation of line harmonics.
- Voltage regulation. Intrinsic output voltage limit provide safety, constant voltage load regulation without requiring control circuit, and a range of immunity to input voltage variations.
- Short-circuit protection. Electric and magnetic de-coupled input-output allows for short-circuited output with no reflection to the input.

Oscillations on the *LC-tank* tend to grow with every *AC* cycle until reaching the saturation limit of the magnetic core, thus achieving a constant output voltage for a good range of input voltages and load conditions. Since primary and secondary windings do not present inductive coupling, *PTs* provide a good input-output filtering and *short-circuit* protection. There are a great number of possible core topologies presenting the characteristics required for parametric transformers. **Fig.8.1.** shows the three more common topologies found on the literature. Due to their desired properties, *PTs* has been used for an important number of *AC* applications, like power factor correction, bidirectional *AC* power transfer control and filtering. The input of *PTs* can be driven with squared *AC*, using *DC* sources and a *H-bridge* or a *push-pull* circuit, while maintaining and almost sinusoidal current. The mechanism used for achieving inductance variations on all these topologies is based on the saturation of the common reluctance elements. These topologies can achieve inductance variations only if the input current is reaching the non-linear region of the common reluctance element.

INVESTIGATIONS ON THE USE OF PM-INDUCTORS AS PARAMETRIC TRANSFORMERS

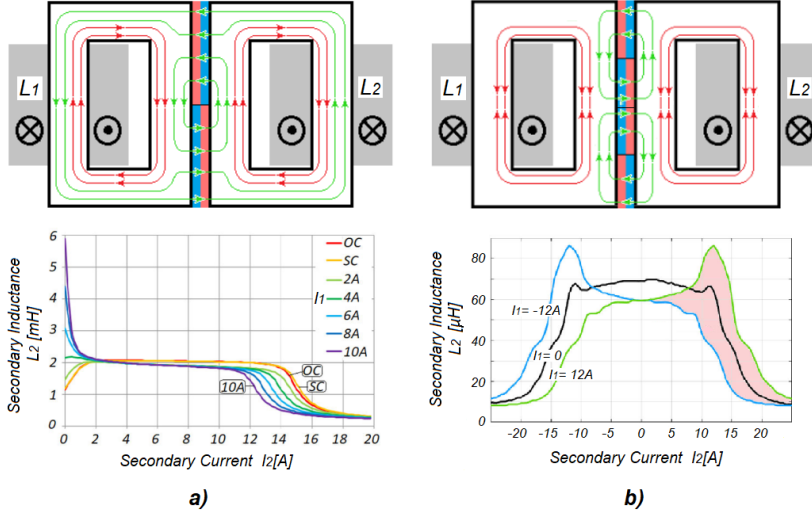


Fig.8.2. Saturation-gap topologies as Parametric Transformers. **a)** DC Saturation-gap topology (top), and secondary inductance vs current, L_2 vs I_2 profile (bottom), at different primary conditions: Open-circuit (OC), Short-circuit (SC) and a range of DC currents. **b)** AC Symmetric Saturation-gap PM-PT topology (top), and secondary inductance vs current, L_2 vs I_2 profile (bottom), measured at three primary currents: 0A , -12A and 12A .

Despite the advantages and useful properties of *PTs*, their energy density and efficiency are very limited, and *PTs* only experience a short fame during the 70's and 80's. Due to the continuous developments in power semiconductor technologies and switching control methods (*PWM*) for load regulation, the use of *PTs* has been very reduced in the following decades and has become almost forgotten in present days. [42]-[45].

8.2. NON-INDUCTIVE COUPLING ON THE SATURATION-GAP TOPOLOGY

At first sight, the *PMBI Saturation-gap* topology, as depicted in **Fig.8.2.a)(top)**, or **Fig.4.1.c)**, can be mistake by a transformer, due to the presence of two distinct windings. On the contrary, this topology is better described as two separated inductors simultaneously biased by the same pair of *PMs*. The two biased inductors are commonly connect in series or parallel, in order to perform as a single biased inductor. In order to analyze the coupling between the two windings in the *Saturation-gap* topology, a practical experiment on a physical prototype has been perform. The

prototype uses the topology depicted in **Fig.8.2.a)(top)**, using *N87 Ferrite UU/46/30* cores, with 80 turns in both windings and *3mm bonded-NdFeB PMs*. The *inductance vs current* profile, $L_2 vs I_2$ of the *secondary* winding, has been empirically measured for a number of conditions at the primary windings: *open-circuit*, *short-circuit*, and a number of *DC* current levels. **Fig.8.2.a)(bottom)** shows the measured $L_2 vs I_2$ profiles. It is clearly noticeable that the *secondary* $L_2 vs I_2$ profiles, with *open-circuit (OC)* or *short-circuit (SC)* conditions at the *primary* windings, are identical. This is good evidence of none, or minimal coupling or flux linkage exist between the *primary* and *secondary* windings, $\lambda_{12} = 0$. Nevertheless, a *DC* current present on the *primary* windings, does shift the biasing level and the $L_2 vs I_2$ profile of the *secondary*, as shown in **Fig.8.2.a)(bottom)**. The $L_2 vs I_2$ profile can shift from *over-biased* to *under-biased* states, depending on the current through the *primary*. The higher the *primary* current the lower the biasing level achieved at the *secondary*. The *non-inductive coupling* and the capability of producing inductance variations with this *PMBI* topology, present a potential mechanism for a new topology of *PT*. On the other hand, the $L_2 vs I_2$ profile of this *Saturation-gap DC-bias* topology as shown in **Fig.8.2.a)** is always biased at some degree and the inductance is concentrated in the positive range of the *secondary* current.

8.3. NEW SYMMETRIC SATURATION-GAP PM-PT TOPOLOGY

Since *PTs* are meant to operate with *AC*, a similar symmetric *PM-PT* topology was developed based on the *Saturation-gap* concept. The new *PM-PT* topology is depict in **Fig.8.2.b)**. The green vectors represent magnetic flux produced by the *PMs*. The red vectors represent magnetic flux produced by the windings. Since this topology use *AC*, the red vectors are depicted with double polarity. This topology uses a double pair of *PMs*, presenting a symmetric distribution of the *PM's* flux on the cores. A physical prototype was built using *N87 Ferrite UU/30/19* cores with 24 turns in each winding and *1.2 mm* thick *bonded-NdFeB PMs*. The *inductance vs current* profile, $L_2 vs I_2$ of the *secondary* winding, has been empirically measured for both positive and negative secondary currents, using a *WK3260 magnetic analyzer*. The $L_2 vs I_2$ measurements were repeated for a range of positive and negative primary *DC* currents. **Fig.8.2.b) (bottom)** presents the measured $L_2 vs I_2$, at three different primary *DC* currents: $-12A$, $0A$ and $12A$. When there is no current on the primary windings ($I_1 = 0A$), the secondary $L_2 vs I_2$ presents a symmetric profile center at $I_2 = 0A$, similar to a standard non-biased *AC* inductor. Primary current shifts the center of symmetry of the $L_2 vs I_2$ profile, similar to a *PM* biasing effect. The polarity of the primary current determines the biasing direction of the shifted $L_2 vs I_2$ profile. The shaded area in **Fig.8.2.b) (bottom)**, enclosed between the $L_2 vs I_2$ profiles at $I_1 = 12A$ and $I_1 = -12A$, represents the total *LI* product (or flux linkage, λ) variation achieved during a *AC* cycle with a primary current of $12A$ peak. This area, related to the *LI* product displacement, is proportional to the achievable *primary-secondary* energy transfer of the measured prototype.

INVESTIGATIONS ON THE USE OF PM-INDUCTORS AS PARAMETRIC TRANSFORMERS

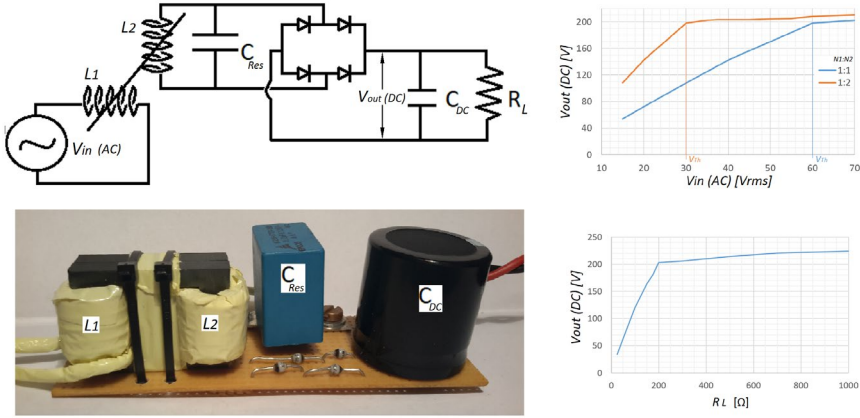


Fig.8.3. AC-DC converter using the *Permanent Magnet Parametric Transformer, PM-PT*. Top-left: Circuit schematic. Bottom-left: Physical prototype. Top-right: Measured V_{DC} vs V_{AC} with two different winding ratios. Bottom-right: V_{DC} vs R_L measured with 1:1 winding ratio, Input voltage, $V_{AC} = 35\text{ V}$, resonant frequency, $f_0 = 36\text{ kHz}$.

8.4. PRACTICAL EXPERIMENTATION

The new *PM-PT* topology has been tested operating in an *AC to DC* converter, using a simple *Full diode bridge* at the output of the secondary *LC-tank*. **Fig.8.3.(top-left)** shows the used circuit schematic. The *PM-PT* is depicted by the symbol presenting the two windings, L_1 and L_2 , in orthogonal relationship, implying there is zero flux linkage between primary and secondary windings. The *Output DC voltage*, V_{DC} as function of the *Input AC voltage*, V_{AC} was measured at the resonant frequency, $f_0 = 36\text{ kHz}$. The converter was tested twice using two different winding ratios, $N_1:N_2$, on the *PM-PT*, 1:1 and 1:2. The measured V_{DC} vs V_{AC} performance of the converter is shown in **Fig.8.3.(top-right)**. When the Input voltage, V_{AC} is above the *voltage-threshold*, V_{Th} the output voltage, V_{DC} remains relatively constant and minimally affected by the input voltage, V_{AC} . The *Output DC Voltage*, V_{DC} using the $N_1:N_2 = 1:2$ ratio, has been measured for a range of load resistance values. **Fig.8.3.(bottom-right)** shows the measured V_{DC} as function of load resistance, R_L . The maximum Output Power is $P_{out} = 200\text{ W}$, at a load resistance of $R_L = 200\Omega$. It can be noticed that the *PM-PT* achieves load regulation, presenting relatively constant voltage, V_{DC} for loads below maximum power. The Output voltage, V_{DC} rapidly decreases if the load resistance is below the maximum power load, $R_L < 200\Omega$, demonstrating the *shot-circuit* protection properties of the *PM-PT*. The physically implemented *AC-DC* converter using the *PM-PT* prototype is shown in **Fig.8.3.(bottom-left)**.

PERMANENT MAGNET BIASED INDUCTORS

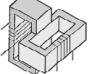
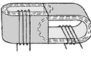
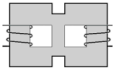
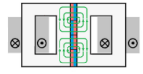
	Previous PT topologies			New PM-PT topology
	Orthogonal-Flux	Parallel-Flux	Parallel-Flux	PM-Parallel-Flux
				
PT topology from ref.	[42]	[42]	[43]	[P5]
year of publication	1974	1974	2010	2020
mechanism for inductance variation	based on saturation	based on saturation	based on saturation	based on PM-biasing
core material	Silicon-Steel	Silicon-Steel	Silicon-Steel	Ferrite MF198A
area product, cm ⁴	not specified	Not specified	1400	116
total mass, Kg	20	20	Not specified	0.058
maximum power [W] (tested on prototype)	360	1200	15	206
efficiency [%] (at max. Power)	50%	67%	not specified	90%
frequency, Hz	1000	1000	50	36000
power density, W/kg	18	60	not specified	3540
energy density, mJ/kg	18	60	not specified	98
input over- and under-voltage protection	yes	yes	yes	yes
output voltage load regulation	yes	yes	yes	yes
short-circuit protection	yes	yes	yes	yes
robust EMI protection	yes	yes	yes	yes
bidirectional filtering	yes	yes	yes	yes

Table 8.1. Comparison of *Parametric Transformers*, *PT* topologies and achievements.

8.5. CONCLUSIONS ON THE NEW *PM-PT* TOPOLOGY

The new *PM-PT* topology presents all the known benefits associated with *PTs* and achieves an efficiency and energy density superior to the previously known *PT* topologies. **Table 8.1.** presents a comparison of achievements of the new *PM-PT* topology with previous *PT* topologies. The new inductance variation mechanism, based on *PM-biasing*, is the cause of the increased energy density. Previous *PT* topologies achieve inductance variations by saturation mechanisms and require the use of *SiFe* lamination cores. The new *PM-PT* topology can be implement using ferrite cores, allowing for higher frequency of operation, and further increasing the achievable power density.

9. INVESTIGATIONS ON COPPER

LOSSES ON HIGH FREQUENCY

PLANAR WINDINGS

This chapter briefly summarizes the challenges associated with the design and implementation of high frequency planar magnetics. A high frequency planar ferrite transformer, with a power rating of 2000 VA , has been physically implemented. The transformer was employed on a converter operating at a frequency of 110 kHz . A scope for possible techniques oriented to overcome some of the limitations arising from high frequency planar design has been performed. A possible technique, for achieving improved current density distribution and lower copper losses, has been identified. An experimental analysis has been made using two different transformer prototypes, and the successful performance of the proposed technique has been verified. The further development and investigations of the possibilities and optimization of the proposed technique will be the focus of future research.

9.1. INTRODUCTION TO PLANAR MAGNETICS

One of the main trends through the last decades, in the field of power electronics, has been a continuous increase of the switching frequency of power converters. Higher frequency allows a higher power density. Faster and more robust power semiconductor technologies (SiC, GaN) are in constant investigation and development, in order to assist to the desired increase in switching frequency. Ferrite core materials achieving low losses at higher frequencies are also in constant development by the material industry. Higher switching frequency translates into smaller inductance requirements and lower volume and weight of the magnetic components. On the other hand, several challenges arise on the magnetic component design at high frequency operation. Due to the *skin effect*, there is a limit in the current penetration depth, (*skin depth*) S_d into the copper conductor's cross-section, A_w . Multicore conductor or foil windings are possible techniques used in common high frequency transformers. The impact of the parasitic capacitances and leakage inductances becomes more dominant at higher frequencies, presenting additional problems with the conventional copper wire wound coils. Planar magnetics are developed in order to approach some of the mentioned limitations associated with high frequency operation. Planar ferrite cores, present a flat profile having a smaller total volume and smaller window area, W_a as compared to standard cores with the same area cross-section, A_c . The smaller core volume allows for lower losses and

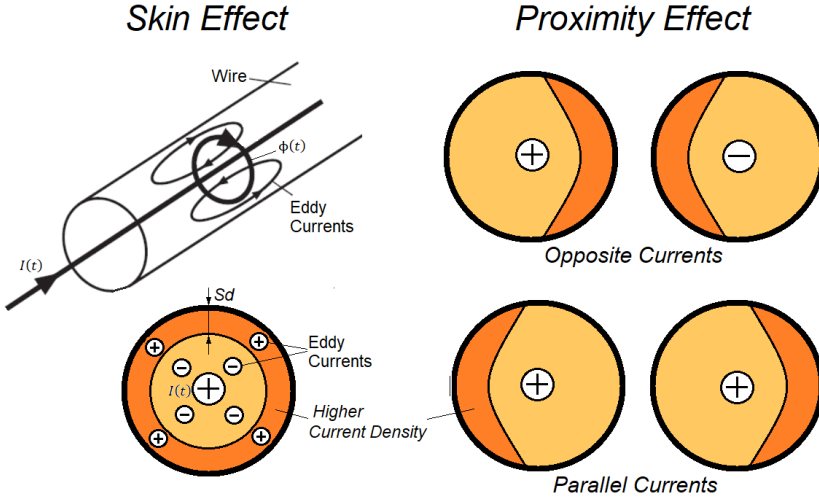


Fig.9.1. Eddy currents in electric conductors. *Left:* The *Skin Effect*, Field vectors in wire (top) and wire's area cross-section, A_W (bottom). *Right:* The *Proximity Effect*, in conductor's cross-section, A_W carrying opposite currents (top), and parallel currents (bottom). Positive sign "+" indicates current into the page, and minus "-" sign indicates current out of the page. Darker orange areas indicate higher current density, $J[A/m^2]$.

better utilization of the maximum usable magnetic flux variation, ΔB within the core's limits, $\pm B_{Sat}$. Due to the lower inductance requirements associated with the higher operation frequency, and higher allowable magnetic flux variations, ΔB , planar transformers typically present a reduced number of turns as compared with common transformers. The windings of planar transformers and inductors can be directly print into multilayer PCBs or using copper foil stampings. These winding techniques allows for better control of parasitic capacitances, better thermal dissipation and more efficient automatized production and replicability. Planar magnetics is a currently growing field of investigation and development with increasing number of scientific articles being publish every year.

9.2. EDDY CURRENTS IN ELECTRIC CONDUCTORS

The main challenges in the design of planar magnetics, arises from high frequency effects associated with eddy currents within the copper conductors. If the frequency is sufficiently high, magnetic fields will be present inside the electric conductor, modifying the current density, $J[A/m^2]$ distribution within the copper conductor's

Investigations on Copper Losses on High Frequency Planar windings

area cross-section, A_W . No-uniform current density distribution induces poor utilization of the total conductor's cross-section, A_W and higher AC resistance, R_{AC} compared to the conductor's DC resistance, R_{DC} . The distortion of the current distribution, $J[A/m^2]$ in a wire, due to the magnetic fields associated with its own current, is known as the *Skin effect*, depicted in **Fig.9.1.(left)**. The distortion of the current density, $J[A/m^2]$ in close wires, due to the interactions of their magnetic fields, is known as the *Proximity effect*, depicted in **Fig.9.1.(right)**. A single conductor carrying a current, $I(t)$ with round area cross-section, A_W is depict in **Fig.9.1.(left)**. A magnetic field, $\phi(t)$ is induced inside the area of the wire, A_W . Eddy currents inside the wire, attenuate the current flowing through the center of the wire's, A_W and concentrate the current density at the periphery of the wire. The maximum current penetration into the conductor is refer as the Skin Depth, and is dependent on the conductor resistivity, ρ magnetic permeability, μ and the frequency, f of the current:

$$Sd = \sqrt{\frac{\rho}{\pi\mu f}} \quad (9.1)$$

For copper conductors operating at a temperature of 25°C, the Skin depth, Sd can be approximated by the expression in (2.33):

$$Sd [mm] = \frac{66.2}{\sqrt{f}} \quad (9.2)$$

A common choice for planar magnetics is PCB printed windings or stamping copper foil windings, with a thickness of twice the *Skin depth*, Sd in order to improve the conductor's area, A_W utilization, as compared standard wires with round cross-section.

9.3. AC LOSSES IN PLANAR WINDINGS

There is an important number of articles in the literature focus on the effort for the accurate prediction of AC losses in planar windings. The interactions of skin effects and proximity effects between all windings present a high level of complexity. A simplified expression for calculating the AC resistance, R_{AC} on each of the layers, originates from the mathematical studies of Dowell, based on the one-dimensional solution of the diffusion equation applied to infinite parallel plates [47]. Based on the analysis of Dowel, further studies provided an expression for calculation of the ratio of AC resistance to DC resistance in planar windings [48][49]:

$$\frac{R_{AC,m}}{R_{DC,m}} = \frac{\delta}{2} \left[\frac{\sinh \delta + \sin \delta}{\cosh \delta - \cos \delta} + (2m - 1)^2 \frac{\sinh \delta - \sin \delta}{\cosh \delta + \cos \delta} \right] \quad (9.3)$$

Where, δ is the ratio between the conductor thickness and the skin depth, Sd :

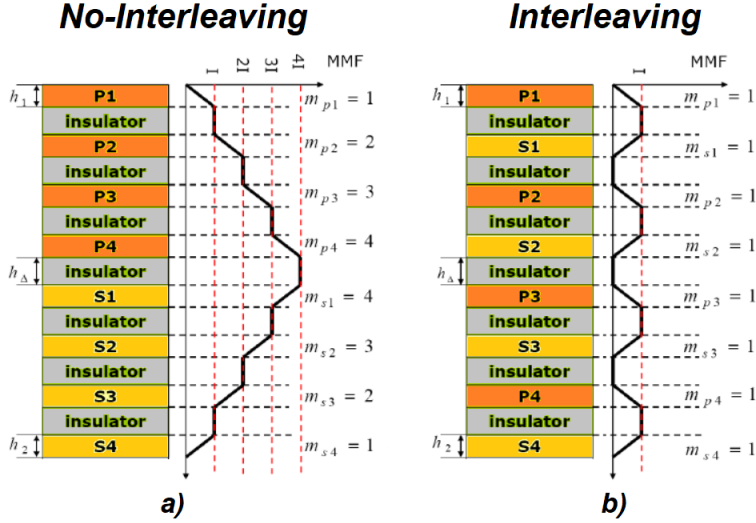


Fig.9.2. Planar winding arrangements, MMF s and proximity loss factor, m on each layer.
 a) No-interleaving windings. b) Interleaving windings.

$$\delta = \frac{h}{sd} \quad (9.4)$$

The factor, m is dependent on the increment of magnetization force, F (MMF) in each layer, and is define as:

$$m = \frac{F(h)}{F(h) - F(0)} \quad (9.5)$$

The calculated m factor for each layer of a planar transformer with four windings in both primary and secondary are presented in **Fig.9.2.** for two different cases of winding arrangements. It can be clearly noticed that the interleaving arrangement, significantly reduces the factor, m , improving the R_{AC}/R_{DC} ratio, compared with the non-interleaving windings. A number of methods are being develop in order to predict and optimize the R_{AC}/R_{DC} ratio, leaking inductances and parasitic capacitances. *FEA* simulations are a common tool for design optimization purposes. Different techniques oriented to optimization of planar windings performance have been find in the literature, including the particular arrangements of parallel windings [50][51].

Investigations on Copper Losses on High Frequency Planar windings

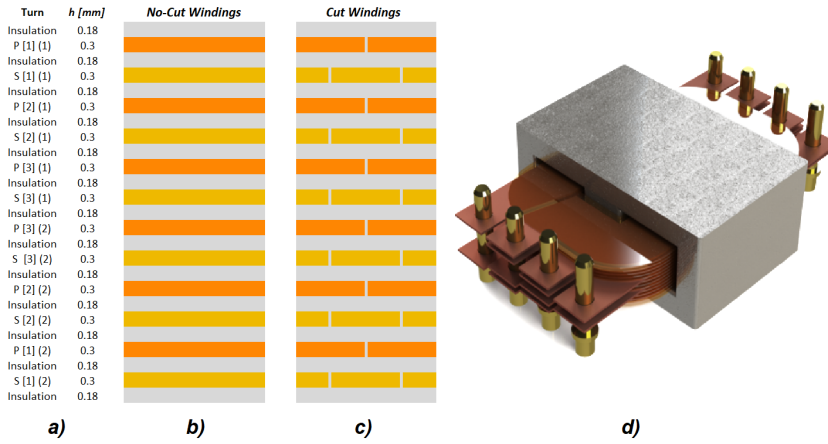


Fig.9.3. Planar Transformer prototypes, with and without current density equalization technique (*brick laying*). **a)** Windings/insulation thickness and primary (P) and secondary (S) interleaving pattern. Series turn number in square brackets. Parallel turn number in round parenthesis. **b)** No-Cut Winding's area cross-section, A_W . **c)** Cut Winding's area cross-section, A_W (*brick laying*). **d)** 3D model of Planar Transformer prototypes.

9.4. A NEW TECHNIQUE FOR CURRENT DENSITY EQUALIZATION

A possible new strategy for optimizing the current density distribution on planar windings has been identify. This new technique can be applied to planar transformer windings having a single turn per layer, typical of transformers with high current requirements. The *skin effect* and the *proximity effects* between interleaving planar windings could be engineer in order to cancel each other by using the strategy depicted in **Fig.9.3.c)**. Each of the layers, consisting of a single turn, has been cut in the length along the current flow. Primary (P) layers present a single cut at the center of the winding, dividing each turn in two parallel winding sections. Secondary (P) layers present two cuts at the center of the winding sections of the primary layers, presenting a cross-section pattern similar to *brick laying*. The *Skin effect* in each winding tends to concentrate the current density at the edges of the winding. By dividing each winding into parallel sections, a part of the *skin effect* could be reduced. Since primary and secondary windings are, interleave and carrying opposite currents, in the prototype using the brick laying cross-section depicted in **Fig.9.3.c)** the proximity effects between layers will tend to achieve the same current distribution in all layers as in **Fig.9.1.(right-top)**, and counteract the *skin effect* tendency to concentrate the current density in the edges (*cuts*) of the windings.

PERMANENT MAGNET BIASED INDUCTORS

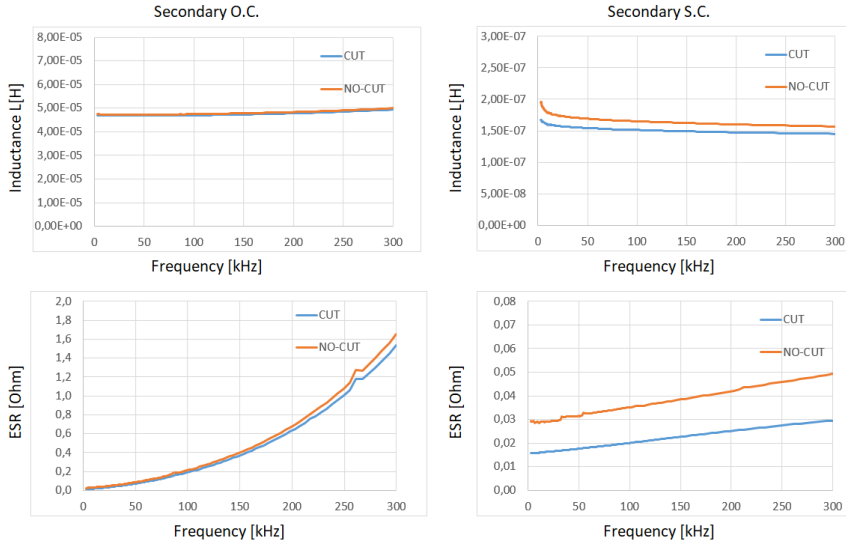


Fig.9.4. Empirical measurements on planar transformer prototypes. *Top:* Inductance vs frequency, L vs f . *Bottom:* Equivalent Series Resistance vs frequency, ESR vs f . *Left:* Measured with Open-circuit (O.C.) secondary. *Right:* Measured with Short-circuit (S.C.) secondary terminals. "NO-CUT" (orange line) corresponds to prototype depicted in Fig.9.3.b). "CUT" (blue line) is prototype using the technique depicted in Fig.9.3.c).

9.5. PRACTICAL IMPLEMENTATION

Two different planar transformer prototypes have been physically implemented. The prototypes are test on a converter using an H -bridge operating at 110 kHz frequency. Maximum input voltage is 50 V amplitude 50% duty cycle square wave. Peak current is 40 A and a total power handling of 2000 VA. Both transformer prototypes were implement using a planar ferrite transformer EE7878400421 Fair-Rite with material 98 and copper foil stampings. Each transformer presents only one turn per layer, two layers in parallel for each turn and a total of tree turns in series in both primary and secondary windings. The winding interleaving patter and the copper foil and insulation thickness presented in Fig.9.3.a) was use in both prototypes. One of the prototypes used common copper foil windings with no cuts along the current path, as depicted in the windings cross-section in Fig.9.3.b). The second prototype used copper foil windings with cuts along the current path, as depicted in the winding cross-section in Fig.9.3.c). The inductance, L [H] and the equivalent series resistance, ESR [Ω], as function of frequency, was measured using a precision RLC meter in both prototypes, refer as CUT and NO-CUT in Fig.9.4. Since both prototypes utilizes the

same core and winding thickness and interleaving pattern, differences in their measured equivalent series resistance, $ESR [\Omega]$, are assumed to be derive from the *brick-laying* technique. The measurements were performed at the primary windings, with two different conditions at the secondary windings: *Open-circuit* (O.C.) and *Short-circuit* (S.C.). It is noticeable that the inductance, $L[H]$ and equivalent series resistance, $ESR [\Omega]$, are practically identical in both prototypes when measured having an *Open-circuit* at the secondary windings (**Fig.9.4.left**). These measurements, with and *Open-circuit* at the secondary, are indicative of the transformer performance under no-load conditions. The mechanisms employ by the *brick-laying* technique, to equalize the current density, are based on the counteraction of the *Skin effect* and *Proximity effect*, and require the presence of opposite currents in consecutive winding layers. Therefore, this technique can only improve the winding current distribution during loaded conditions, when there is a current present in both primary and secondary windings. The measurements done with and *Short-circuit* at the secondary, are indicative of the transformer performance under full-load conditions (**Fig.9.4.right**). The inductance, $L[H]$ in both prototypes are practically identical, with minimal impact from the *brick-laying* technique. The measured equivalent series resistance, $ESR [\Omega]$, of the “CUT” windings prototype is considerably lower compared with the “NO-CUT” windings transformer. This experiment serves as a good proof of concept of the *brick-laying* technique for current density equalization in planar transformer windings, operating under full-load.

9.6. CONCLUSIONS ON AC LOSSES IN PLANAR WINDINGS

The main challenges in the prediction and optimization of AC losses in planar windings has been briefly analyze. A possible technique for improving the current distribution in interleave windings of high frequency planar transformers has been identified. The new current equalization technique, refer as *brick laying*, has been implemented and tested empirically. Two different planar transformer prototypes were built with and without using the *brick laying* technique on their windings. The prototypes were test on an H-bridge converter, operating at 110 kHz frequency, 50 V input square wave with a peak current of 40 A . The inductance, $L[H]$ and equivalent series resistance, $ESR [\Omega]$ as function of frequency, in both prototypes were measure using a precision RLC meter. Measurements were made both, with open-circuit and short-circuit conditions at the secondary windings in order to evaluate the transformer performance in both, no-load and full-load conditions respectively. The prototype using the new *brick laying* strategy in its windings, present approximately 40% lower $ESR [\Omega]$ when operating at full-load conditions (*Short-circuit secondary*). The measured performance of both prototypes operating under no-load conditions (*Open-circuit secondary*), were practically identical. This practical investigation can serve as a successful proof of concept of the proposed strategy for improvement of current distribution in planar transformer windings. Further analysis and experimentation and FEA simulations are encouraged as focus for future research.

PERMANENT MAGNET BIASED INDUCTORS

REFERENCES

- [1] J.W. Kolar, U. Drofenik, J. Bieta, M.L. Heldwein, H. Ertl, T. Friedli, S. D. Round, "PWM Converter Power Density Barriers", 2007 Power Conversion Conference – Nagoya, pp. 9-29. 2007.
- [2] Wilson, T.G.: 'The evolution of power electronics', IEEE Transactions on Power Electronics, 2000, Volume 15, Issue 3, pp. 439–446. 2000.
- [3] Helong Li, Stig Munk-Nielsen, Xiongfei Wang, Ramkrishan Mahneshwari, Szymon Bęczkowski, Christian Uhrenfeldt, W. -Toke Franke, "Influences of Device and Circuit Mismatches on Paralleling Silicon Carbide MOSFETs", IEEE Transactions on Power Electronics. vol. 31, no. 1, pp. 621-634, Jan. 2016.
- [4] L. Helle, K.B. Larsen, A.H. Jorgensen, S. Munk-Nielsen, F. Blaabjerg, "Evaluation of modulation schemes for three-phase to three-phase matrix converters," IEEE Transactions on Industrial Electronics, vol. 51, no. 1, pp. 158-171, Feb. 2004.
- [5] Ui-Min Choi, Frede Blaabjerg, Søren Jørgensen, Stig Munk-Nielsen, Bjørn Rannestad, "Reliability Improvement of Power Converters by Means of Condition Monitoring of IGBT Modules", IEEE Transactions on Power Electronics, vol. 32, no. 10, pp. 7990-7997, Oct. 2017.
- [6] Fausto Fiorillo, Giorgio Bertotti, Carlo Appino, Massimo Pasquale, "Soft Magnetic Materials", Wiley Encyclopedia of Electrical and Electronics Engineering. 15 November 2016.
- [7] Gaoyuan Ouyang, Xi Chen, Yongfeng Liang, Chad Macziewski, Jun Cui, "Review of Fe-6.5wt%Si high silicon steel - A promising soft magnetic material for sub-kHz application", Journal of Magnetism and Magnetic Materials. Volume 481, pp. 234-250. 1 July 2019.
- [8] R. Krishnan, A.S. Bharadwaj, "A comparative study of various motor drive systems for aircraft applications", Proceedings of the 1991 IEEE Industry Applications Society Annual Meeting, Dearborn, MI, USA. Volume 1, pp. 252–258. 28 September–4 October 1991.
- [9] Kapila Warnakulasuriya, Andrea Polti, Farhad Nabhani, "Evolution of Magnetics in Power Electronics Applications and Facing the Challenges of Future Electronics Industry," PCIM Europe 2017; International Exhibition and Conference for Power Electronics, Intelligent Motion, Renewable Energy and Energy Management, 2017, pp. 1-5.
- [10] McLyman, Colonel. "Transformer and Inductor Design Handbook", 4th edition 2017, DOI:10.1201/b10865. ISBN: 9781315217666.

PERMANENT MAGNET BIASED INDUCTORS

- [11] J.T. Ludwig, "Design of optimum inductors using magnetically hard ferrites in combination with magnetically soft materials", *Journal of Applied Physics*. Volume 29, Issue 3, pp. 497-499. Mar 1958.
- [12] J.T. Ludwig, "Inductors biased with permanent magnets. Part I: Theory and analysis", *American Institute of Electrical Engineers, Part I: Communication and Electronics, Transactions of the*. Volume 79, Issue 3, pp. 273-278. July 1960.
- [13] J.T. Ludwig, "Inductors biased with permanent magnets. Part II: Design and synthesis", *American Institute of Electrical Engineers, Part I: Communication and Electronics, Transactions of the*. Volume 79, Issue 3, pp. 278-291. July 1960.
- [14] J.T. Ludwig, "Inductors biased with permanent magnets", *Electrical Engineering*, Volume 80, Issue 6, p 408. June 1961.
- [15] Akio Nakamura, and Junpei Ohta, "A new reverse-biased choke coil", *Proceedings of Powercon 9 C-5*. TDK-Electronics Company Ltd. Power Concepts, Inc. July 1982.
- [16] Stefan Herzog, Alexander Stadler and Christof Gulden, "MaxFlux–Magnetically Biased Inductor", *Bodo's Power*, Jun 2014.
- [17] Kuo Baoquan, Song Liwei, Zhang Qianfan, and Cheng Shukang, "The principle and design of the permanent magnet bias DC reactor", *Proceedings of the Fifth International Conference on Electrical Machines and Systems, ICEMS 2001*. Volume 1, pp. 230-232. August 2001.
- [18] Teruhiko Fujiwara, and Hatsuo Matsumoto, "A new downsized large current choke coil with magnet bias method", *Telecommunications Energy Conference, 2003. INTELEC '03. The 25th International*. IEEE, pp. 416-420. October 2003.
- [19] Rafal Wrobel, Neville McNeill, and Phil H. Mellor, "Design of a high-temperature pre-biased line choke for power electronics applications", *Power Electronics Specialists Conference. PESC 2008*. IEEE, pp 3171–3177. Jun 2008.
- [20] G.M. Shane, and S.D. Sudhoff, "Permanent magnet inductor design", *Electric Ship Technologies Symposium*, IEEE, pp. 330-333. 10-13 April 2011.
- [21] G.M. Shane, and S.D. Sudhoff, "Design and Optimization of Permanent Magnet Inductors", *Applied Power Electronics Conference and Exposition (APEC) 2012, 27th Annual IEEE*, pp 1770 – 1777. Feb 2012.
- [22] G.M. Shane, and S.D. Sudhoff, "Design Paradigm for permanent-magnet-inductor-based power converters", *IEEE Transactions on Energy Conversion*, Vol 28, NO 4, pp 880 – 893. December 2013.
- [23] Zhigang Dang and Jaber A. Abu Qahouq, "Permanent magnet toroid power inductor with increased saturation current", *Applied Power Electronics Conference and Exposition (APEC) 2013, 28th Annual IEEE*, pp 2624 – 2628. March 2013.

- [24] Andres Revilla Aguilar, and Stig Munk-Nielsen, "Method for introducing bias magnetization in ungaped cores: The Saturation-Gap", 2014 IEEE Applied Power Electronics Conference and Exposition (APEC) 2014, 29th Annual IEEE, pp 721 - 725. 16-20 March 2014.
- [25] Andres Revilla Aguilar, Stig Munk-Nielsen, Marco Zuccherato and Hans-Jørgen Thougard, "Size reduction of a DC line choke using saturation gap and biasing with permanent magnets", PCIM Europe 2014, pp 1667 – 1674. Nuremberg, Germany, 20-22 May 2014.
- [26] Andres Revilla Aguilar, and Stig Munk-Nielsen, "Design analysis and simulation of magnetic biased inductors with Saturation-Gap", Power Electronics and Applications (EPE'14-ECCE Europe), 2014 16th European Conference on, pp 1 - 11. 2014.
- [27] Andres Revilla Aguilar, and Stig Munk-Nielsen, "Half Size Reduction of DC Output Filter Inductors With the Saturation-Gap Magnetic Bias Topology", IEEE Journal of Emerging and Selected Topics in Power Electronics (JESTPE), Vol. 4, Issue 2, pp 382 – 392. June 2016.
- [28] S. P. McDonald, G. J. Atkinson, R. Martin and S. Ullah, "Magnetically biased inductor for an aerospace switched reluctance drive", 2015 IEEE International Electric Machines & Drives Conference (IEMDC), pp. 1272-1278, May 2015.
- [29] M. Schmidhuber, R. Ludwig, M. Baumann, M. Rossa and M. Schmeller, "Magnetically Biased High Power Coil Module", Proceedings of PCIM Europe 2015; International Exhibition and Conference for Power Electronics, Intelligent Motion, Renewable Energy and Energy Management, pp. 1-6, May 2015.
- [30] Z. Dang and J. A. Abu Qahouq, "Permanent magnet power inductor with EE core for switching power converters", 2015 IEEE Applied Power Electronics Conference and Exposition (APEC), 2015, pp. 1073-1077, 15-19 March 2015.
- [31] Z. Dang and J. A. Abu Qahouq, "Evaluation of High-Current Toroid Power Inductor With NdFeB Magnet for DC–DC Power Converters", IEEE Transactions on Industrial Electronics, vol. 62, no. 11, pp. 6868-6876, Nov. 2015.
- [32] Z. Dang and J. A. Abu Qahouq, "Permanent-Magnet Coupled Power Inductor for Multiphase DC–DC Power Converters", IEEE Transactions on Industrial Electronics, vol. 64, no. 3, pp. 1971-1981, March 2017.
- [33] S. Lin, J. Friebe, S. Langfermann and M. Owzareck, "Premagnetization of High-Power Low-Frequency DC-Inductors in Power Electronic Applications", PCIM Europe 2019; International Exhibition and Conference for Power Electronics, Intelligent Motion, Renewable Energy and Energy Management, pp. 1-7, May 2019.
- [34] J. Friebe, S. Lin, L. Fauth and T. Brinker, "Premagnetized Inductors in Single Phase dc-ac and ac-dc Converters", 2019 IEEE 15th Brazilian Power Electronics Conference and 5th IEEE Southern Power Electronics Conference (COBEP/SPEC), pp. 1-6, Dec 2019.

PERMANENT MAGNET BIASED INDUCTORS

- [35] B. Houska, D. Yan, J. Benzaquen and D. Divan, "Partial Saturation in Permanent Magnet Inductors", 2022 IEEE Energy Conversion Congress and Exposition (ECCE), 2022, pp. 1-7. Oct. 2022.
- [36] R. S. Yang, A. B. Nadler, C. R. Sullivan and D. J. Perreault, "Permanent Magnet Hybrid Core Inductors for High Saturation Capability", 2022 IEEE 23rd Workshop on Control and Modeling for Power Electronics (COMPEL), pp. 1-8, Jun 2022.
- [37] Z. An et al., "Laminated Permanent Magnets Enable Compact Magnetic Components in Current-Source Converters", IEEE Transactions on Power Electronics, vol. 37, no. 10, pp. 12391-12405, Oct. 2022.
- [38] Patent No. list: CA606140(A), US3359519(A), US3735305(A), US3968456(A), US4009460(A), US4103221(A), US4491819(A), US5350980(A), EP0744757(A1)(A4)(B1), JPH08316049(A), JPH09283353(A), JPH09213546(A), CN2356409(Y), KR20000024608(A), US20020390061(A1), US2002097126(A1), US2002097127(A1), US2002089400(A1), KR20020020265(A), JP2002359125(A), JP2002313647(A), JP2002289443(A), JP2002222714(A), JP2002222721(A), JP2002175917(A), JP2002175926(A), JP2002175925(A), JP2003124041(A), JP2003318046(A), JP2003017340(A), US20046717504(B2), US2004168303(A1), US20046734771(B2), JP2004055787(A), JP2004055734(A), US20056853285(B2), US20056906608(B2), US20060214759(A1), JP2006196591(A), JP2007281204(A), US2008303620(A1), US2008303619(A1), TW200828356(A), JP2008078177(A), US20100194512(A1), US20118004379(B2), CN103578688(A), JP2015198159(A), CN106057395(A), US2016042855(A1), US2017117077(A1), CN212136108(U), CN212136185(U), US10629357(B2), US2021249176(A1).
- [39] H. Lovatt and P. Watterson, "Energy stored in permanent magnets", IEEE Transactions on Magnetics, Vol. 35(1) pp 505-507. Jan 1999.
- [40] J. Friebe and P. Zacharias, "Review of Magnetic Material Degradation Characteristics for the Design of Premagnetized Inductors", IEEE Transactions on Magnetics, Vol. 50, Issue 3, March 2014.
- [41] R.J. Pasterczyk and T. Delaforge, "Engineering Illusion to accurately Predict Power Losses in Magnetic Materials on the Base of Standard Manufacturers' Datasheets", PCIM Europe 2014, pp 1 – 9. Nuremberg, Germany, 20-22 May 2014.
- [42] W. Fam, G. Bahl, "Two Related Types of Parametric Transformers", IEEE Trans. On Magnetics, Vol 10, Issue 3, Sep 1974, pp. 690-693.
- [43] M. Yoshida, M. Ohta, Y. Sakamoto, "Considerations on the operation point of a planar parametric transformer based on the Mathieu equation", IEEE International Power Electronics Conference, ECCE Asia, 2010, Sapporo, Japan.
- [44] Z.H. Meiksin, "Comparison of Orthogonal- and Parallel-Flux Variable Inductors", IEEE Trans. In Industry Applications, Vol IA-10, Issue 3, May 1974, pp. 417-423.

- [45] E. Salih Tez, I.R. Smith, "The Parametric Transformer: A Power Conversion Device Demonstrating the Principles of Parametric Excitation", IEEE Trans. On Education, Vol 27, Issue 2, May 1984, pp. 56-65.
- [46] Andres Revilla Aguilar, Bjørn Rannestad and Stig Munk-Nielsen, "Parametric Transformer using PM-Inductors with Saturation-gap", Journal of The Institution of Engineering and Technology, IET PEL 2020, Vol. 13, Issue 19, 30 December 2020, pp. 4581-4591.
- [47] P. L. Dowel, "Effects of eddy currents in transformer windings", Proceedings of the Institution of Electrical Engineers, Vol. 113, Issue 8, August 1966, pp. 1387-1394.
- [48] J. Ferreira, "Improved analytical model of conductive losses in magnetic components", IEEE Transactions on Power Electronics, Vol. 9, Issue 3, January 1994, pp. 127-131.
- [49] Xi Nan and C.R. Sullivan, "An improved calculation of proximity-effect loss in high-frequency windings of round conductors", IEEE 34th Annual Conference of Power Electronics Specialist, 2003. PESC 03., Acapulco, Mexico, 2003, Vol. 2, pp. 853-860.
- [50] Z. Ouyang, O.C. Thomsen and M.A.E. Andersen, "Optimal Design and Tradeoff Analysis of Planar Transformer in High-Power DC-DC Converters", IEEE Transactions on Industrial Electronics, Vol. 59, Issue 7, July 2012, pp. 2800-2810.
- [51] Ziwei Ouyang; Michael A. E. Andersen, "Overview of Planar Magnetic Technology—Fundamental Properties", IEEE Transactions on Power Electronics, vol. 29, no. 9, pp. 4888-4900, Sept. 2014.
- [52] David Meeker, "Finite Element Method Magnetics", Finite Element Method Magnetics, Version 3.3, March 17, 2003.
<https://www.femm.info/wiki/Documentation/>.

ISSN (online): 2446-1636
ISBN (online): 978-87-7573-703-1

AALBORG UNIVERSITY PRESS